Developing Extended Strands in Girder-Diaphragm Connections for Positive Moment Resistance

Kristina Tsvetanova Tsvetanova

A thesis
submitted in partial fulfillment of the
requirements for the degree of

Master of Science in Civil Engineering

University of Washington

2017

Committee:
John F. Stanton
Marc O. Eberhard
Paolo M. Calvi

Program Authorized to Offer Degree:
Department of Civil and Environmental Engineering

University of Washington

Abstract

Developing Extended Strands in Girder-Diaphragm Connections for Positive Moment Resistance

Kristina Tsvetanova Tsvetanova

Co-Chairs of the Supervisory Committee:
Professor John F. Stanton
Civil and Environmental Engineering

Professor Marc O. Eberhard
Civil and Environmental Engineering

In bridges with precast prestressed concrete girders, the resistance to seismic effects is achieved by the interaction between the columns, the cap beam and the girders. Said components must be connected such that flexural resistance is provided. Under the impact of longitudinal seismic motion, the bottom flanges of the two girders, meeting end-to-end at the cap beam, will be under tension and compression, respectively. The tension connection is presently made by extending some of the bottom strands into the cast-in-place diaphragm. At this location, the space available is too small for development by bond in the straight strands alone. Since concrete in the diaphragm is highly confined, it can probably carry high bearing stress and a small bearing area may be possible. Thus, the goal of this project is to create a reliable, effective, as well as practically applicable way of anchoring strands extended from the girder into the cap beam.

The first stage in the development of the girder-diaphragm seismic connection consists of establishing the adequacy of the smallest possible strand anchor capacity such that a

strand ductile failure due to yielding and fracture is achieved before the strand anchor fails by crushing the concrete at the bearing surface.

As a second stage, the impact of the possible failure mechanisms of the strands embedded in the diaphragm on the development of the girder-cap beam positive moment connection was investigated.

Finally, the distribution of girder bending moments across the bridge deck was evaluated, while investigating the influence on that distribution of the most important bridge parameters, such as cracking of bridge components, as well as varying cross sectional dimensions.

TABLE OF CONTENTS

LIST OF FIGURES

LIST OF TABLES

NOTATION LIST

Chapter 1

f_{pu}	ultimate strength of prestressing strand

Chapter 2

Δ	displacement
ϵ_r	radial strain
ϵ_z	axial strain
ϵ_θ	circumferential (i.e. hoop) strain
ϵ_{hoop}	hoop strain
ϵ_{radial}	radial strain
ϵ_{vert}	vertical (i.e. axial) strain
$\mu\varepsilon$	micro-strain
ν	Poisson's ratio
ϕ	internal friction angle
σ_r	radial stress
σ_θ	circumferential (i.e. hoop) stress
σ_{hoop}	hoop stress
A_b	barrel anchor bearing area
A_c	casting anchor bearing area
A_p	prestressing strand cross-sectional area
c_L	confinement effectiveness coefficient
E_p	prestressing strand elastic modulus
E_s	steel elastic modulus
f'_c	specified (28-day) concrete compressive strength
f'_L	lateral confinement stress
f_u	reinforcing steel ultimate stress
f_y	reinforcing steel yield stress
$f'_{bearing}$	ratio of applied load to bearing area
f'_{cc}	confined concrete strength
L_p	prestressing strand length
P	applied load
p	pressure vessel internal pressure
R	pressure vessel inner radius
r	pressure vessel inner radius
t	pressure vessel wall thickness

Chapter 3

λ	concrete weight factor
Ψ_2	CCD method edge distance factor
$\Psi_{c,N}$	ACI method cracked concrete factor
$\Psi_{cp,N}$	ACI method post-installed anchor factor
$\Psi_{ec,N}$	ACI method grouped anchor eccentric tension loading factor
$\Psi_{ed,N}$	ACI or PCI method anchor edge effect factor
A_N	CCD or PCI method projected concrete failure area for a single or grouped embedded anchors
A_{N_c}	ACI method projected concrete failure area of single or grouped embedded anchors

$A_{N_{co}}$	ACI method projected concrete failure area of a single embedded anchor
A_{No}	CCD method projected concrete failure area of a single embedded anchor
C_{bs}	PCI method breakout strength coefficient
C_{crb}	PCI method cracking factor
h_{ef}	effective embedment depth of anchor
k_c	CCD method cracked concrete adjustment factor
k_{nc}	CCD method calibration factor
N_n	CCD method failure load for multiple embedded anchors
N_{cbg}	ACI anchor group breakout strength
N_{cb}	ACI method single embedded anchor, PCI method single or grouped embedded anchors breakout strength
N_{no}	CCD method failure load for single embedded anchor

Chapter 4

α	girder rigid end offset factor
β	girder bending stiffness per unit length of cap beam
γ	column longitudinal reinforcement cc spacing to column diameter ratio
λL_{cb}	total girder bending to cap beam torsional stiffness for half width of the bridge
ω_E	concrete unit weight for elastic modulus calculations
ω_{DL}	concrete unit weight for dead load calculations
ϕ	LRFD strength-reduction factor
ϕ	angle of twist
ρ	reinforcement ratio
A_s	steel reinforcement area
$b_{cb,eff}$	cap beam rigid end offset
B_{eff}	superstructure effective width for girder bending moment distribution
$b_{g,eff}$	girder rigid end offset
c_c	reinforcement clear cover
d_b	longitudinal reinforcement bar diameter
D_c	column diameter
D_s	superstructure depth
e	natural exponent (Euler's constant)
E_g	girder elastic modulus
F	longitudinal seismic load
G_{cb}	cap beam shear modulus
h	column diameter
i	girder line number
I_g	moment of inertia of composite bridge deck and girder
J_{cb}	cap beam torsion constant
L_g	girder span length
L_{cb}	half of the cap beam length
M_g	girder moment
M_n	column nominal moment capacity
M_p	column plastic moment capacity
M_{po}^{CG}	plastic hinging moment at the cg of a bridge superstructure
M_{sei}	seismic moment per girder line

M_{sei}^{Ext}	seismic moment per girder line outside B_{eff}
M_{sei}^{Int}	seismic moment per girder line within B_{eff}
N_g^{ext}	number of girders outside B_{eff}
N_g^{int}	number of girders within B_{eff}
N_L	number of girder lines per half of bridge deck width
s_g	girder spacing
T	internal torque
t	distributed torque
T_o	applied torque

Chapter 5

τ_{M_t}	shear stress due to torsional moment
τ_{max}	maximum shear stress
$\tau_{V_{max}}$	maximum transverse shear stress
A_c	cap beam cross-sectional area
A_p	prestressing strand cross-sectional area
b_{cb}	smaller cap beam cross-sectional dimension for torsion
d_b	prestressing strand diameter
E_p	prestressing strand elastic modulus
f_r	concrete modulus of rupture
f_{cs}	prestressed concrete service stress
f_{pe}	prestressing strand effective prestress
f_{ps}	presstressing strand ultimate stress
f_{py}	presstressing strand yield stress
h_{cb}	larger cap beam cross-sectional dimension for torsion
k_g	uncracked girder bending stiffness
k_θ	fully-cracked girder rotational stiffness
k_{ps}	extended strand axial stiffness
L'_d	extended strand debonding length
$M_{g,i}$	i^{th} girder line moment
N_{ps}	required number of extended prestressing strands
S_{g1}	girder bottom section modulus
y_{cg}	girder (bottom) center of gravity

Chapter 6

μ	shear transfer interface friction coefficient
Ψ_e	reinforcement coating factor
Ψ_s	reinforcement size factor
Ψ_t	reinforcement location factor
A	WSDOT BDM A dimension
A_{cv}	shear transfer interface area
A_{vf}	shear transfer interface reinforcement area
b_{vi}	shear transfer interface width
c	shear transfer interface cohesion factor
e_p	prestressing strand eccentricity relative to girder centroid
l_d	reinforcement bar development length
l_t	prestressing strand effective stress transfer length
L_{col}	column clear height used to determine overstrength moments
L_{vi}	shear transfer interface length
$M_{n,i}$	interface shear transfer nominal moment capacity
M_{po}^{Base}	plastic overstrength moment at column base

M_{po}^{top}	plastic overstrength moment at column top
P_c	net compressive force normal to interface shear plane
T_o	maximum cap beam torque equal to half of the total seismic moment at the center of gravity of superstructure
t_s	slab thickness
V_{ni}	girder-diaphragm interface nominal shear resistance
$Y_{t\ slab}$	center of gravity of superstructure measured from the top of the slab

ACKNOWLEDGMENT

First and foremost, I would like to express my most sincere gratitude to my advisors, Professor John Stanton and Professor Marc Eberhard, for their invaluable guidance and unyielding support throughout the course of this research. I deeply appreciated this incredible opportunity to expand my knowledge and grow as a structural engineer, inspired by their expertise and vast experience. I am also thankful to Professor Paolo Calvi for his contribution to this research project. Last, but not least, I am grateful to Professor Don Janssen for his advice and recommendations.

Furthermore, I would also like to thank our sponsor, the Washington Department of Transportation, without whom this project would not have been possible. Mr. Bijan Khaleghi and the rest of the bridge group provided a lot of constructive input, which was incredibly helpful for guiding the project into delivering a truly practical engineering solution.

I am also indebted to many other individuals, whose help and encouragement played a big role in the completion of the project work. I would like to thank Vince Chaijaroen for his help and training, Andrew Winter, for his tremendous support and tireless help, as well as his incredibly insightful advice; Travis Thonstad and Ashley Heid for their assistance and guidance.

Finally, I am very grateful to my family, whose unwavering love and support have motivated and empowered me to be the person who I am today and to achieve many successes. I cherish you deeply and I am blessed to have you in my life. Thank you to the Core Crew - Ashley Heid, whom I met, while asking for directions to More Hall on the very first day of school, who is a good friend, and an inspiration both as a woman, and as an engineer; to Andrew Yang, whom I connected with so incredibly quickly, I hope that you will always be

one of my best friends. Thank you to the Extended Core Crew, Andrew Winter and Ryan Ganey, for making our office simultaneously a knowledgeable, as well as a truly enjoyable and fun environment to work in. Thank you all for your friendship and companionship, your advice, support and encouragement. I was lucky to have met you and I hope I am lucky enough to always have you in my life.

Chapter 1

INTRODUCTION

1.1 Background

A typical Washington State concrete bridge bent consists of cast-in-place piers, precast, prestressed girders, and a cap beam. The latter is comprised of a precast component, called a crossbeam, and a cast-in-place component, flush with the girders, designated as a diaphragm. When subjected to longitudinal seismic loading, the column will experience bending moments, which are then transferred to the cap beam, manifested as torsional moments there. The torsion of the cap beam induces bending moments in the girders, such that pairs of girders whose ends meet in the diaphragm will resist positive moments on one side of the cap beam and negative moments on the other. Thus, interaction between all three bridge bent components must be achieved, such that the induced loads are transferred effectively, providing adequate seismic resistance. Negative moments are transferred using the tension strength provided by steel in the deck, over the cap beam. That moment transfer is not in question.

This project addresses the load transfer from the cap beam to the girders, focusing on providing resistance for positive girder bending moments. The bottom flange of a girder under positive moment will be subjected to tensile stresses; thus, the development of a tension connection is necessary. The current connection detail used by WSDOT to provide positive moment resistance consists of extending some of the prestressing strands from the bottom flange of the girder into the cast-in-place diaphragm. The extended strands are anchored with strand chucks with backing plates welded to them, because the available length is too short to develop the strand by bond alone. The current WSDOT approach, as well as other methods such as bending the extended strands, result in congestion and poor

constructability. Bar conflicts are likely in cases where the girders are not collinear such as in a curved bridge with secant girders. Therefore, the goal of this project is to create a reliable, effective, as well as practically applicable way of anchoring strands, extended from the girder into the diaphragm.

1.2 Extended Strand Connection Details

1.2.1 Positive Seismic Moment Connection in Washington State

The current positive seismic moment detail for the girder-diaphragm connection in the state of Washington involves extending some of the prestressing strands, located in the bottom flange of the girders, and anchoring them with barrel anchors, including a 4"x4"x½" square backing plate welded to the barrel anchors in order to provide a larger bearing area. This detail is shown in Figure 1.1.

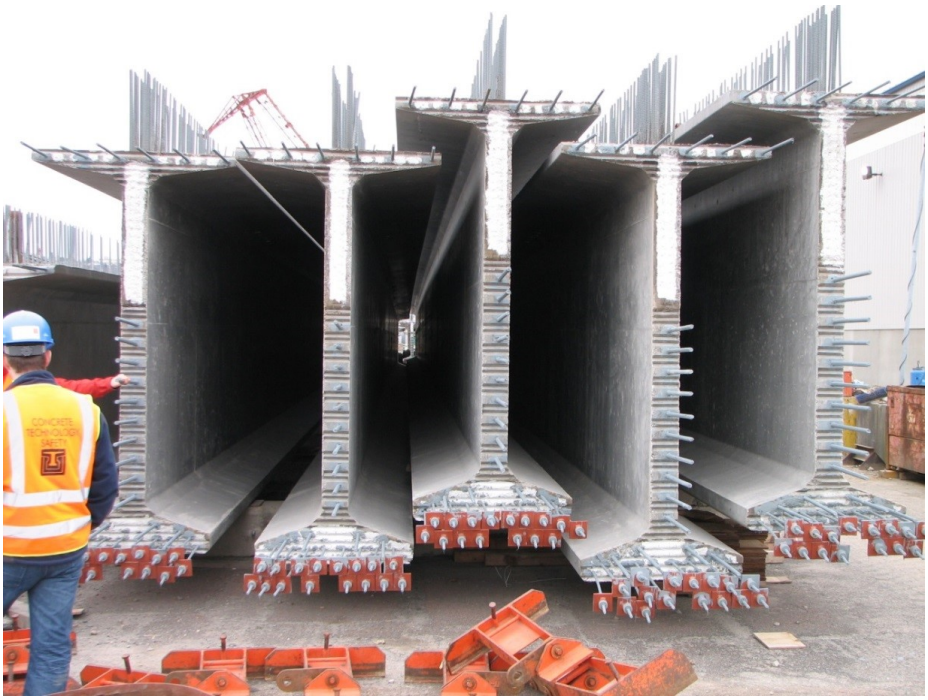

Figure 1.1: Extended Girder Strands for Positive Longitudinal Seismic Moment Connection in Washington State

A precast crossbeam, used in the state of Washington is shown in Figure 1.2 and gives

a general idea of a typical diaphragm reinforcement pattern (Marsh et al., 2013). Cast in place cross-beams are more common, but the reinforcement pattern is essentially identical.

Figure 1.2: Precast Bent Cap Construction in the State of Washington (Marsh et al., 2013)

The erection of the girders with extended strands, equipped with strand anchors with welded bearing plates shown in Figure 1.1 would be very difficult, as the extended anchored strands would be conflicting with the heavy diaphragm reinforcement shown in Figure 1.2.

It should be noted that the prototype bridge superstructure, for which a crossbeam detail is shown in Figure 4.3 was used as a reference structure throughout this thesis. The crossbeam detail differs from the one depicted in Figure 1.2, although it is still similar in terms of the extent of diaphragm congestion.

Similar connection details, although not explicitly considering a longitudinal seismic effect, have been investigated by other departments of transportation.

In non-seismic applications, there is less need for longitudinal resistance, and thus torsional resistance of the cap beam. The primary need is for girder continuity in order to

maintain a constant slope across the cross-beam and a smooth side. Consequently, the diaphragm can be much narrower than in seismic applications. The non-seismic applications are considered in detail in Subsection 1.2.2.

1.2.2 Non-Seismic Applications

Precast prestressed girders can be made continuous for the effect of live load by connecting the girders at the support. Once the girders meeting end-to-end are connected by the casting of the diaphragm, they might camber up due to creep, shrinkage and temperature effects. These restraints cause a positive moment at the diaphragm. Unless reinforcement on the bottom girder flange level is provided, the girder-diaphragm joint would crack, eliminating the longitudinal continuity. Then, the girders would act like simple spans between supports, leading to midspan moments of much higher magnitude. Other factors, such as the age of girders at time of erection, and connection details, such as extending additional mild reinforcement horizontally from girder webs into the diaphragm, have an impact on the severity of the restraint moment effects. The positive moment reinforcement is provided by extending prestressing strands from the girder bottom flanges into the diaphragm or by embedding bent mild reinforcing bars extended from the end of the precast girders into the diaphragm.

Miller et al. (2004) carried out a detailed study in order to investigate the positive moment connection between girders, providing continuity of the structure. The research included a literature review, as well as thorough information on the current positive moment connection details used by many different departments of transportation, and an experimental study. The latter was carried out in order to determine the impact of varying factors, such the use of either bent mild reinforcement or bent prestressing strands, extending from girder ends, while having the girder ends either embedded or not embedded into the diaphragm.

The use of additional stirrups in the diaphragm on the effectiveness of the continuity connection was also investigated. The different connections were subjected to cyclic tests.

Connections with extended bent strands failed due to the pullout of the strands from the concrete in cases with girders not embedded in the diaphragm; connections with girders embedded in the diaphragm, experienced both pullout of the strands and pullout of the girders from the diaphragm, and as evidence for the latter, cracking and spalling of concrete on the face of the diaphragm was observed. Connections developed by extending bent mild reinforcing bars need to include an asymmetric pattern of the bars, to avoid bar conflicts, thus an asymmetric response in the system is expected. The connections for both girders embedded and girders not embedded in the diaphragm fail due to fracture of the steel, followed by a girder pullout from the diaphragm, which was evident due to the excessive spalling of diaphragm face concrete. The mild bar connection with girders embedded into the diaphragm lasted for twice the number of testing cycles, when compared to the one in which the girders were not embedded into the diaphragm. For bent strands, the connection with embedded into the diaphragm girders lasted three times the number of cycles than that of the connection without embedded into the diaphragm girders. Furthermore, it was found that the use of stirrups in the diaphragm arrest the diagonal cracks, which occur during the girder (or strand) pullout failure and thus the ductility of the connection increases (after the pullout failure has started). All connections had sufficient strength and performed satisfactorily; thus, it is this study's recommendation that the engineer chooses what to use in a particular case. (Miller et al., 2004).

Two more research programs, investigating this issue are summarized as follows.

Noppakunwijai et al. (2002) at the University of Nebraska-Lincoln have proposed extending some of the strands in the bottom girder flanges into the diaphragm and bending them 90° as an effective method of resisting the positive restraint moments that take place at the diaphragm due to shrinkage and creep of the girders. The proposed detail is shown in Figure 1.3. A similar detail is also used in other states such as New York. Bending the extended strands would act as an anchorage of the longitudinal reinforcement, aiding to preventing bond failure, and thus would also be beneficial in improving girder shear resistance.

Figure 1.3: Bent Extended Strand Detail (Noppakunwijai et al., 2002)

The strands are bent at the prestressing plant with little additional cost. The research concluded that extending 0.6" strands horizontally for a short distance (10") and including a 26" vertical segment bent at 90° into the diaphragm would ensure the strands can develop a stress of $0.8f_{pu}$ prior to pullout (Noppakunwijai et al., 2002).

The effectiveness of this detail in resisting longitudinal seismic moment is considered as follows. This research did not include any investigation of the behaviour of groups of strands, but rather investigated single bent strands with different embedment depths and dimensions (0.5" and 0.6" diameter) tested in tension. The observed failure modes always occurred due to pullout of the strands as also found by Miller et al. (2004); even for a total embedment depth of 52" for a 0.6" strand; the strand capacity was not reached. This observation does not agree with findings, presented later in this thesis, that 40" of embedment for 0.6" diameter strand is sufficient for the development of strand fracture. This goes to show that strand bond is very unreliable mechanism in developing resistance. If no reinforcing bars are extended from the girder web, no additional resistance to girder pullout exists, and the

girders would be unseated by the time the strands pullout of the diaphragm. This detail is also not practical in terms of constructability, since for a large number of extended strands there would be excessive congestion. For example, as a result of the calculations included in the report, it was determined that 17 strands need to be extended and bent. Such a high number of extended bent strands would make girder erection extremely difficult.

Similarly, research conducted by Newhouse et al. (2007) at Virginia Polytechnic Institute and State University studied the effectiveness of both extended strands and extended reinforcing bars in providing resistance of positive restraint moments. The test setup is shown in Figure 1.4.

(a) (b)

Figure 1.4: Bent Extended Strand and Reinforcing Bar Details (Newhouse et al., 2007)

The strands were extended a total of 24", including a 9" horizontal portion and a 15" vertical segment bent at 90°. The bars were bent at 180°, creating a hairpin-shape with equal length legs embedded 5' into the girder ends and the bends extending 11" from the ends of the girders.

The test assembly consisted of two girder spans, which framed into a 12" wide cast-in-place diaphragm that was flush with the girder ends, and a cast-in-place deck above the girders. A cyclic vertical load was applied to one of the girder ends away from the diaphragm to assess the performance of each configuration at resisting positive restraint moments and establishing continuity between the girders, as well as providing additional moment resistance in the event of an overload scenario such as an earthquake. As a result of these tests, the reinforcing bar detail exhibited a much more ductile behavior when compared to the bent extended strand configuration (Newhouse et al., 2007).

While the U-bar detail provides strength and ductility, the bars' rigidity risks assembly difficulties when the girder is lowered into place, because they cannot easily be moved to alleviate conflicts. Furthermore, the girder bottom flange is also likely to contain many strands, leaving little remaining space to embed the bars.

Using plain bent extended strands results in a very large displacements, which would be avoided if strand anchorage was utilized.

1.3 Related Research

1.3.1 Seismic Loading of Precast Prestressed Girder Bridges - (Holombo et al., 2000)

Experimental testing of two 40% scale model bridges was conducted to develop a design approach for precast, prestressed spliced-girder bridges under the impact of longitudinal seismic loading. The models were comprised of a column connected to a bent cap with two different girder configurations. In one test specimen, four lines of deck bulb tee girders were used, whereas in the other, a pair of lines of bathtub units were utilized. The test setups are shown in Figure 1.5. Based on the results of these tests, the authors came up with the following recommendation relating to this project. Holombo et al. (2000) state that the variation in the strains, measured in the longitudinal reinforcement across the bridge deck, is indicative of the distribution of girder bending moments across the bridge deck.

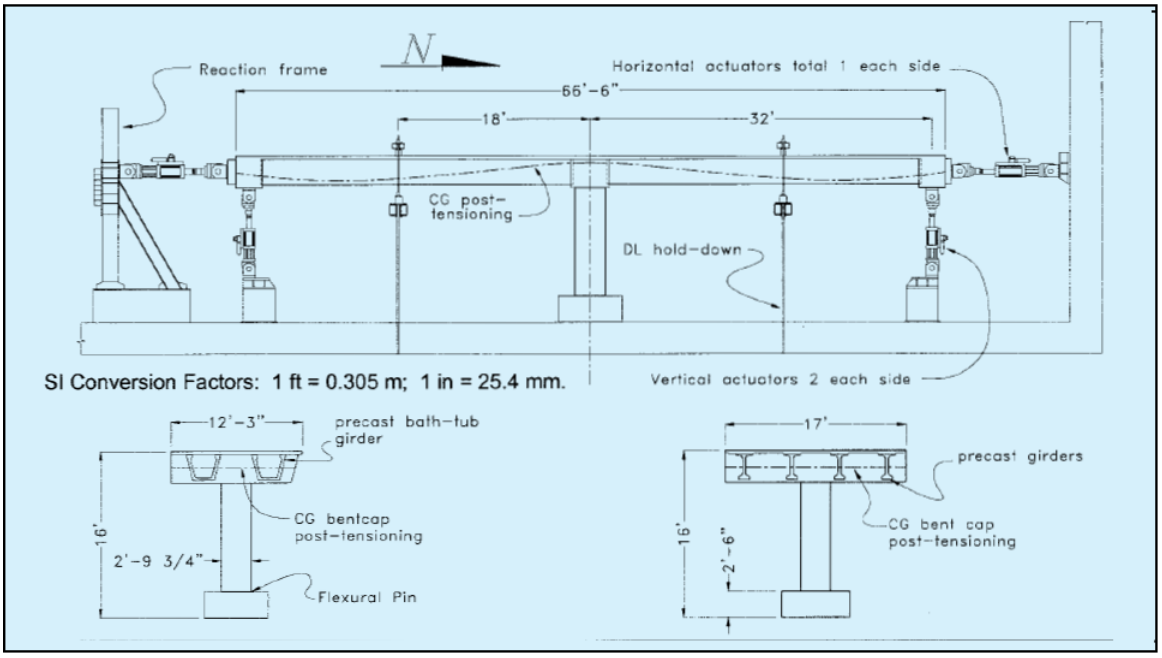

Figure 1.5: Prototype Layouts and Test Setup (Holombo et al., 2000)

A typical California cap beam system is flush with the girders and so has a smaller cross-section, and is much more torsionally flexible, compared to a Washington "drop-cap" one, in which the girders are seated on the first-stage cross beam. This would result in a nonuniform resistance of the seismic moment across the width of the superstructure. An effective width concept was used in order to quantify the superstructure resistance to seismic moment, and the researchers concluded that the majority of the seismic moment was resisted by girders in close proximity to the column.

As this study forms the basis of the WSDOT design practice, its validity was investigated for a typical Washington State cap beam.

1.3.2 Concrete Capacity Design (CCD) Approach - (Fuchs et al., 1995)

Studies were sought that would provide insight into the bearing stress that the strand anchor and plate could apply to the concrete. The work of Fuchs et al. (1995) provides some guidance, for both single strands and a group of strands.

A series of tension tests on headed steel studs, embedded in concrete blocks, were carried

out by Fuchs et al. (1995) and were used in the development of the Concrete Capacity Design (CCD) method. This method is used to predict the concrete capacity of steel anchors under tension, considering the influence of many different factors, such as the embedment depth of the fastening, the cracking of concrete, edge distance of the anchor, and the eccentricity of the applied load. It should be noted the methods for estimating the capacity of anchors under tension in ACI 318 and the PCI design hand book are based on the CCD approach. However, they have been made more conservative by considering cracked concrete properties, and a 5% fractile for test database, which forms the basis for the CCD method.

1.3.3 Spirally Confined Concrete Strength - (Richart et al., 1929)

The diaphragm concrete behind any strand anchor benefits from confinement by the surrounding concrete. To evaluate the effectiveness of that confinement, studies on the subject were sought. Owen (1998) provides an extensive bibliography on the subject. One of the first, and mostly widely referenced, research programs was conducted by Richart et al. (1929), who studied the effect of spiral confinement on the compression strength of reinforced concrete columns by carrying out a series of experiments. Based on the test results, an expression predicting the contribution of confinement to concrete compression strength was derived. That equation forms the basis for the confinement equation used in ACI 318.

1.4 Scope

The research program reported here evaluates the capacity of the extended strand connection at the most critical locations.

- In *Chapter 2* failure by crushing of the concrete behind the individual strand anchor is addressed.

- *Chapter 3* details the experimental procedures conducted in order to determine the possible failure mechanisms for groups of extended girder strands, anchored with strand

chucks, and embedded into the diaphragm. Analysis of the test results to predict system behaviour was also included.

- *Chapter 4* includes the development of different bridge superstructure computational models, used in determining the behaviour of the system under longitudinal seismic impact.

- *Chapter 5* summarizes the results of the bridge superstructure analyses and discusses the predicted system behaviour, recommending an amendment to the current design practice.

- *Chapter 6* offers further recommendations regarding the current girder-diaphragm connection detail used by WSDOT.

- *Chapter 7* provides a summary of all of the key findings of this thesis.

Chapter 2

CONFINED ANCHORAGE TESTS

2.1 Introduction

The positive moment seismic connection in precast prestressed concrete girder bridges is presently made by extending some of the bottom girder strands into the cast-in-place diaphragm. In this location, the space available is too small for development by bond in the straight strands alone. For this reason, the strands are usually anchored by bending or by being equipped with a strand anchor bearing on a steel plate. The size of the plate is presently based on the concrete strength, f'_c, ignoring the benefit of confinement. The relatively large plates lead to congestion and difficulties in erecting the girders. Since the concrete in the diaphragm is highly confined, it can probably carry high bearing stress and the use of a small bearing plate may be possible. Thus, in order to provide designers with the most versatility, the use of straight strands equipped with the smallest possible anchorage device is proposed.

The first stage in the development of the girder-diaphragm seismic connection consists of establishing the adequacy of the strand anchor capacity such that a ductile failure due to yielding and fracture of the strand is achieved before the strand anchor fails.

In order to check the strand anchor efficiency, tests on single chucks (anchors) attached to strand embedded in small concrete cylinders, confined to approximately the same extent as the concrete in the real diaphragm, were conducted. A summary of the tests is shown in Table 2.1.

Table 2.1: Confined Anchorage Test Summary

Concrete Batch	Anchor Type	Specimen Size	Number of Specimens	Test
A	Casting	6" x 6"	3	Compression
	Barrel	6" x 6"	3	
B	Barrel	6" x 6"	2	
		6" x 12"	1	
		6" x 6"	2	Tension

The test plan originally included strand chucks bearing on plates of different sizes, since the current detail includes 4"x4"x½" bearing plates behind the strand anchors. However, the first tests were conducted without plates and it was discovered that strand anchors without plates could resist the force of strand at fracture. Therefore, the tests that included bearing plates were eliminated from the schedule. The tests are described in detail in this chapter.

2.2 Experimental Setup

2.2.1 Specimen Design

Due to space limitations in the diaphragm, it is proposed that the bottom girder strands extending into the cap beam are anchored with anchors as small as possible. To that end, two types of strand anchors, namely, barrel anchors and anchor castings, were considered. Barrel anchors are typically used for applications where they bear against a steel plate. Casting anchors are widely used for unbonded strands in slabs, where they bear on concrete. Their greater bearing area leads to lower bearing stresses behind the anchor. The anchors and their dimensions are shown in Figure 2.1.

(a) Barrel Anchor

(b) Casting Anchor

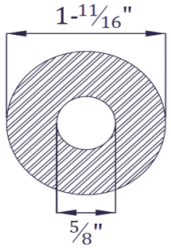

$A_b = 1.94\ in^2$

(c) Barrel Anchor Dimensions

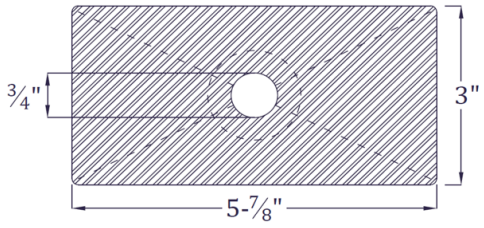

$A_c = 17.18\ in^2$

(d) Casting Anchor Dimensions

Figure 2.1: Anchors Used in the Tests

In order to test the reliability of the proposed detail, a single strand chuck, anchoring 0.6" strand and embedded in concrete, was tested. The first tests were conducted by pulling on a strand engaged in the chuck. It was found that the strand broke before the bearing interface incurred any damage, showing that the anchor was stronger than the strand. In order to find out how much stronger, subsequent tests were conducted by loading the chuck in compression from the opposite end.

The concrete was cast in a steel tube, in order to ensure highly confined concrete, much like the diaphragm concrete. Extensive research has shown that highly confined concrete can withstand stresses much higher than f'_c. For instance, Richart et al. (1929), Balmer (1949), Newman and Newman (1971) and Chuan-Zhi et al. (1987) carried out tests on biaxially and triaxially confined concrete cylinders and cubes in order to investigate the increase in axial load bearing capacity due to confinement. A more extensive summary of the aforementioned, as well as other previous research may be found in Owen (1998).

Thus, the concrete cylinders were confined by the steel tube, in order to simulate the

confined concrete behaviour in the diaphragm. The required thickness of the steel tube, was determined by performing a cylindrical pressure vessel analysis, assuming a thin walled cylinder.

Other research carried out by Hawkins (1968) has shown that bearing stresses can exceed f'_c without failure, even in unconfined concrete, if the load is applied over only a small part of the total surface area. This result is embodied in ACI318-11 Section 10.14 addressing concrete bearing strength, and in ACI381-11 Appendix D discussing steel headed studs, embedded in concrete, which allows stresses up to $8f'_c$ at the bearing area under the head of a stud, before local concrete crushing takes place (ACI318, 2011).

Assuming a load, 50% higher than the strand capacity needs to be resisted, a load of 90 kips was used for the analysis. The required strength of the confined concrete can be determined as shown in Equation 2.1.

$$f'_{bearing} = \frac{P}{A_b} \tag{2.1}$$

where

$A_b = 1.94$ in^2 is the net bearing area under the strand chuck,

$P = 90$ k is the applied load.

Thus, $f'_{bearing} = 44.7\ ksi$.

Since the concrete is under tri-axial compression, it is assumed that the expression derived by Richart et al. (1929) for confining stress provided by ties of spiral would be valid here.

$$f'_{bearing} = f'_c + 4.1f'_L \tag{2.2}$$

where

f'_c is the unconfined 28-day compressive strength of concrete (ksi),

f'_L is the lateral confining stress (ksi).

Thus, the required lateral confining stress, $f'_L = 9.6\ ksi$.

Finally, the hoop (circumferential) stress in a thin walled pressure vessel can be deter-

mined as follows.

$$\sigma_\theta = \frac{pR}{t} \tag{2.3}$$

where

p is the internal pressure (ksi), or in this case the lateral confining pressure f'_L,

and

t and R are the thickness and internal radius of the vessel (in), respectively.

So, considering the hoop stress σ_θ would be the yield stress of the vessel $f_y = 42\ ksi$ for HSS Grade B Steel,

$$f_y = \frac{f'_L R}{t} \tag{2.4}$$

This results in $t = 0.69$". The selected tube thickness was 0.5". The chosen thickness was less than that required theoretically because the beneficial effects of loading a small area had been ignored in the planning phase.

2.2.2 Concrete Mix

The concrete mix proportions were determined as per WSDOT standards for 4000 D class concrete, typically used in the diaphragm region. By reviewing mix designs used by WSDOT in previous projects it was ensured that the concrete used in the experiments would exhibit properties close to what the concrete on site would be. The mix proportions for the two concrete batches used in the experimental program are given in Table 2.2.

Table 2.2: Confined Anchorage Tests Concrete Mix Designs

	Cement Paste (lbs/cy)			**Aggregates (lbs/cy)**		**Admixtures (ml/100 lbs cement)**		
Concrete Batch	Water	Cement	Slag (GGBFS)	AASHTO #67	Building Sand	DARAVAIR 1000	Glenium 7500	MasterLife SRA 035
A	214.10	500.62	160.91	1732.22	1296.28	45	125	620
B	185.52	495.30	159.20	1714.12	1308.47	60	125	0

For the first batch of concrete (Batch A), three admixtures were used in the mix, namely, high range water reducer (Glenium 7500), air entrainer (DARAVAIR 1000) and shrinkage

reducer (MasterLife SRA 035). The air entraining agent was used to ensure that the lab concrete was not artificially strong. Class 4000D concrete is defined by a performance specification, rather than a specific mix design. The air entraining admixture was added to the mixing water of the concrete, while the super plasticizer and shrinkage reducer were added into the mixer while the concrete ingredients were being mixed. Despite these efforts to prevent the three substances from reacting with each other, upon testing the concrete, it was deemed that some sort of neutralization between the three took place during the mixing procedure. Ground-granulated blast-furnace slag (GGBFS) was also used as a substitute pozzolanic material, conforming to typical WSDOT mix design. Even though air- entraining admixture was used, the air content in the concrete was determined to be only 2.7%. The concrete slump test resulted in a 9.5" slump. 7 days after the concrete was cast, two 4"x 8" concrete cylinders were tested for compressive strength and the latter was determined to be 4850 psi. The concrete strength during testing was about 5400 psi.

New concrete mix proportions were determined for the second batch of concrete (Batch B) since the three admixtures used in the previous mix, namely, high range water reducer, air entrainer and shrinkage reducer, neutralized each other's effectiveness. For the new mix, it was decided to refrain from using the shrinkage reducer, and increase the amount of air entraining admixture to be close to the maximum allowed amount per WSDOT standards, thus resulting in a higher air content. The resulting concrete strength was smaller than the concrete strength of the first concrete batch, which is to be expected due to the increased air content. As a result, the air content in the concrete was determined to be 11%. The concrete slump was 7.4". 7 days after the concrete was cast, two 4"x 8" concrete cylinders were tested for compressive strength and the latter was determined as 4190 psi. The concrete strength during testing was determined as 4350 psi. The concrete was thus as weak as it could be while still meeting the requirements for class 4000D.

The mix properties for both concrete batches are summarized in Table 2.3.

Table 2.3: Confined Anchorage Tests Concrete Properties

Concrete Batch	Air Content (%)	Slump (in.)	Admixture			f '$_c$ (psi)	
			Air Entrainer	Water Reducer	Shrinkage Reducer	7-day	14-day
A	2.7	9.5	✓	✓	✓	4850	5400
B	11.0	7.4	✓	✓	×	4190	4350

2.2.3 Specimen Assembly and Preparation

Two slightly different specimen assemblies were used for the different batches of concrete. A schematic of the test specimens is shown in Figure 2.2.

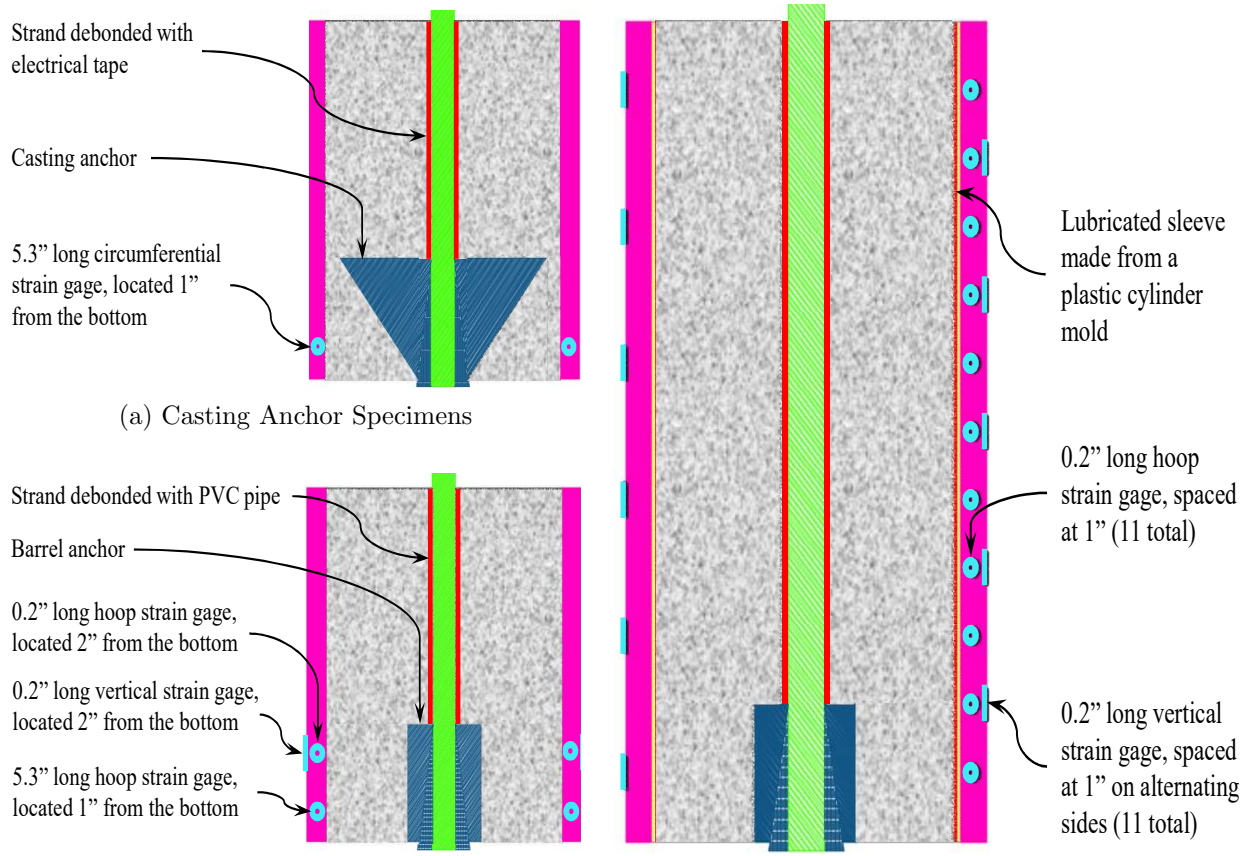

(a) Casting Anchor Specimens

(b) Barrel Anchor Specimens

(c) 6"x12" Cylinder Barrel Anchor

Figure 2.2: Specimen Schematics

The specimen assembly is shown in Figure 2.3.

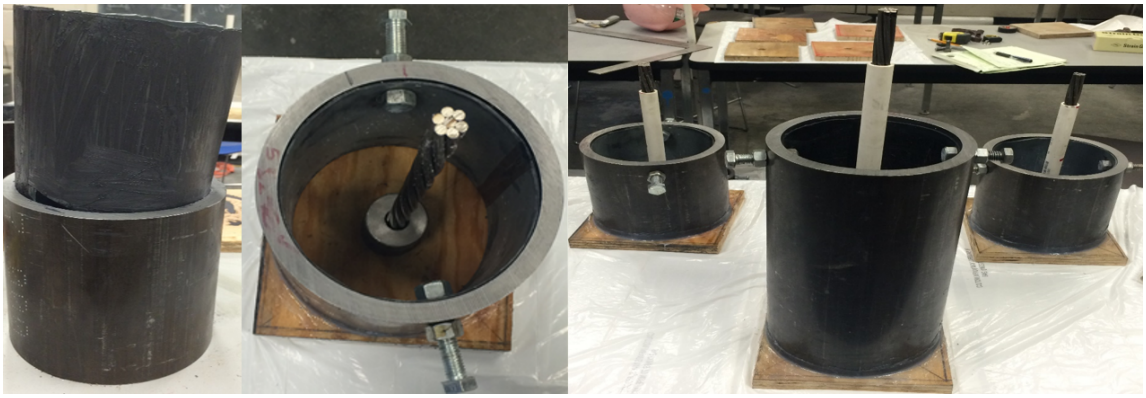

Figure 2.3: Specimen Assembly

Specimens from concrete Batch A included six 6"x 6" cylinders. The test specimens consisted of single strand, anchored with a strand chuck and embedded in concrete. The concrete was cast in round HSS7x0.5 steel tubes in order to replicate the concrete confinement in the diaphragm region. 0.6" diameter strand, anchored with either a barrel or a casting anchor, was placed in the middle of the steel tube with the anchor on the bottom. A portion of the wedge of the strand anchor, which had gripped on to the strand, was standing out by about 3/16". The tube was positioned on a plywood plate with a 1-3/8" diameter hole in its center to provide a smooth and level surface for casting by providing space for the strand chuck wedge that was sticking out. A bridge assembly comprised of a 1" thick, 8"x 1.5" wooden plate with a hole of 7/8" diameter the middle, held in place by 4"x 1" wooden plates attached to it, was used to center the strand and keep it straight it during casting. The strand was debonded from the concrete by using electrical tape. Each specimen had two 5.3" long circumferential strain gages, located 1" from the bottom on opposite sides of the steel tube.

Specimens from concrete Batch B included five 6"x 6" cylinders and one 6"x 12" cylinder. A few variations were made to the specimen assembly compared to Batch A. Plastic cylinder molds greased on the outside were placed inside each steel tube in order to prevent the transfer of vertical forces from the concrete to the surrounding steel for all specimens from Batch B. The strands placed in all specimens were fully debonded by the use of PVC pipes as opposed to electrical tape used for the debonding of specimens from Batch A. Two 1/2"

diameter holes were drilled 1" from the top of the steel tubes in order to facilitate the moving of specimens, while ensuring a tight fit of the mold against the steel tube. This is shown in Figure 2.3. Six strain gages were placed on each 6"x6" specimen – two 5.3" long circumferential gages, located 1" from the bottom of the steel cylinder on opposite sides of the specimen, and two circumferential and two vertical 0.2" long strain gages, located 2" from the bottom of the specimen above the 5.3" long circumferential gages. Twenty-two 0.2" long strain gages were placed on the 6"x12" specimen – 11 circumferential and 11 vertical. Since all of the vertical gages would not fit in one line, the gages were placed in two parallel lines of 6 and 5 gages, respectively. The strain gage configurations are shown in Figure 2.2, where the circumferential gages are represented by circles and the vertical gages are represented by vertical line segments.

After casting, the specimens were turned upside down, such that the strand anchor was on top; then, a hydrostone layer of approximately 0.7" thickness was cast under each specimen, in order to create a level surface during testing. This is shown in Figure 2.4.

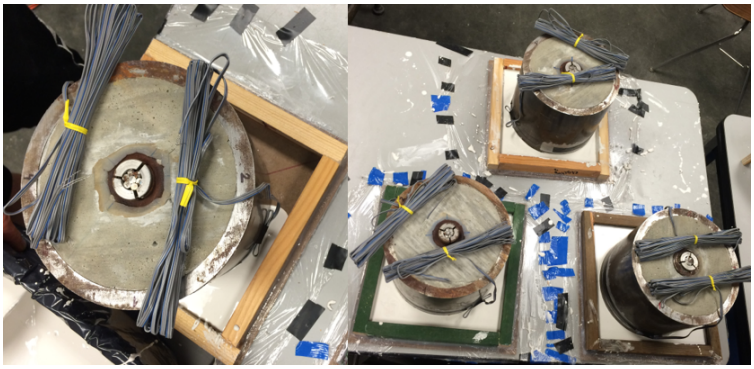

Figure 2.4: Hydrostone Casting

2.3 Testing Procedures

The specimens were initially tested by loading a strand, which was engaged in a chuck, in tension as discussed in Section 2.3.1. However, assuming the strand anchor is stronger than the strand and the (desired) ductile failure mode would be achieved by the fracture of the strand, performing only tension tests would stand in the way of obtaining knowledge about

the capacity of the strand chuck. Also, since the location of interest is the area of concrete bearing on the bottom face of the anchor inside the cylinder, the forces are transferred such that the bottom anchor surface, and the strand anchor wedge, located on the opposite side of the anchor, would both be under compression regardless of whether a tensile load is applied through pulling the anchored strand, or a compressive load is applied directly on the chuck body. Thus, it was deemed appropriate to test the anchors in compression in order to determine their capacity.

2.3.1 Tension Tests

The tension test setup is shown in Figure 2.5.

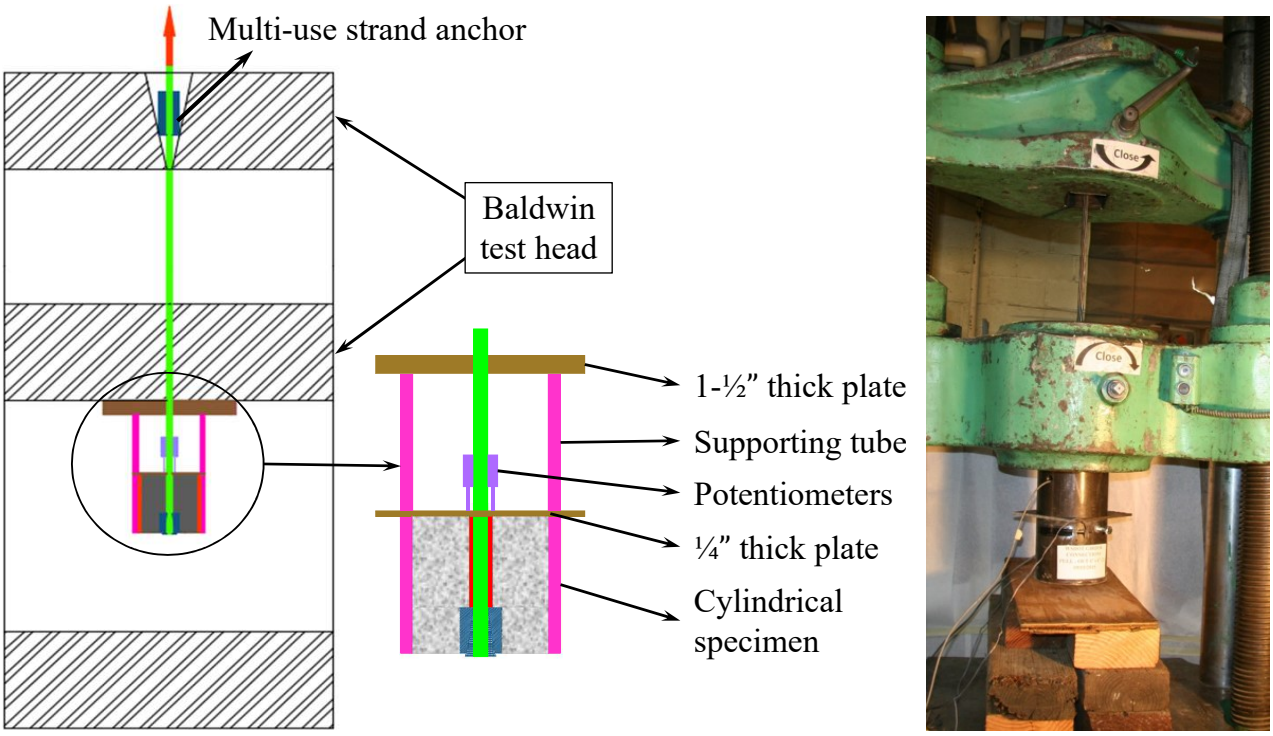

(a) (b)

Figure 2.5: Tension Test Setup

A ¼" thick rectangular plate was placed on top of each 6"x 6" specimen, then a hollow 6" long, 6" ID steel tube was placed above thar. A 1-½" thick 7"x 7" steel plate was placed on top of the supporting hollow tube. The specimens were then placed on top of wooden

blocks, in order to be lifted high enough for the plate to fit underneath the bottom head of the Baldwin test machine. Then, a multiuse strand chuck was attached to the free end of the strand and caught in between the top Baldwin head clamps. The tensile load was applied by moving the top test head while the lower remained stationary. Two potentiometers were glued on the strand. Two specimens from concrete Batch B were tested in tension. All the other specimens were tested in the compression configuration.

2.3.2 Compression Tests

The schematic compression test assembly for specimens from concrete Batch A is shown in Figure 2.6.

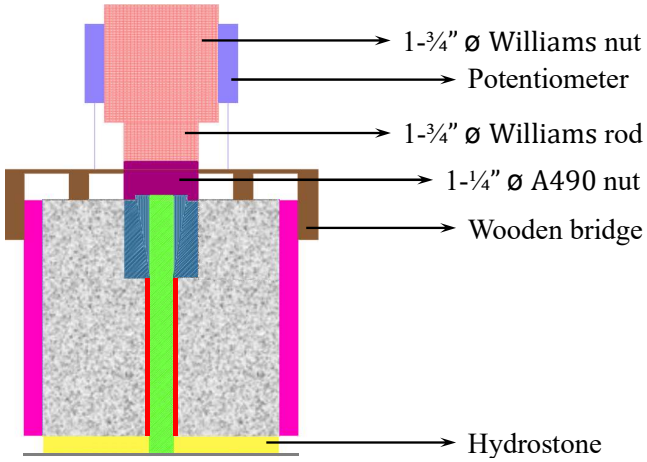

Figure 2.6: Schematic Compression Test Assembly Batch A

In all cases a base was present only under the concrete on the bottom of the specimen, excluding the bottom of the steel tube, with the goal of ensuring that the steel cylinder provided only radial stress to confine the concrete by preventing the transfer of vertical stresses from the concrete along the walls of the steel tube. Hydrostone, a quick-setting high strength gypsum paste, was used as a supporting pad for the concrete and was also cast in order to provide a level bottom surface for the specimens.

Compression tests were carried out on all six 6"x 6" specimens from concrete Batch A. The variations in the test assemblies for Batch A specimens are shown in Table 2.4.

Table 2.4: Batch A Test Setup Variations

Specimen	Loading Assembly	Load Application Point	Test Setup
Barrel Anchor 1 (6"x6")	**1¾" rod**	**Wedge**	
Barrel Anchor 2 (6"x6")	**1-¾" rod + 1-¼" nut**	**Chuck Body**	
Barrel Anchor 3 + Casting Anchors 1, 2, & 3 (6"x6")	**1-¾" rod + 1-¼" nut + ¾" plate**	**Chuck Body**	

The load application assembly changed slightly between tests, until the best method was decided on. The initial testing procedure was as follows. All specimens were placed on the testing machine plateau sitting on the hydrostone with the anchors (barrel or casting) on top. While testing the first specimen, a 1-¾" diameter Williams rod ($f_u = 150$ ksi) with a nut was used to apply the compression load directly on the wedge of the strand anchor. The rod was centered by a bridge assembly comprised of a 2" thick, 8"x 4.5" wooden plate with a hole of 1-⅞" diameter the middle, held in place by 4"x 2" wooden plates attached to it. Two potentiometers were attached to the rod in order to measure the anchor displacement during the test.

The loading assembly was changed at the end of the first test, since part of the deformation measured was due to the wedge (which was standing out by about 3/16") being pushed

into the chuck. A 1-¼" diameter ASTM A490 nut was placed over the chuck body, covering the wedge and the 1-¾" rod was placed on top of the nut, in which manner the load would be applied onto the chuck body. The nut served as a high-strength tube through which the load was delivered to the barrel (and not the wedge) of the strand anchor.

At the end of the second test, the 1-¾" Williams rod, as well as the 1-¼" ASTM A490 diameter nut beneath it used to to apply the load had both yielded and deformed. Hence, the final version of the loading assembly was to place a ¾" thick plate between the loading rod and the 1-¼" diameter A490 nut. The damage (by local yielding) was then limited to the plate, and this resulted in better alignment of the load train components.

In the first series of tests for specimens from Batch A, discussed above, the displacements measured were partly due to the yielding of the loading rod, nut and plate, as well as the chuck top surface. Thus, a new testing assembly was created for the specimens from batch B as shown in Figure 2.7.

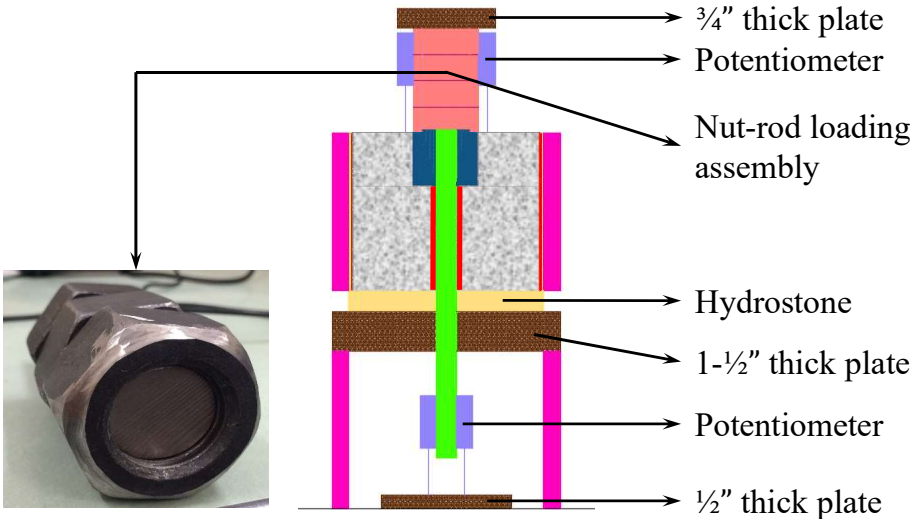

Figure 2.7: Schematic Compression Test Assembly Batch B

Push tests were carried out on three 6”x 6” specimens, as well as on the 6”x 12” specimen from concrete Batch B. The variations in test setups for Batch B are summarized in Table 2.5.

Table 2.5: Batch B Test Setup Variations

Specimen	Barrel Anchor 4 (6"x6")	Barrel Anchor 5 (6"x6")	Barrel Anchor 6 (6"x12")
Loading Asssembly	(4) 1¼" nuts + ¾" plate	(5) 1¼" nuts + ¾" plate	(5) 1¼" nuts + ¾" plate
Load Application Point	Chuck Body	Chuck Body	Chuck Body
Test Setup			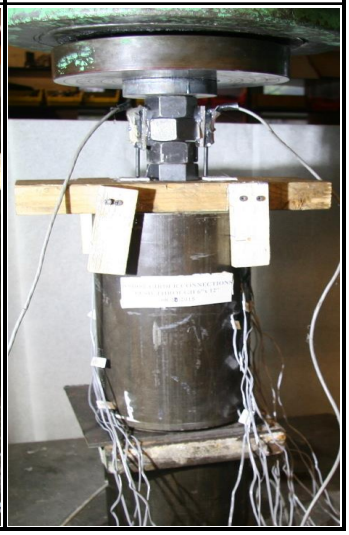

The initial test setup was as follows. A hollow 6” long, 6” ID supporting steel tube with a hole in the side was placed on the test machine surface. A 1-½” thick, 7”x 7” steel plate with a 1-½” diameter hole in the middle was placed on top of the hollow steel tube. The test specimen was placed on top of the 1-½” thick steel plate, with the strand extending down the hole and into the supporting tube by approximately 6”. Two potentiometers were glued to the strand in the hollow tube, their wires extending through the holes in the supporting tube. The purpose was to measure the movement of the body of the strand anchor relative to the concrete, without including the deformation of the load train. The strand acted as a

push rod for the potentiometers. The potentiometers rested on a plate with ½" thickness, placed in the middle of the supporting tube on the bottom of the assembly.

In order to ensure that the load is being applied to the chuck body and wedge simultaneously, replicating the actual loading scenario as closely as possible, a piece of high strength rod with four 1-¼" diameter A490 nuts tightened onto it (nut-rod loading assembly) was used to apply the load. The ¾" thick plate, connected to the Baldwin was placed on top. The nuts were kept in place by a bridge assembly comprised of a 2" thick, 8"x 4.5" wooden plate with a hole of 1 ⅞" diameter the middle, held in place by 4"x 2" wooden plates attached to it. Two potentiometers were attached to the nut-rod loading assembly in order to measure the chuck displacement during the test.

Since the potentiometers detached from the 4 A490 nut - high strength rod loading assembly during the course of the test, it was decided to include 5 A490 nuts for the second compression test. Furthermore, since the steel plate, used between the supporting tube and the testing specimen had a hole larger than the 0.6" strand diameter, a sort of concrete flow was observed during the test, as the concrete crushed through the hole in the plate. This is discussed in detail in Section 2.4. Hence, a ¼" thick rectangular plate with ¹³⁄₁₆" diameter hole was used, to minimize the space around the strand. This revised test setup was used for the 6"x 12" specimen.

2.4 Test Results

The results from all compression and tension tests are summarized in Table 2.6.

P_{max} refers to the maximum load but that does not mean the load at failure, just the maximum applied load for each test. The values of the anchor displacements relative to the concrete were measured after the tests were concluded by using a caliper. These displacements roughly reflect the rigid body motion of the strand chuck, excluding the deformations due to yielding of the loading assembly and are not the same as the displacements of the testing assembly, which were recorded by potentiometers.

Table 2.6: Confined Anchorage Test Results

Anchor	Specimen	P_{max} (kips)	Anchor Displacement (in)	Test
Barrel Anchor	TBA[1] 1	55.3	-	Tension
	TBA 2	58.1	-	
	CBA[2] 1	249.3	-	Compression
	CBA 2	205.6	0.28	
	CBA 3	220.5	0.22	
	CBA 4	193.5	1.51	
	CBA 5	200.4	0.72	
	CBA 6	225.3	0.61	
Casting Anchor	CCA[3] 1	199.7	0.06	
	CCA 2	204.7	0.05	
	CCA 3	212.7	0.08	

[1]TBA = Barrel Anchor in Tension
[2]CBA = Barrel Anchor in Compression
[3]CCA = Casting Anchor in Compression

The specimens for which no plastic mold was used to debond the concrete from the steel tube (Specimens CBA and CCA 1,2 and 3), a barrel anchor displacement of about 0.25" corresponding to a load of about 200 kips was recorded. Specimens, for which greased plastic molds were used to debond the concrete from the surrounding steel tube (specimens CBA 5-6), a barrel anchor displacement of about 0.66" for a load of about 200 kips was measured. The reason behind the high barrel anchor displacement of 1.5" for specimen CBA 4, which also included a greased plastic mold, is discussed later in detail. The casting anchor displacements were much smaller than those of barrel anchors, which is to be expected due to the much higher bearing area.

2.4.1 Tension Test Results

Post-test photos of the barrel anchor tension specimen tests are shown in Figure 2.8.

(a) TBA 1 (b) TBA 2

Figure 2.8: Barrel Anchor Tension Test Specimens

Both specimens failed due to strand fracture prior to the occurrence of any damage to the strand anchor or the surrounding concrete.

2.4.2 Compression Test Results

The barrel anchor compression test specimens post testing are shown in Figures 2.9a to 2.9f.

For Specimen CBA 1, the load was applied on the wedge of the anchor. Thus, the recorded displacement included both the displacements of the anchor body into the concrete, and of the wedge into the anchor. Due to applying the load on the anchor wedge, less local crushing of the concrete was observed as the loading rod was not in direct contact with the concrete. In addition, the steel tube was greased prior to the casting of concrete, but it is likely that did not completely debond the concrete from the steel.

(a) CBA 1

In Specimen CBA 2, more local concrete crushing was achieved since a 1¼" diameter A490 nut was used to apply the load on the chuck body, as opposed to the anchor wedge. The loading nut and rod yielded by the end of the test. The steel tube was greased prior to concrete casting.

(b) CBA 2

In Specimen CBA 3, a ¾" plate was added on top of the loading 1¼" diameter A490 nut in order to prevent it from yielding. The load was still applied to the anchor body and approximately the same amount of local crushing as in Figure 2.9b was observed. The steel tube was greased prior to concrete casting.

(c) CBA 3

Beginning with Specimen CBA 4, and continuing through Specimen CBA 6, the concrete was cast in plastic molds, placed in the greased steel tube in order to debond the concrete from the tube and prevent the transfer of axial stresses from the concrete through the steel tube. The goal was that the tube would only act as a confining presence and all the vertical stress would all pass down through the concrete, without axially engaging the tube. Two ½" diameter holes were drilled 1" from the top (while casting) of each specimen, in order to ensure a tight fit between the plastic mold and the surrounding steel tube, while providing an effortless way of lifting the specimen, using bolts, going through the holes, with nuts on the inside of the steel tube, embedded into the concrete. Similarly, for Specimens CBA 4, 5 and 6, the load was applied using a high strength threaded rod with A490 nuts as shown in Figure 2.7.

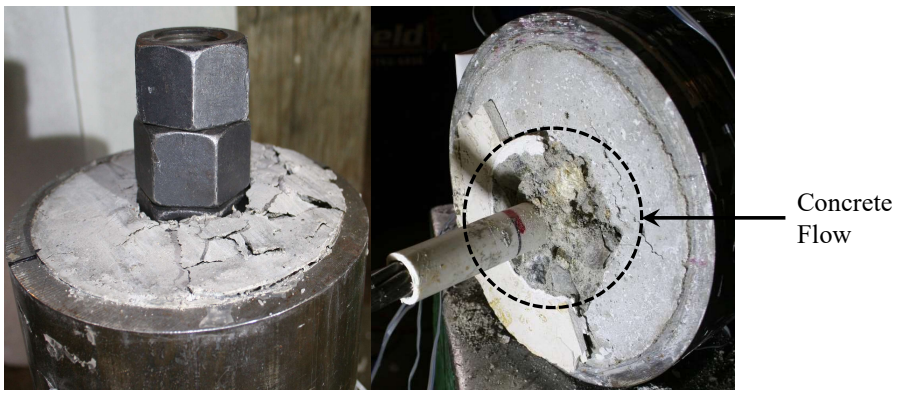

(d) CBA 4

A supporting steel tube was used as shown in Figure 2.7. An assembly comprised of a high-strength rod with (4) 1-¼" diameter A490 nuts was used to apply the load. Two of them locally crushed the concrete, embedding themselves in it completely, while displacing the anchor significantly. This happened due to the fact that a 1-½" thick plate with a 1-½" diameter hole in the middle was used between the specimen and the supporting tube, which lead to a concrete flow through the 1-½" plate hole as illustrated in Figure 2.9.

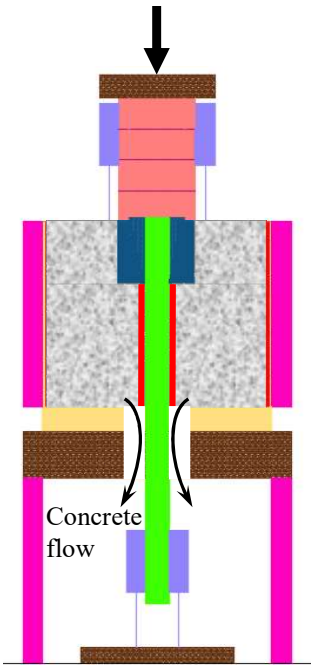

Figure 2.9: Specimen CBA 4 Concrete Flow

After the test, the concrete around the barrel anchor was removed in order to examine what had occurred beneath the anchor. A region of crushed concrete shaped like a washer with an approximate thickness of 2 mm was discovered directly underneath the anchor. Other than that, the concrete around and under the anchor appeared to be undamaged.

In order to prevent the concrete flow observed in Figure 2.9d, a ¾" thick plate was added on top of the 1-½" thick plate in the loading assemblies of Specimens CBA 5 and CBA 6. Thus, the local crushing of the concrete was less severe, as its vertical displacement capacity was inhibited. The local crushing is still more severe when compared to Figures 2.9b and 2.9c, due to the presence of the supporting tube, as well as the debonding of concrete.

(e) CBA 5

(f) CBA 6

Figure 2.9: Barrel Anchor Compression Test Specimens

It is believed that the presence of the plastic sleeve in the steel cylinder provided some radial flexibility. As the concrete moved radially outwards, it allowed more vertical displacement of the strand anchor.

The casting anchor specimens after compression tests are shown in Figure 2.10.

The steel tube was greased prior to concrete casting but no plastic mold was used. The load was applied to the chuck body via A490 nuts and no local concrete crushing was observed at the end of any of the casting anchor tests.

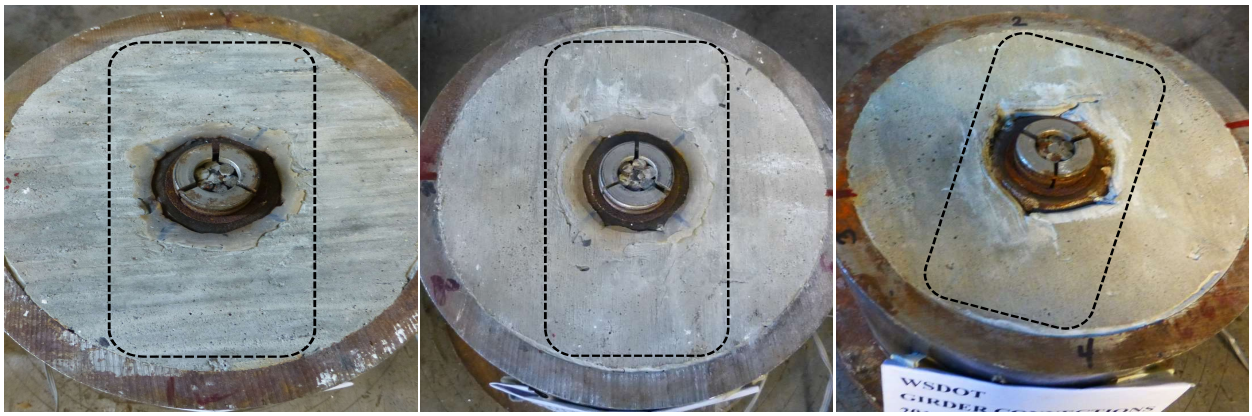

(a) CCA 1 (b) CCA 2 (c) CCA 3

Figure 2.10: Casting Anchor Compression Test Specimens

2.5 Analysis of Results

2.5.1 Summary of Results

The loads obtained from all barrel anchor tests are shown in Figure 2.11.

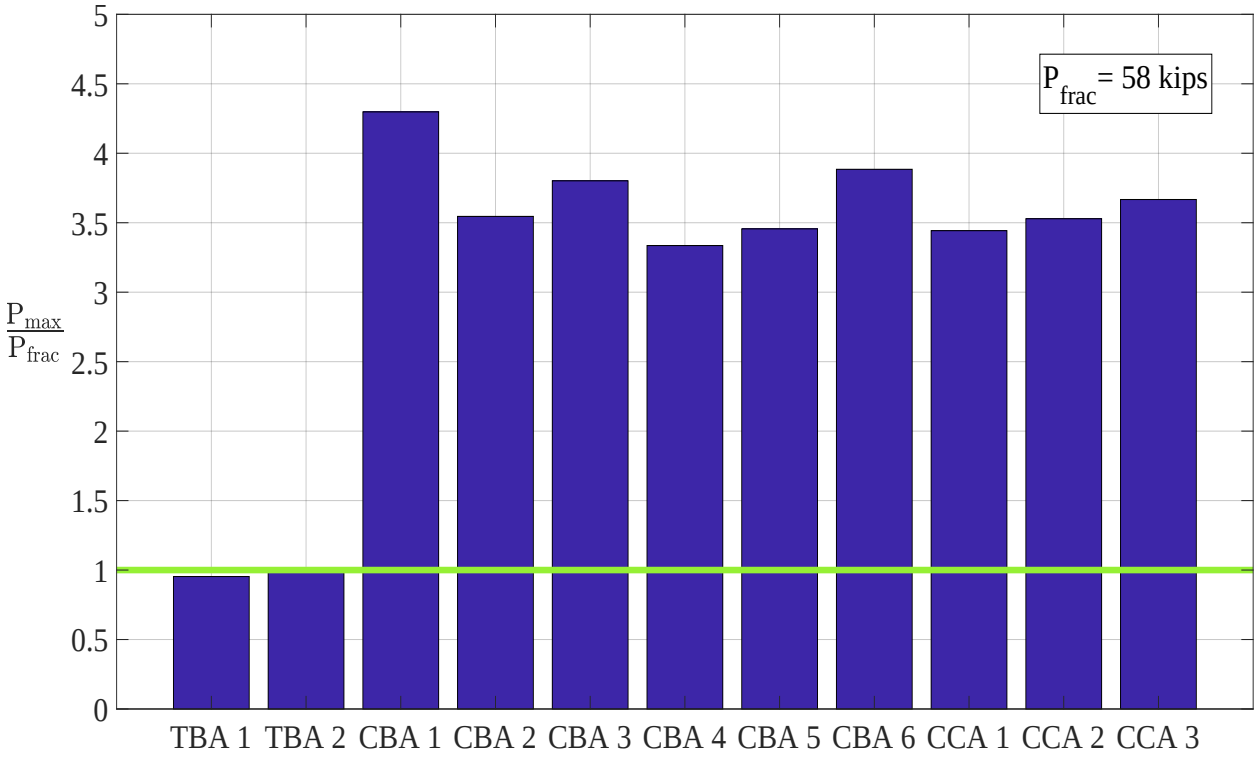

Figure 2.11: Barrel Anchor Tests Summary

Since the maximum loads obtained from the casting anchor tests were very close to the barrel anchor maximum loads, they do not provide any additional contribution. Furthermore, the casting anchors have large dimensions and are much heavier, thus the use of barrel anchors would be preferred for facilitation of constructability.

The maximum loads obtained from the barrel anchor compression tests were about 4-4.5 times the fracture load of the strands. Even under these high loads very little local concrete crushing was observed and the tests were stopped because of yielding in the steel load train. Thus, it was deemed appropriate to further investigate this phenomenon.

The main quantities of interest obtained from the barrel anchor and casting anchor tension and compression tests are summarized in Tables 2.7 and 2.8, respectively.

Table 2.7: Analysis of Barrel and Casting Anchor Tension Test Results

Test	P_{max} (kips)	f'_c (psi)	$f'_{bearing}$ (ksi)	ε_{vert} (με)	ε_{hoop} (με)	σ_{hoop} (ksi)	f'_L (ksi)	$\frac{f'_{bearing} - f'_c}{f'_L}$
TBA[1] 1	55.30	5400	28.66	-	168.7	5.377	0.896	25.95
TBA 2	58.06		30.09	-	40.28	1.284	0.214	115.4

[1]TBA = Barrel Anchor in Tension

Table 2.8: Analysis of Barrel and Casting Anchor Compression Test Results

Test	P_{max} (kips)	f'_c (psi)	$f'_{bearing}$ (ksi)	ε_{vert} (με)	ε_{hoop} (με)	σ_{hoop} (ksi)	f'_L (ksi)	$\frac{f'_{bearing} - f'_c}{f'_L}$
CBA[1] 1	249.3	5400	129.2	-	578.1	18.42	3.070	40.31
CBA 2	205.6		106.6	-	536.4	17.09	2.849	35.51
CBA 3	220.5		114.3	-	748.9	23.86	3.977	27.37
CBA 4	193.5	4700	100.3	-158.3	577.0	16.87	2.812	33.98
CBA 5	200.4		103.9	-103.3	591.4	17.86	2.977	33.32
CBA 6	225.3		116.8	-165.3	873.4	26.25	4.375	25.61
CCA[2] 1	199.7	5500	11.62	-	249.9	7.962	1.327	4.613
CCA 2	204.7		11.91	-	290.8	9.267	1.544	4.151
CCA 3	212.7		12.38	-	324.0	10.32	1.721	3.997

[1]CBA = Barrel Anchor in Compression

[2]CCA = Casting Anchor in Compression

The ratio between the bearing stress and lateral confining stress for each test, as shown in Tables 2.7 and 2.8, is important in evaluating the effectiveness of the confinement. The bearing stress was obtained from the peak load and the contact area between the anchor and the concrete, which was 1.94 in^2 for the barrel anchors and 17.18in^2 for the casting anchors. The lateral confinement stress was obtained from the stress in the steel tube, which was, in turn, obtained from the strain gage readings, using 3-D Hooke's law as shown in Equation 2.5.

$$\sigma_\theta = \frac{E_s}{(1+\nu)(1-2\nu)}\Big[(1-\nu)\epsilon_\theta + \nu(\epsilon_r + \epsilon_z)\Big] \tag{2.5}$$

where subscripts r, θ and z refer to the radial, circumferential and axial directions, respectively. Specimens CBA 1,2 and 3 had a pair of circumferential gages on opposite sides, located at 5" from the top of the specimen on the outside of the steel surface. The vertical strains for those specimens were assumed to be zero, since they were not recorded. In later specimens where the vertical strains were recorded, it was confirmed that they were smaller than the recorded circumferential strains by approximately a magnitude of 5. Thus, it was deemed appropriate to use vertical strains of zero for the specimens from Batch A. The radial strains were determined by using 3-D Hooke's Law and assuming $\sigma_r = 0$ on the outer surface of the steel tube as shown in Equation 2.6.

$$\begin{aligned} 0 &= (1-\nu)\epsilon_r + \nu(\epsilon_\theta) \\ \epsilon_r &= \frac{-\nu}{1-\nu}\Big[\epsilon_\theta\Big] \end{aligned} \tag{2.6}$$

Specimens CBA 4 and 5 had a pair of circumferential gages, located 5" from the top of the specimen, and a pair of circumferential strain gages, as well as a pair of vertical strain gages, located at 4" from the top of the specimen. Thus, for those specimens the radial strain was determined as follows.

$$\begin{aligned} 0 &= (1-\nu)\epsilon_{radial} + \nu(\epsilon_\theta + \epsilon_z) \\ \epsilon_r &= \frac{-\nu}{1-\nu}\Big[\epsilon_\theta + \epsilon_z\Big] \end{aligned} \tag{2.7}$$

Upon determining the radial strains, the radial stresses on the inside of the steel tube were determined by using Equation 2.8.

$$\sigma_r = \frac{E_s}{(1+\nu)(1-2\nu)}\Big[(1-\nu)\epsilon_r + \nu(\epsilon_\theta + \epsilon_z)\Big] \tag{2.8}$$

Assuming a thin walled cylindrical pressure vessel,

$$\sigma_\theta = \frac{pR}{t} \tag{2.9}$$

where

p is the internal pressure, which is in this case the lateral confining stress, f'_L,

$R = 3$" is the internal radius of the steel tube and

$t = 1/2$" is the thickness of the steel tube.

The lateral confining stress on the concrete is equal to the radial stress at the inner surface of the steel cylinder and is given by Equation 2.10.

$$f'_L = \sigma_r = \frac{t\sigma_\theta}{R} \tag{2.10}$$

Concrete is commonly treated as satisfying a Mohr-Coulomb failure criterion, in which case the strength of confined concrete can be determined from

$$\begin{aligned} f'_{cc} &= f'_c + c_L f'_L \\ f'_{cc} &= f'_c + \frac{(1+sin\phi)}{(1-sin\phi)} f'_L \end{aligned} \tag{2.11}$$

where ϕ is the internal angle of friction.

Selecting $\phi = 37°$ returns the result found experimentally by Richart, Brandtzaeg and Brown shown in Equation 2.12 (Richart et al., 1929).

$$f'_{cc} = f'_c + 4.1 f'_L \tag{2.12}$$

The coefficient c_L indicates the effectiveness of the confinement, which, according to the Mohr-Coulomb theory, depends on the internal friction angle. For each test result, a value of c_L for use in Equation 2.11 can be calculated by treating the bearing stress, $f'_{bearing}$, as the confined concrete strength, f'_{cc}, to give

$$c_L = \frac{f'_{bearing} - f'_c}{f'_L} \tag{2.13}$$

Values of c_L are given in Tables 2.7 and 2.8 and may be compared with the 4.1 found by Richart et al. (1929). For the barrel anchors tested in tension, the comparison is not really valid, because the concrete had not started to crush significantly by the time the strand failed and the test was stopped. Thus, the resisting mechanism was still partially elastic, and was not the sliding shear one that underlies the Mohr-Coulomb theory. The c_L values for the casting anchors are comparable to those found by Richart et al.(Richart et al., 1929). The c_L values for the barrel anchors tested in compression are about an order of magnitude higher than Richarts, which suggests that some other beneficial mechanism, in addition to the conventional confinement, was active. It is believed that the bearing stress was high because the bearing load was applied over only a small proportion of the total available area. Even though this behavior has been seen before (Hawkins, 1968) and is incorporated in codes (ACI318 (2011) Chapter 10 and Appendix D), good mechanical models for it are not yet available.

Even though these c_L values from the bearing anchor compression tests are high, they are still lower bounds, because the bearing stress measured in the test was a lower bound to the true failure stress.

The tests had to be stopped because the ASTM A490 nut and the Williams bar used in the load train were deforming plastically, and not because the concrete was failing.

The strains in the steel tube varied over the height of the tube. This was seen in Specimen CBA 6, which was 12" high, and was equipped with 11 circumferential and 11 vertical strain gages, measuring the strains at every inch along the height of the steel tube. However, for the other specimens, the strains had to be read where gages were available. In specimens CBA 4 and CBA 5 (6" high), the hoop strains were taken as the average of gage readings 5" and 4" from the top of the specimen, respectively; and the vertical strains were taken as the average of the gage readings 4" from the top of the specimen. Those heights were approximately where the maximum strains were observed in Specimen CBA 6.

Specimens CBA 1,2 and 3 were also constructed with 6" high tubes, with only circumferential gages 5" from the top of the specimen and were placed there because that location was expected to experience approximately the maximum strain. The lateral confining stress is thus a local value at the inside of the steel tube, at approximately the location of the maximum value, and so some variation in results should be expected. However, the average value of c_L was 33, with a Coefficient of Variation of 17%.

2.5.2 6"x6" Cylinder Tension Tests

The load-displacement relationships for the barrel anchor tension tests are shown in Figure 2.12.

As a reminder, a plastic sleeve was used to debond the concrete from the steel tube for both specimens TBA 1 and TBA 2.

The elastic displacement of the strand was obtained as follows.

where

$$\Delta_{elastic} = \frac{PL_p}{A_p E_p} \qquad 2.14$$

P is the applied load, considered to be ranging from 0 to 60 kips,

$A_p = 0.217\ in^2$ is the cross-sectional area of 0.6" diameter strand,

$E_p = 28000\ ksi$ is the modulus of elasticity of the strand,

$L_p = 6.5$" is the length of the strand.

Thus, the elastic displacement of 0.6" diameter strand would be 0.06" at about 55 kips, resulting in a plastic deformation of about 0.05". for TBA 2 and 0.29" for TBA 1. Specimen TBA 1 was subjected to two loading cycles. During the first loading cycle, a test setup malfunction took place preventing strand fracture from occurring. Consequently, a second loading cycle was conducted, during which strand fracture was achieved. However, while the stiffness of Specimen TBA 1 was drastically reduced, the ultimate strand capacity was similar to that of Specimen TBA 2.

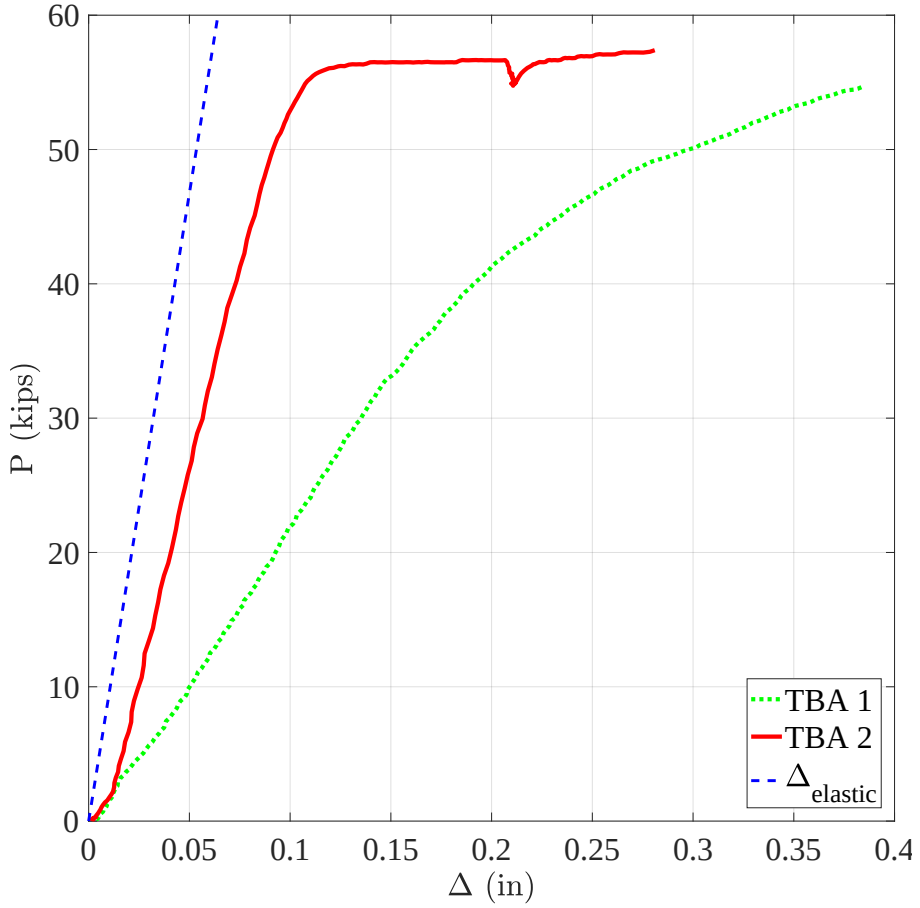

Figure 2.12: Load vs Displacement Barrel Anchor Tension Tests

2.5.3 Compression Tests

The displacement values obtained from the potentiometers during the tests are compared by illustrating the load-displacement relationship for all compression tests in Figure 2.13.

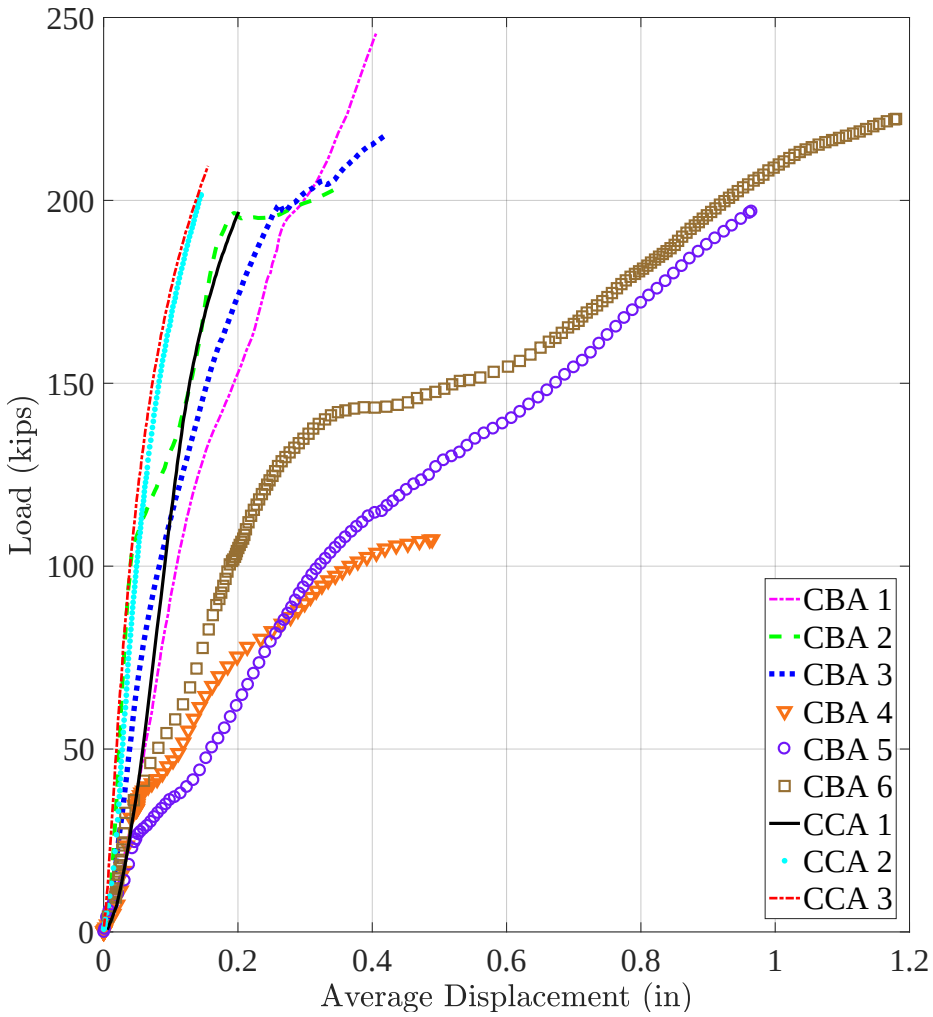

Figure 2.13: Load vs Average Displacement Compression Tests

The displacements for the bonded barrel anchor specimens CBA 1, CBA 2 and CBA 3 are about 0.4" at the maximum load levels; however it should be kept in mind that part of the displacement detected by the potentiometers was due to the yielding of the nut and rod loading assembly, as well as due to the yielding of the chuck top surface. Thus, the displacements of the chuck body relative to the concrete would be smaller.

If one is to consider a load of about 60 kips (which would be the failure load in practice), the largest displacement, which occurred for specimen CBA 1 is about 0.07".

The debonded barrel anchor specimens, namely, CBA 4, CBA 5 and CBA 6, experience much larger displacements at the maximum load levels. The reason why the maximum observed displacement for specimen CBA 4 is about 0.5" is because when the concrete flow occurred, the instruments recording the displacement were damaged.

Overall,the maximum displacements were larger due to the debonding of the concrete from the steel tube, by the use of plastic molds. This allowed radial displacement of the concrete to occur where any gaps between the plastic mold and the steel tube may have existed. This behaviour was confirmed by the fact that grease squeezed through the gap between the plastic mold and the steel tube during the tests. Additionally, radial compression of the plastic sleeve inside the steel tube likely took place. Ultimately, the debonding also allowed the free top concrete surface around the anchor to heave more easily when compared to bonded specimens.

Based on the barrel anchor compression test results, at a load of about 60 kips (which would be the failure load in practice) a displacement in the range between 0.15" - 0.2" is to be expected, proving the barrel anchor performance is satisfactory and indicating that this detail does not only have sufficient capacity in terms of strength, but will also not experience significant slipping.

For the bonded barrel anchor specimens CBA 4, CBA 5 and CBA 6, a pair of potentiometers were attached to each A490 nut in the load train, and to each strand as shown in Figure 2.7. The displacement values recorded for the nuts and the strands were very close as shown in Figure 2.14.

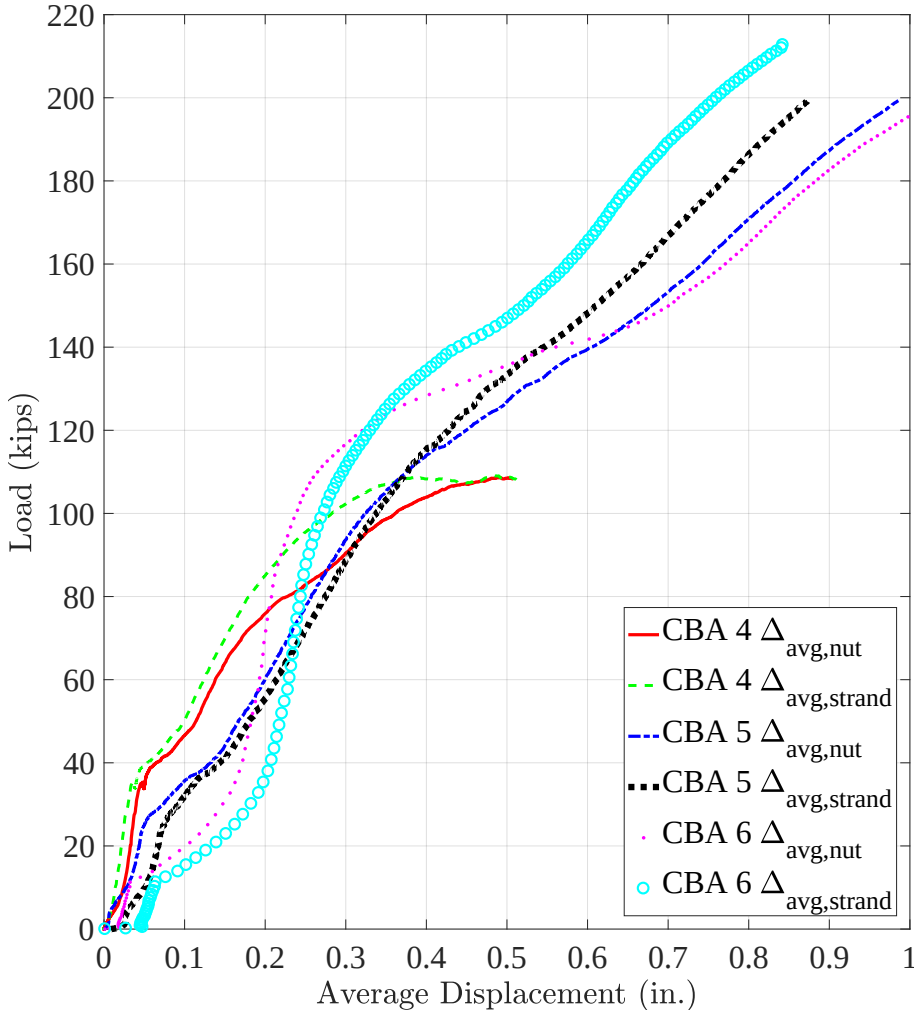

Figure 2.14: Load vs Average Displacement Debonded Barrel Anchor Specimens

The potentiometers glued to the A490 nuts used for loading and the ones glued to the strands gave similar results, leading to the conclusion that the obtained displacements were reasonably well captured.

Specimens CBA 1, CBA 2, CBA 3, CCA 1, CCA 2 and CCA 3 had only two potentiometers, attached on the 1-¼" diameter Williams nut, used to apply the load as shown in Figure 2.6.

Ultimately, the use of the nut displacement values was deemed appropriate for all compression specimens.

The load-strain relationships for all compression tests are shown in Figure 2.15.

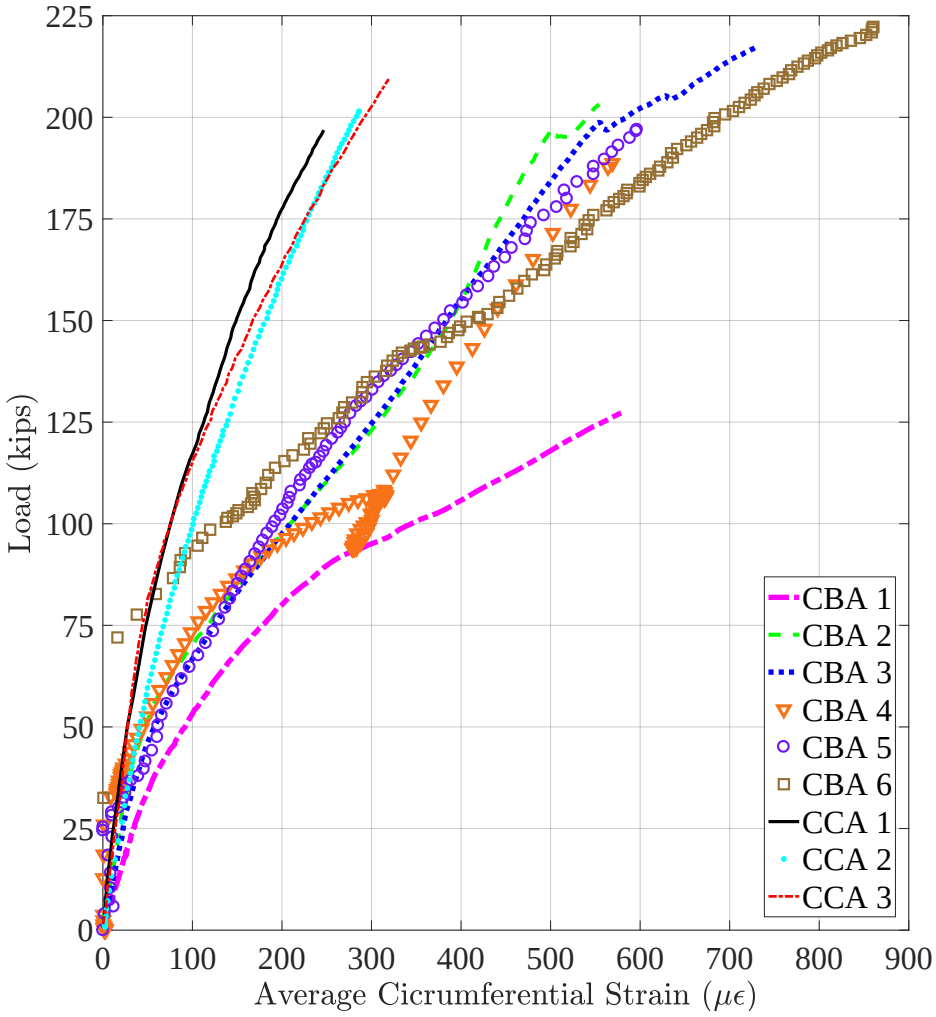

Figure 2.15: Load vs Average Hoop Strain Compression Tests

As previously mentioned, the casting anchor hoop strains are approximately half of the barrel anchor specimens' strains. They are certainly expected to be smaller, because the distribution of load at the point of application is more uniform, however, computing the expected ratio would be complicated.

The average strain values for the bonded specimens CBA 4, CBA 5 and CBA 6 were similar to those obtained from the other barrel anchor tests. The jump that occurs at about 108 kips for specimen CBA 4 could have been caused by the concrete flow; a sudden drop in the load took place possibly as the concrete started squeezing out and after several seconds, the specimen started picking load again.

For Specimens CBA 4 and CBA 5 (6"x 6"), unbonded with the use of plastic cylinder molds, only the long circumferential strain gage readings were used, when comparing their behaviour to the bonded Specimens CBA 1, CBA 2, CBA 3, CCA 1, CCA 2, and CCA 3 (6"x 6"). This was done for the sake of consistency between results. The long and short hoop strain values were fairly close for Specimens CBA 4 and CBA 5 as shown in Figure 2.16.

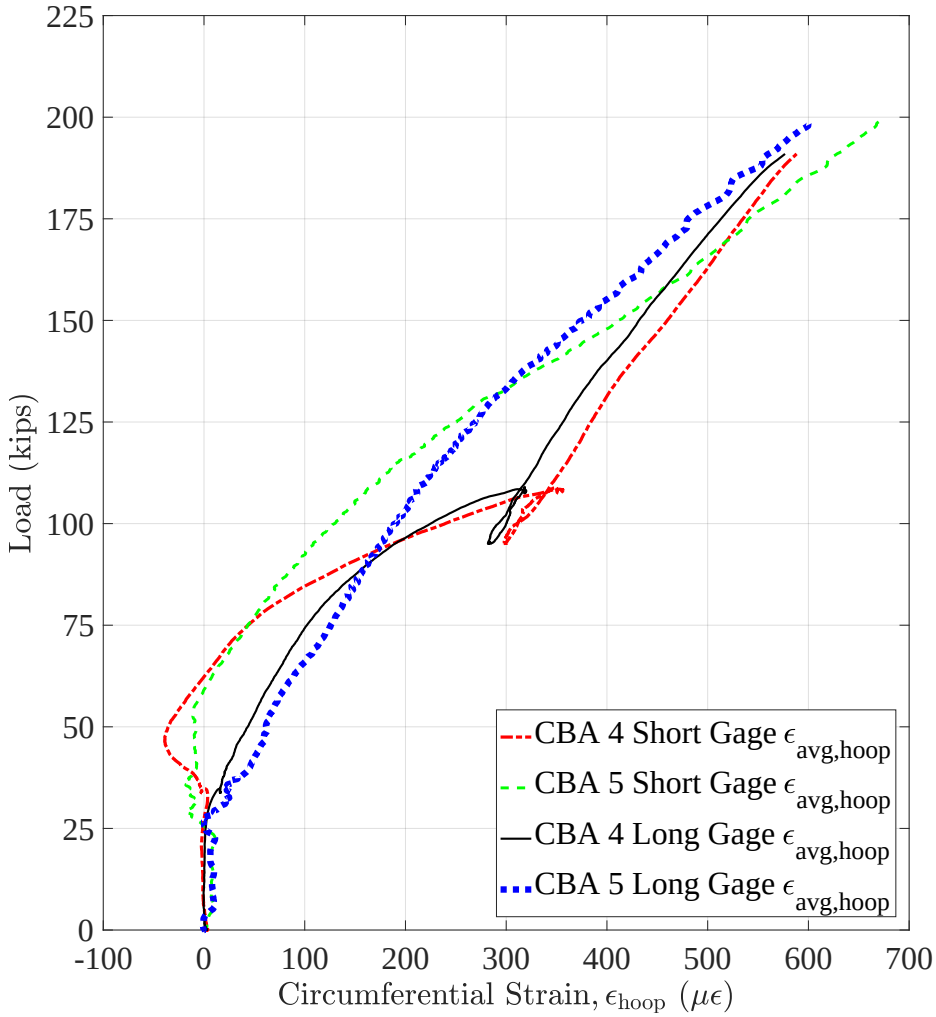

Figure 2.16: Load vs Average Hoop Strain CBA 4 and CBA 5

Specimen CBA 6 (6"x 12") had 11 small circumferential and 11 small vertical strain gages, placed along every inch of the steel tube. Thus, the circumferential and vertical gage readings at 5" from the top surface of the specimen were used in order to compare the results with the rest of the compression tests, since all of the strain gages in all of the other (6"x 6")

specimens were located 4” and 5” from the the top of the specimens.

The load vs. lateral confining stress curves for all specimens are shown in Figure 2.17.

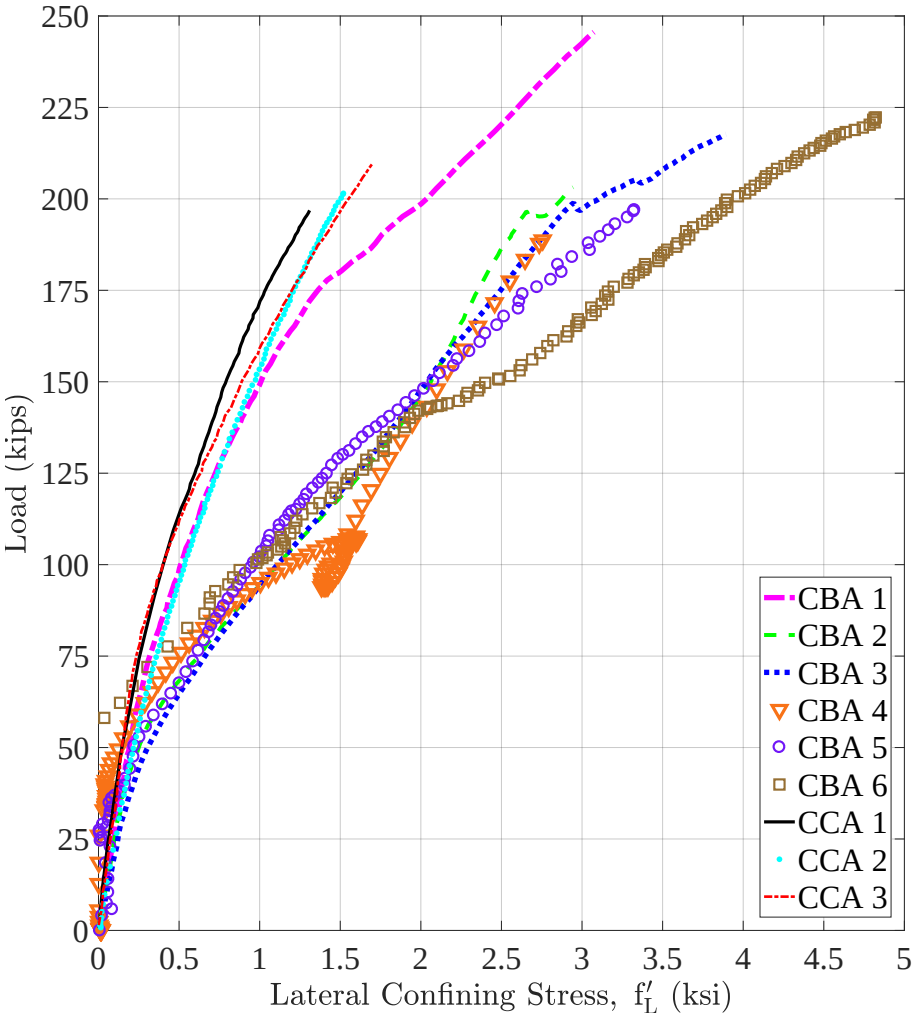

Figure 2.17: Lateral Confining Stress vs Load Compression Tests

This behaviour is consistent with the load vs strain curves, since the lateral confining pressure was derived from the recorded circumferential strain.

The confinement coefficient-load relationships for all compression tests are shown in Figure 2.18.

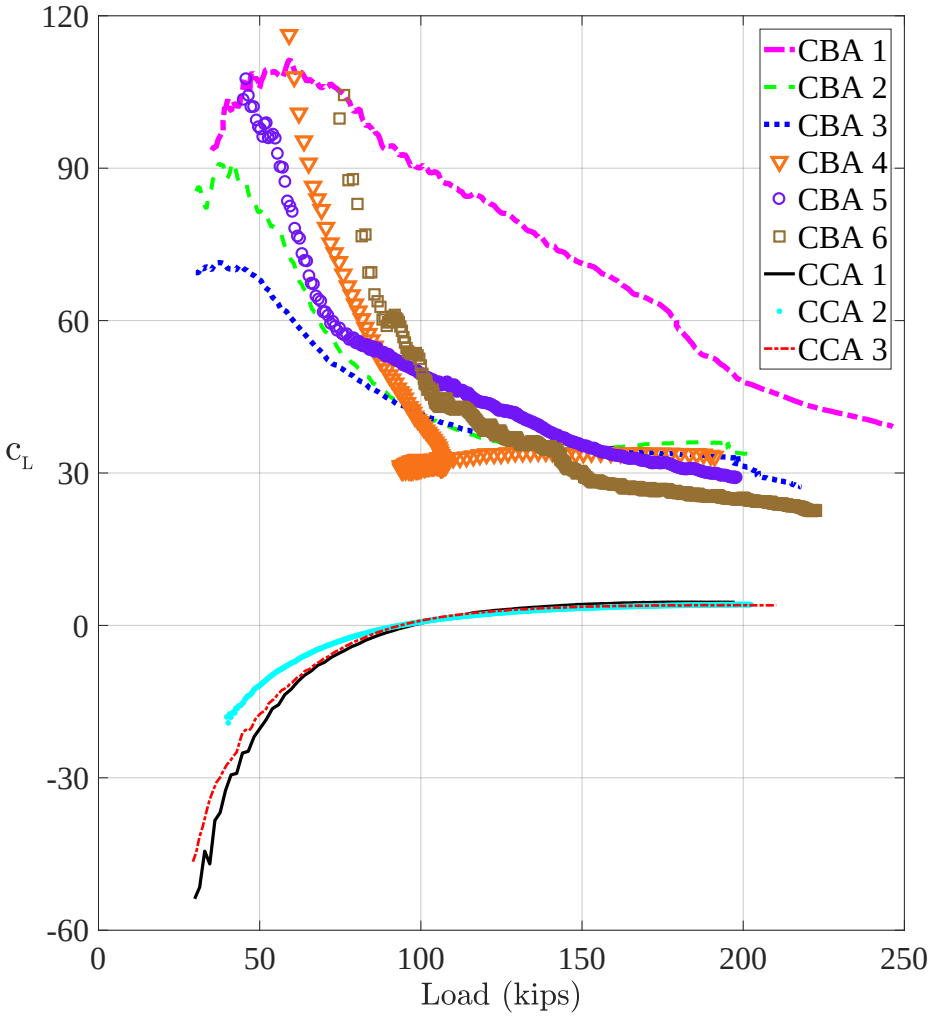

Figure 2.18: Confinement Coefficient vs Load Compression Tests

It can be concluded that the steel tube provides very small resistance at low loads and the higher the load applied, the more confining stress can be obtained. When the confinement ratio is plotted versus the load, it can be seen that for casting anchors, the ratio is converging to 4, while for barrel anchors, it is approaching a maximum of 40 at high loads for Specimens CBA 1,2 and 3 without plastic molds and a maximum of 33 for Specimens CBA 4,5 and 6 which included plastic cylinder molds. Because two features (cylinder height and steel-concrete bond) were different in the two cases, it is not possible to tell which feature affected the results the most.

Negative values of the confinement coefficient were observed at low loads for Specimens

CCA 1,2 and 3. Those occur since the bearing area of the casting anchors is very large - about 17 in^2. Thus, f'_{cc}, which is the ratio of the applied load to the bearing area, is quite small at low loads and much smaller than f'_c. Thus, looking back at Equation 2.11, the value of c_L would be negative. Physically, that simply means that the confinement of the concrete has not quite come into effect, since the applied pressure is too low.

2.5.4 6"x12" Cylinder Analysis

The stress profiles along the specimen height at three different load levels (150, 175 and 200 kips) are shown in Figure 2.19.

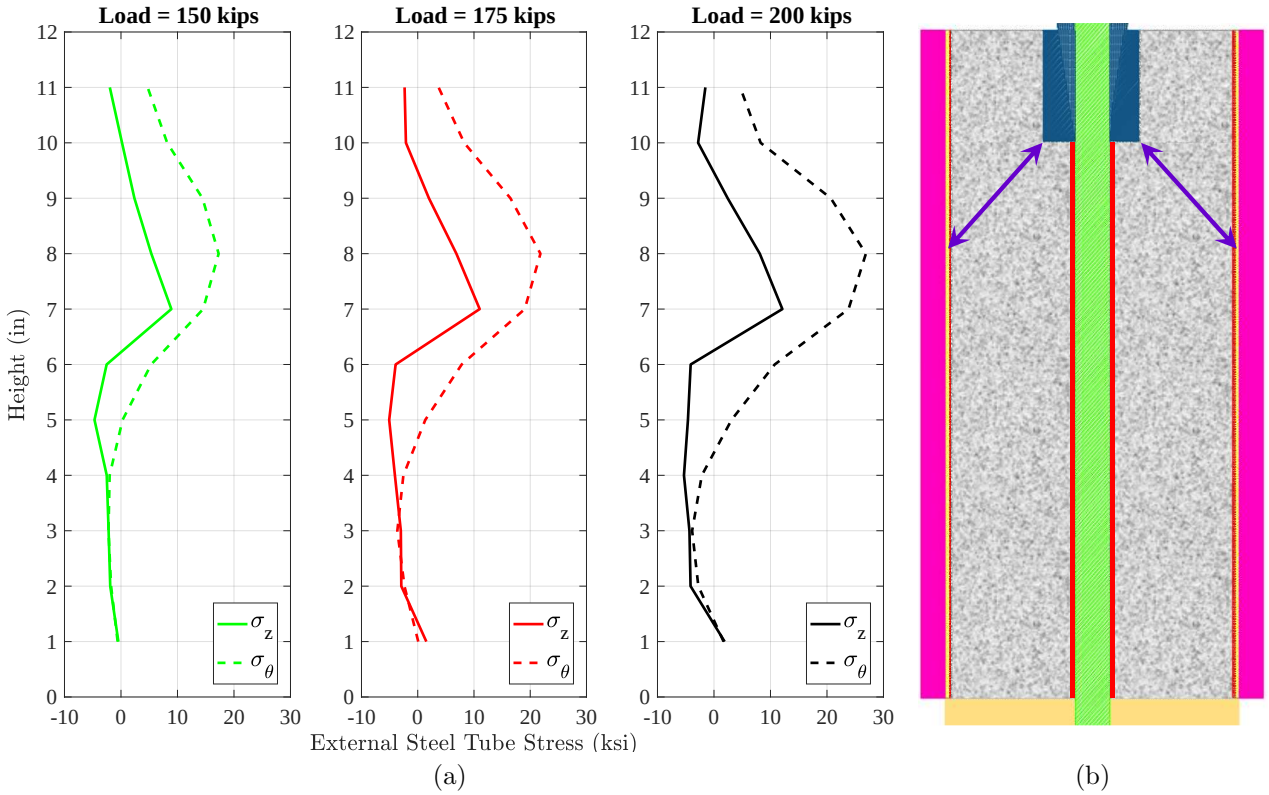

Figure 2.19: Axial and Hoop Stress Profiles Along Height for Specimen CBA 6

Specimen CBA 6 was constructed with a 12" high HSS7x0.5 section and had 11 circumferential and 11 vertical strain gages at every inch along the height of the specimen, in order to determine the distribution of stresses in the concrete more accurately. The axial and cir-

cumferential stress values were determined from the measured vertical and circumferential strains.

Several features are apparent in all three plots.

- **Peak Hoop Stress**. The peak hoop stress occurs at about 8" up from the bottom, or 2" below the loading interface at the bottom of the chuck. This suggests that the load is transferred outwards from its point of application in a conical strut structure with an outer surface that is at 45°to the vertical. That implied load transfer mechanism is in agreement with the expected strut-and-tie model. The hoop stress remains above 50% of that maximum value over a 4" wide band, centered on the location of the peak stress. This suggests a fan mechanism, rather than a pure cone.

- **Non-zero Vertical Stress**. The vertical stress is non-zero over essentially the whole height. This suggests that either the tube wall was bending or that some axial stress was being transferred to the tube wall by friction, despite the greased plastic liner. If the radial pressure from the concrete on the tube was non-uniform with height, which was almost certainly the case, then some wall bending was inevitable. The fact that the peak vertical stress occurred close to the location of peak hoop stress supports this view.

- **Negative Vertical Stress**. The vertical stress is negative near the base. This radial stress there was expected to be nearly uniform with height, and that is confirmed by the nearly-constant hoop stresses, in which there should be little bending. The vertical stress is therefore attributed to axial stress in the tube wall. That vertical stress is in the range of 2-5 ksi from 2"-6" above the base, decreasing gradually towards the bottom, and it drops sharply to a value close to zero right at the bottom. This suggests that some friction existed between the tube wall and the concrete, despite the efforts to eliminate it with the greased plastic sleeve.

In order to investigate further the internal stresses, and particularly the bending, a finite

element numerical model of the system was created using ABAQUS software. The following features were included in the model:

- Only the HSS7x0.5 section was investigated in the model, concrete was not included.
- Generalized Hooke's Law was used to determine the radial strains along the height of the specimen, using the axial and circumferential strain values along the specimen height obtained during testing, as well as to determine axial and hoop stresses.
- Lamé's equations were used to calculate the internal radial stresses and a profile of those along the height of the specimen was created. Since positive vertical strains were observed after about 6" distance from the bottom, the profile which was considered included stress values at 5" from the bottom until 11" from the bottom of the specimen.
- The centroid of each of the profiles shown above was determined, assuming that the load would really be somewhat distributed and would be centered there. The Height vs. Internal Radial Stress curves shown in Figure 2.20 were integrated, resulting in one (for each load) value of load per unit length around the circumference.
- Uniform pressure was assumed to act in compression on the inside wall of the steel cylinder. The distributed load was assumed to act on 1", 2", 2.5", 3", 3.5" and 4" wide strips and the value of the uniform pressure was obtained by dividing the load per unit length by the strip width being analyzed.
- To check the compatibility of the model with the experimental data, the measured strain profiles along the height of the specimen for 125 kips, 150 kips, 175 kips and 200 kips were compared with the profiles obtained from the ABAQUS model. The true width of the applied load band could be obtained by finding the curve in the numerical simulation that the best-fitted the measured strains, and by inspecting the measured and computed ratios of vertical to horizontal stress.

The applied internal pressure (internal radial stress) profiles are shown in Figure 2.20.

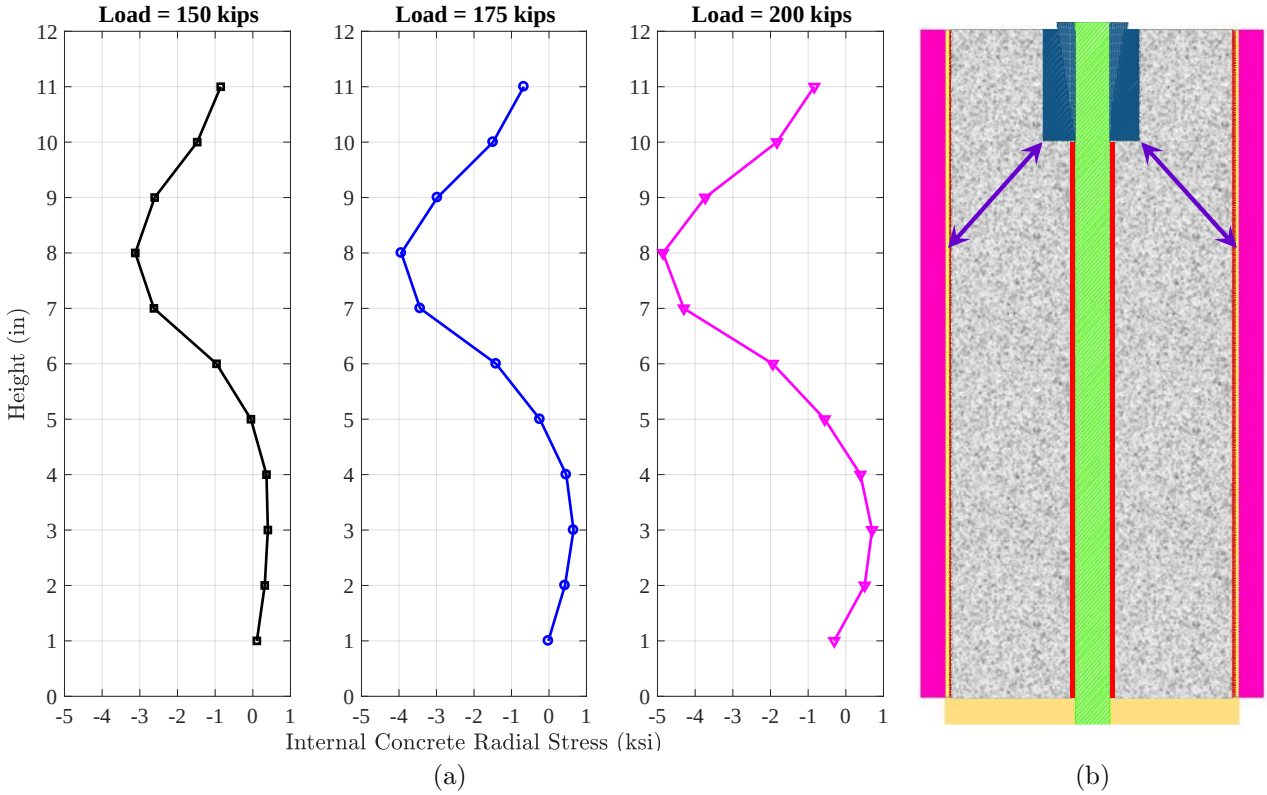

Figure 2.20: Radial Stress Profiles Along Height for Specimen CBA 6

A comparison between the measured and computed strains on the outside of the steel cylinder wall, at different load levels is shown in Figure 2.21. Analyses were conducted for many different widths of the loading band, but only 2", 3" and 4" are shown in the interests of clarity. Both vertical and hoop strains are shown.

The overall shapes of the computed profiles match those of the measured profiles, but the hoop strains appear to fit better than the vertical strains. No vertical load on the steel was included in the numerical model, but friction might have introduced some in the test, which may explain why the computed vertical strains are more positive (tensile) than their measured counterparts, especially in the peak stress region.

The strain errors were squared, added and normalized with respect to load, for each load width. The results are plotted against load width in Figure 2.22a, which shows vertical ("V") and circumferential ("C"), or hoop, values separately. Results for the vertical and hoop errors combined are shown in Figure 2.22b.

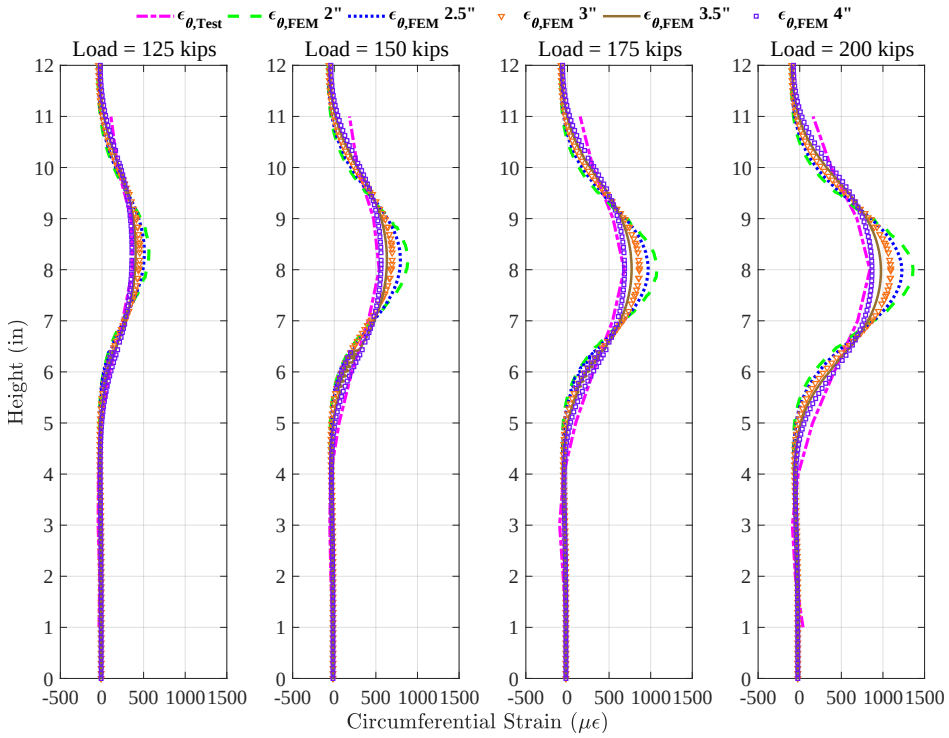

(a) External Steel Tube Circumferential Strain Profile

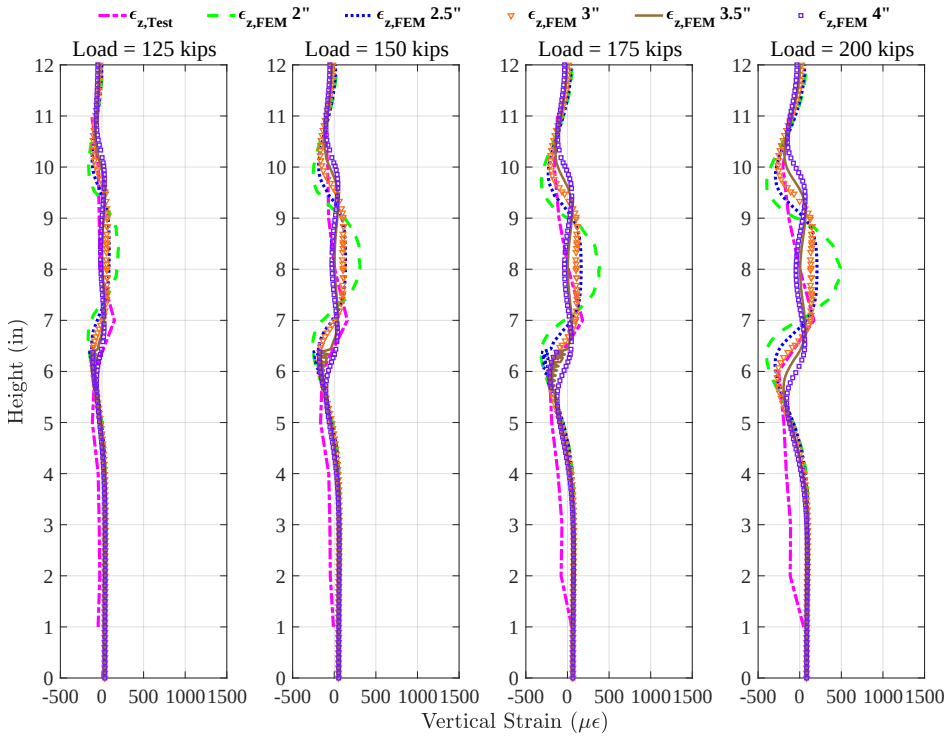

(b) External Steel Tube Vertical Strain Profile

Figure 2.21: Experimental Strain Profiles vs ABAQUS Strain Profiles

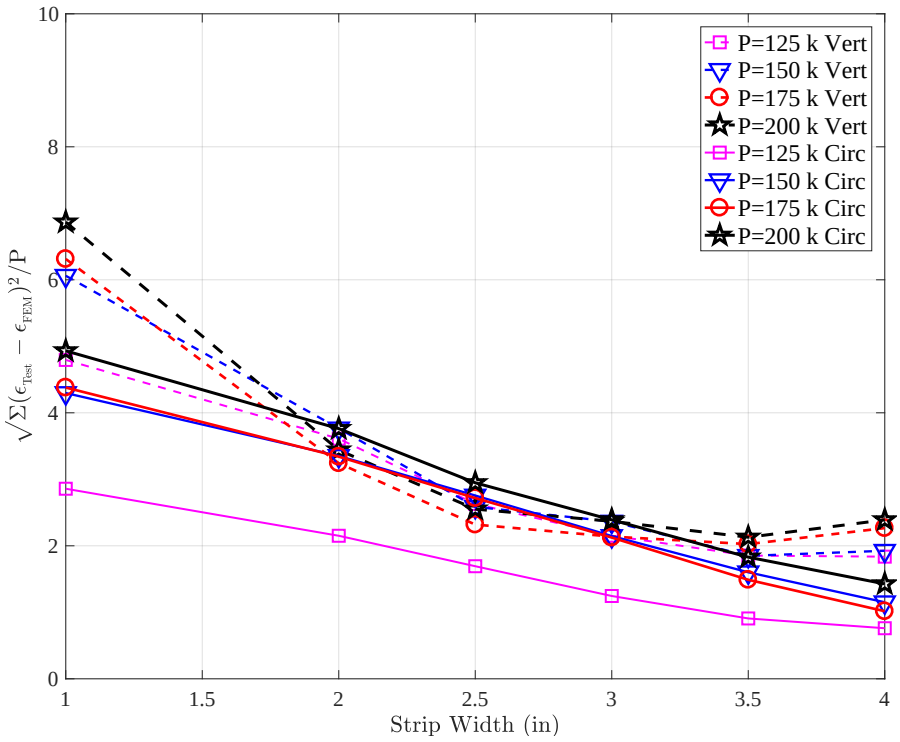

(a) Individual Strain Difference Error

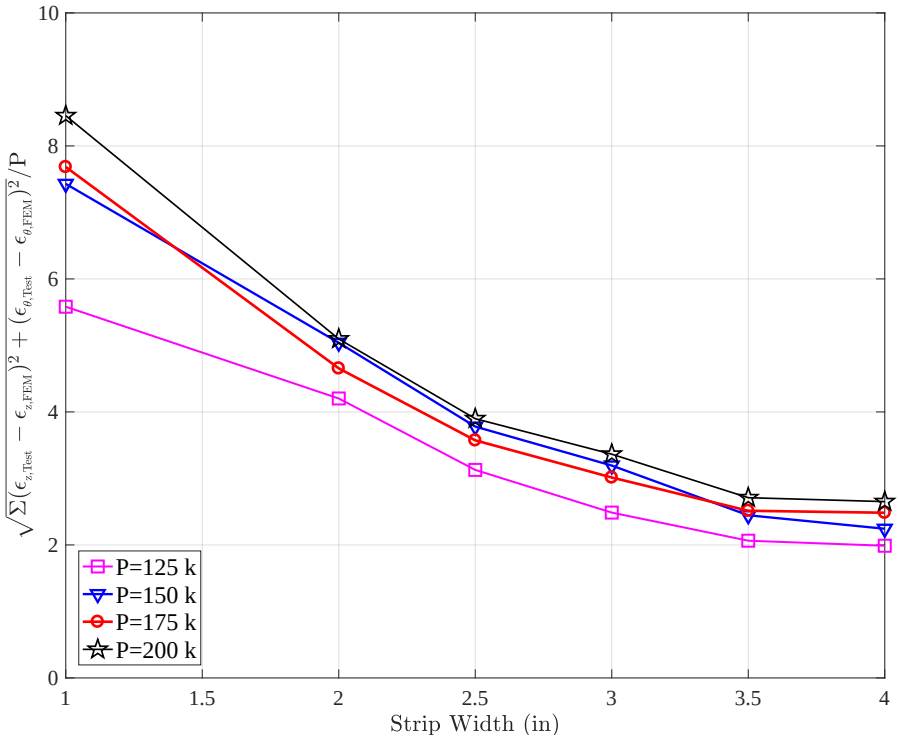

(b) Cumulative Strain Difference Error

Figure 2.22: Strain Difference Error vs Strip Width

It can be deduced that the best fit is obtained with a load width between 3" and 4". The hoop strains showed smaller errors than the vertical ones, as might be expected from the profiles in Figure 2.21, and the fits were generally better at lower loads (i.e. 150 rather than 200 kips).

Other loading patterns, such as a triangular, a parabolic and a sinusoidal distribution were considered; however, since the strain profile along the height of the specimen for the uniformly distributed load pattern was always closest to the experimental profile, it was concluded that the use of uniform load distribution would be sufficient.

Figure 2.23 shows the best fit model based on the numerical analysis results.

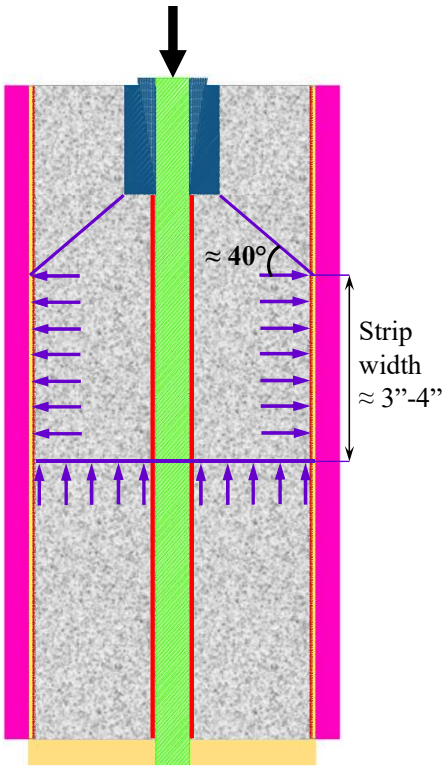

Figure 2.23: Internal Pressure Distribution Based on Analysis Results

2.6 Conclusions

The use of a strand anchor with a small bearing area, namely a barrel anchor without a bearing plate, was deemed sufficient for the development of the girder- diaphragm connection

as a result of the tests described in this chapter. It was shown that the barrel anchor detail would have satisfactory capacity in terms of strength, while experiencing little slippage and local concrete crushing. When tested in tension, the barrel anchors had not sustained any damage by the time the strand had reached its fracture load. Upon testing the barrel anchors in compression, it was discovered the concrete directly behind the bearing anchor could resist bearing stresses as high as 100 ksi with very little local crushing and little slip of the anchor.

Casting anchors' behaviour under compression was satisfactory, however their use would be practically challenging due to constructability issues and extra weight, which can be a problem during girder transportation. They are also larger compared to the current detail, which includes a 4"x 4" rectangular backing plate welded to a barrel anchor. They were investigated as they are more convenient, since no extra welding is required. Barrel anchors would be used in the next stages of the project, while investigating the behaviour of anchored strands, extended from the girder into the diaphragm, because they represented the simplest and most constructable solution and provided anchorage strength that was much higher than required.

Chapter 3

BREAKOUT TESTS

3.1 Introduction

This chapter discusses the tension tests carried out on strands, anchored with post-tensioning chucks and embedded in concrete blocks, in order to observe the impact of the possible failure mechanisms of the aforementioned on the development of the girder-cap beam positive moment connection.

There are four main failure modes for headed studs, subjected to tensile load. These possible failure modes are depicted in Figure 3.1. One possibility of failure is due to the *yielding* and possibly *fracture* of the anchoring system before the breakout of concrete takes place, which is a ductile mode of failure and is desirable. Failure can occur due to *pullout* - which is the sliding of the anchor (either partially or completely) from the concrete, and should be prevented at all cost. Another alternative is a *pullthrough* failure, which involves the pullout of the anchor (or a part of it), with the generation of a localized and relatively small breakout cone in close proximity to the anchor. This failure mode is likely to take place for anchors that have undergone excessive deformations and is mainly dependent on the quality of the anchoring device, thus it is viewed as acceptable. Lastly, highly undesirable brittle modes of failure could occur due to either substantial *breakout* or *splitting* of the concrete member before the yielding of the anchoring device. Splitting failure would be highly dependent on the spacing between anchors, as well as the edge distance of the anchors and the member thickness (Fuchs et al., 1995).

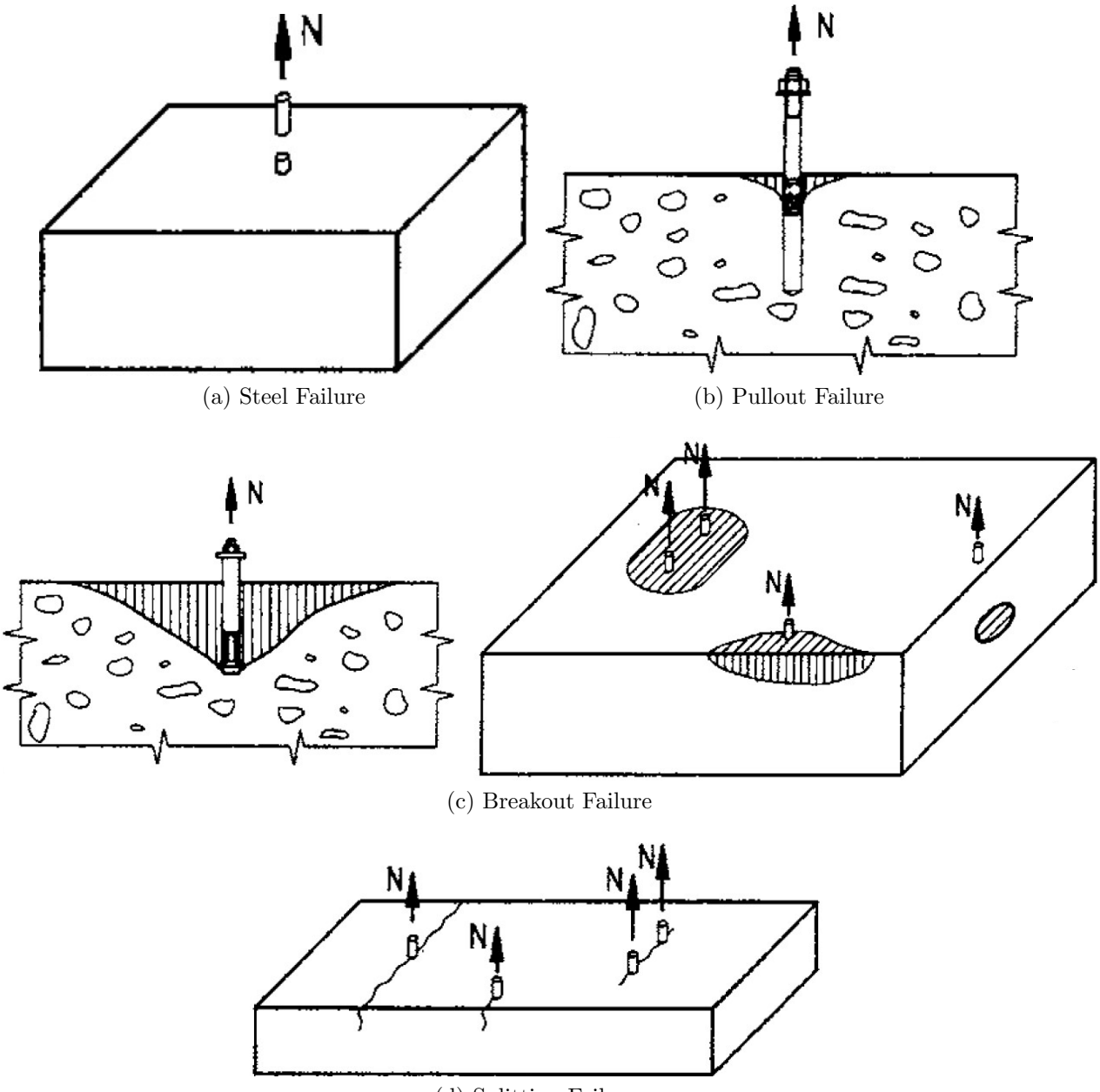

(a) Steel Failure

(b) Pullout Failure

(c) Breakout Failure

(d) Splitting Failure

Figure 3.1: Failure Types of Anchors Under Tensile Load (Fuchs et al., 1995)

For strands anchored in a cap beam, the undesirable failure modes are breakout, pullout and splitting. Splitting is ignored here because the cap beam is so massive and is anyway subjected to torsion, rather than bending, by the girders. Pullout is not possible because of the strand anchors, as shown in Chapter 2. Thus, breakout is the only remaining candidate

behaviour.

Different block depths and strand patterns were considered, by taking into account the strands extended from the girders into the cap beam and the possible breakout cones that could occur.

The goal of these tests is to determine the embedment depth of the anchored strands at which the failure mode shifts from brittle to ductile, and thus prevents the breakout of concrete from being the controlling mechanism. To that end, an expression, providing the strength of the system as a function of depth, was sought.

3.2 Mechanics of Breakout and Methods of Prediction

As previously mentioned, the specimens were designed in accordance with the procedures specified in ACI and PCI. Both design methodologies are based on the Concrete Capacity Design (CCD) Method, developed by Eligehausen (Fuchs et al., 1995).

3.2.1 Concrete Capacity Design Approach

The Concrete Capacity Design (CCD) method proposes the following methodology for determining the concrete capacity of steel fastenings under tension load (Fuchs et al., 1995).

For fastenings subjected to tensile load, a conical failure surface inclined at about 35° with respect to the concrete member is assumed. This implies that the failure surface would spread horizontally roughly three times the effective embedment depth.

The following equation is proposed by the CCD Method for the cone failure load of a single anchor, embedded in uncracked concrete and unaffected by edge effects or overlapping cones.

$$N_{no} = k_{nc}\sqrt{f'_c}\; h_{ef}^{1.5} \tag{3.1}$$

where

h_{ef} is the effective embedment depth of the anchor (in),

f'_c is the specified concrete compressive strength (psi),

$k_{nc} = k_1\ k_2\ k_3$ and k_1, k_2 and k_3 are calibration factors.

The Concrete Capacity Design method proposes $k_{nc} = 40$ for cast-in-place anchors. As the tests described here involve cast-in-place anchors, this value was used when comparing failure loads obtained from the experiments and predicted failure loads.

Since the CCD method is based on rectangular prisms, variations in edge distances, spacing between anchors, as well as different configurations of anchors (group effect) can be easily incorporated.

For multiple anchors, the capacity of concrete can be determined by using the following equation.

$$N_n = \frac{A_N}{A_{No}}\ \Psi_2\ k_{nc}\ \sqrt{f'_c}\ h_{ef}^{1.5} \tag{3.2}$$

where

$A_{No} = 9\ h_{ef}^2$ and is defined as the projected area of one anchor at the concrete surface unlimited by edge influences or neighboring anchors (in^2), idealizing the failure cone as a pyramid with a base length of $3h_{ef}$,

A_N is defined as the actual projected area at the concrete surface (in^2), assuming the failure surface of the individual anchors as a pyramid with a *base length* $= 3h_{ef}$, and the CCD projected areas are illustrated in Figure 3.2.

$$\Psi_2 = \begin{cases} 1 & \text{for edge distances} \geq 1.5h_{ef} \\ 0.7 + 0.3\dfrac{\text{min edge distance}}{1.5h_{ef}} & \text{for edge distances} \leq 1.5h_{ef} \end{cases}$$

For the tests described in this chapter, the effective embedment depth h_{ef} was measured from the top of the barrel anchor.

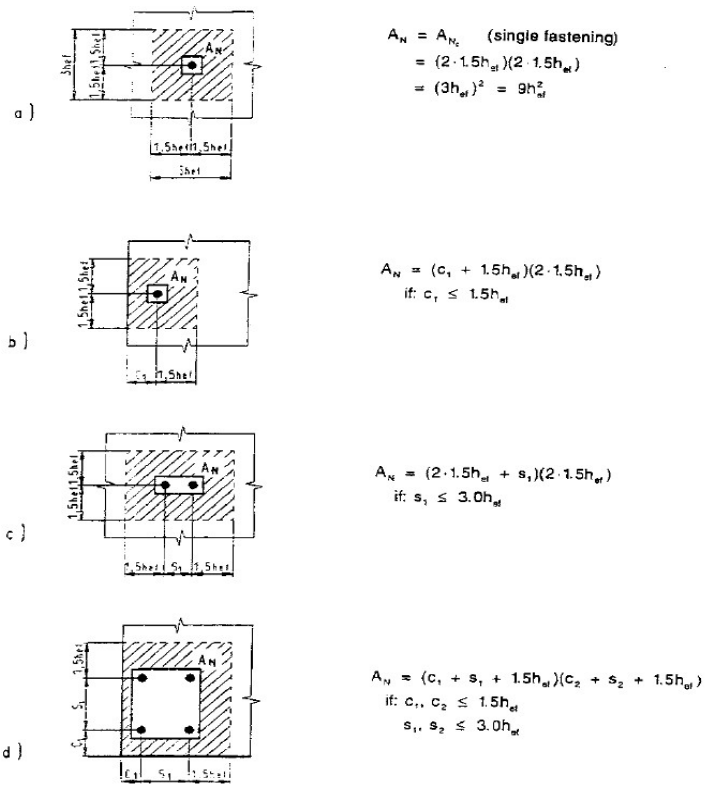

Figure 3.2: Projected Areas for Different Anchors Subjected to Tensile Load (Fuchs et al., 1995)

3.2.2 ACI Design Approach

The test specimens were designed according to the procedure, described in Appendix D in the ACI 318-11 Code.

As in the CCD model (Fuchs et al., 1995), the breakout strength of concrete is determined by assuming a concrete failure prism with approximately 35° angle. Similarly, the failure surface projects $1.5h_{ef}$ horizontally from the center of the anchors.

The breakout strength of a single anchor, as well as a group of anchors embedded in concrete, assuming cracked conditions, are determined by the following equations, respectively, and are illustrated in Figure 3.3.

For a single anchor,

$$N_{cb} = \frac{A_{N_c}}{A_{N_{co}}} \Psi_{ed,N} \Psi_{c,N} \Psi_{cp,N} N_b \qquad 3.3$$

For a group of anchors,

$$N_{cbg} = \frac{A_{N_c}}{A_{N_{co}}} \Psi_{ec,N} \Psi_{ed,N} \Psi_{c,N} \Psi_{cp,N} N_b \quad 3.4$$

where

A_{N_c} is the projected concrete failure area of a single anchor or group of anchors that shall be approximated as the base of the rectilinear geometrical figure that results from projecting the failure surface outward $1.5h_{ef}$ from the center lines of the anchor, or in the case of a group of anchors, from a line through a row of adjacent anchors (in^2);

$A_{N_c} \leq nA_{N_{co}}$, and n is the number of anchors in the group, resisting tension,

$A_{N_{co}} = 9h_{ef}^2$ and is defined as the projected concrete failure area of a single anchor with an *edge distance* $\geq 1.5h_{ef}$ (in^2),

$\Psi_{ec,N} = \dfrac{1}{1 + \dfrac{2e'_N}{3h_{ef}}} \leq 1.0$ is a modification factor for groups of anchors loaded eccentrically in tension and

e'_N is the eccentricity of the tensile force relative to the center of the anchor group (in). In the tests described here, the load was applied concentrically, thus $\Psi_{ec,N} = 1.0$,

$\Psi_{ed,N} = 1.0$ for *minimum edge distance* $\geq 1.5h_{ef}$ and is defined as a modification factor for edge effects for single anchors or anchor groups loaded in tension. In tests, described here, every specimen had *edge distance* $> 1.5h_{ef}$. $\Psi_{ed,N}$ is Ψ_2 in the CCD method notation.

$\Psi_{c,N} = 1.25$ for cast-in-place anchors and is defined as the modification factor for anchors located in a region of a concrete member where analysis indicates no cracking at service load levels,

$\Psi_{cp,N} = 1.0$ for cast-in-place anchors and is defined as the modification factor for post-installed anchors designed for uncracked concrete,

$N_b = k_c \lambda_a \sqrt{f'_c} h_{ef}^{1.5}$

where

$k_c = 24$ for cast-in-place anchors and its values were determined from a large database of test

results in uncracked concrete at the 5 percent fractile and were adjusted to cracked concrete, $\lambda_a = 1.0$ for normal weight concrete.

For embedment depths greather than 11", the expression for N_b including the $h_{ef}^{1.5}$ term was determined to be too conservative and an alternative was proposed as follows.

For 11" $\leq h_{ef} \leq$ 25"

$$N_b = 16\ \lambda_a\ \sqrt{f'_c}\ h_{ef}^{5/3}$$

where

h_{ef} is the effective embedment depth (in), in this case measured from the top of the barrel anchor.

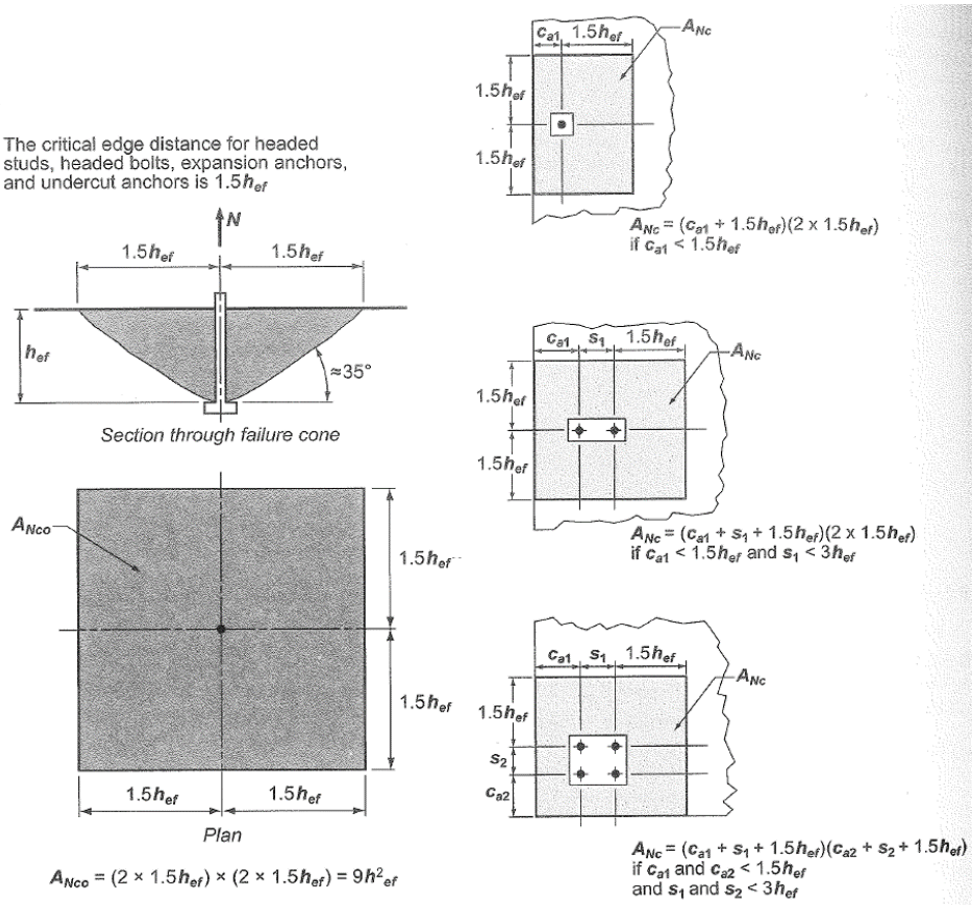

Figure 3.3: Projected Areas for Different Anchors Subjected to Tensile Load (ACI318, 2011)

The test specimens were designed based on designating a target capacity and determining the required embedment depth to achieve failure at the target load, according to the ACI procedure, described above.

3.2.3 PCI Design Approach

The design method, described in PCI Design Handbook Chapter 6 was used as an alternative while designing the test specimens, in order to make a comparison with the failure loads predicted by ACI.

The breakout concrete strength for studs loaded in tension can be determined as shown in Equation 3.5.

where

$$N_{cb} = C_{bs}\ A_N\ C_{crb}\ \Psi_{ed,N} \tag{3.5}$$

$C_{bs} = 3.33\ \lambda \sqrt{\frac{f'_c}{h_{ef}}}$ and is defined as the breakout strength coefficient,

A_N is the projected surface area for a stud or group of studs (in^2), and is depicted in Figure 3.4.

$\Psi_{ed,N}$ is a modification factor based on the edge distances of the embedded anchor. It is the same as ACI notation. $\Psi_{ed,N} = 1.0$ since the minimum edge distances were greater than $1.5h_{ef}$.

h_{ef} is the effective embedment depth (in), in this case measured from the top of the barrel anchor to the surface of the concrete block.

C_{crb} is defined as the cracking factor and $C_{crb} = 1$, assuming uncracked concrete, which was the case here.

λ is a modification factor reflecting the reduced mechanical properties of lightweight concrete, and $\lambda = 1.0$ for the tests described.

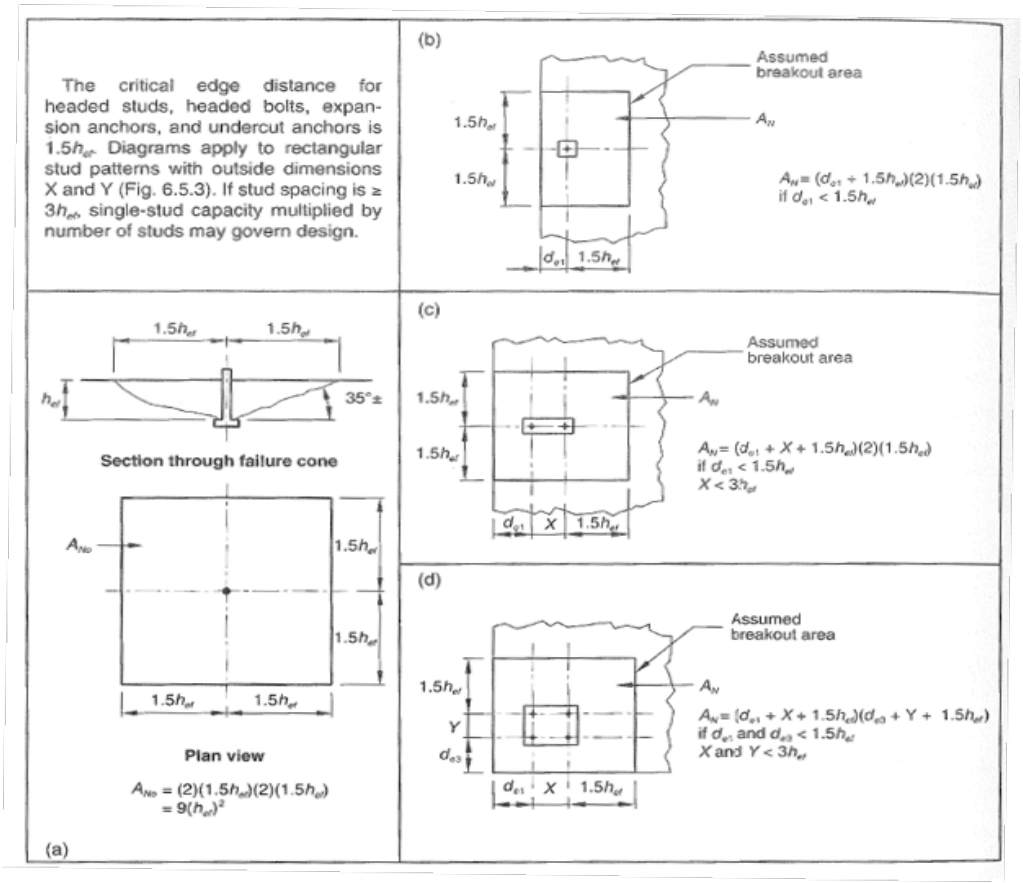

Figure 3.4: Projected Areas for Different Anchors Subjected to Tensile Load (PCI, 2004)

This method is more conservative than the ACI method, as for anchors, embedded deeper than 11”., ACI proposes an adjusted equation, suggesting that the $h_{eff}^{1.5}$ term in the equation, used to determine the breakout capacity is too conservative, including the use of $h_{eff}^{5/3}$, as described in Section 3.2.2.

3.3 Test Specimens

3.3.1 Specimen Configuration

Fourteen specimens with varying depths and strand configurations were designed in order to observe the effect of embedment depth and collective impact of different groups of strands on the breakout failure mechanism. Considering the girder strands extended into the diaphragm, the failure mechanisms for four different strand patterns were investigated- single strand, two

strands, four strands in a line and four strands in a square.

The designed specimens, as well as the details of the considered strand patterns considered are shown in Figure 3.5.

Pattern	Specimen
	U_1_O_1.75
	U_1_O_3.63
	U_1_O_5.19
	U_1_O_6.06
	B_1_O_1.75
	B_1_O_3.50
	B_1_O_5.00
	B_1_O_6.50
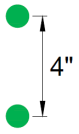	U_2_L_2.75
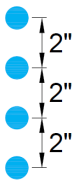	U_4_L_5.50
	U_4_L_9.25
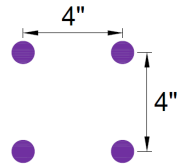	U_4_S_9.75
	U_4_S_14.50
	U_4_S_16.50

(a)

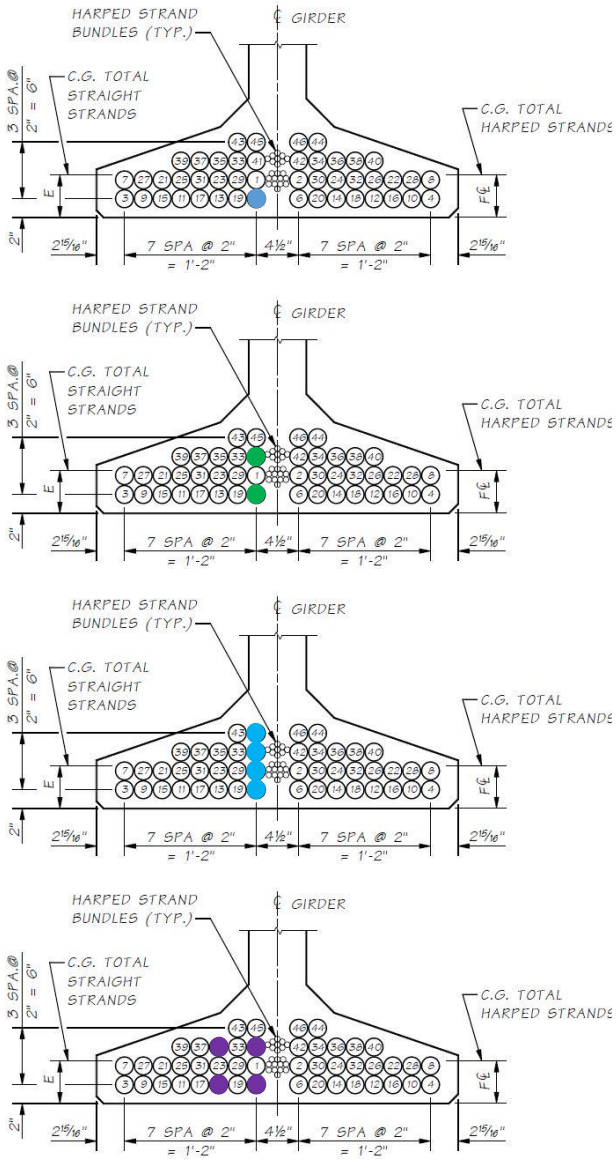

(b)

Figure 3.5: Breakout Specimen Configuration

The naming system for the specimens is explained as follows.

The first letter of the specimen name - either B or U - stands for the bond conditions of

the strands in the specimen, indicating whether the strand is *bonded* or *unbonded*.

The subsequent number - either 1, 2 or 4 - stands for the number of strands present in the specimen.

The following letter - O, L or S - represents the pattern of the strands in the specimen, and corresponds to *one*, *line* and *square* strand patterns respectively.

The final number represents the effective embedment depth of the strand anchors, in inches, given by the distance from the top of the barrel anchor to the concrete surface.

Thus, for instance, U_4_L_9.25 would describe an unbonded specimen with 4 strands in a line, with 9.25" effective embedment depth.

The effect of bonded strands was investigated only for specimens with a single strand. It was theorized that the bonded specimens would fail at lower loads, presuming the failure would occur in stages, generating from top of the specimen, creating cone-like breakout surfaces developing in stages, depending primarily on the bond between the strand and the concrete. However, all strands were covered with electrical tape for approximately 1"-1.5" from the top of the strand chuck and the single strand specimens were quite shallow overall - varying between 1.75" and 6.5". The electrical tape was used in order to prevent concrete from getting between the strand and the barrel anchor. Thus, it is likely that the smallest bonded specimens were not fully bonded and it is uncertain whether the "true" bonded behaviour can be captured by investigating such small depths. Test results show that the maximum loads for bonded and unbonded specimens are quite close, and further investigation of the bond conditions on the failure load was not carried out.

3.3.2 Specimen Design

The strand orientations investigated in the tests were selected considering that certain groups among the extended strands were in danger of suffering a breakout failure, unless they were embedded into the diaphragm for a sufficient length. To that end, the strands were embedded in concrete blocks with varying depths, in order to determine how much embedment is needed to provide ductile failure mode, while investigating how closely the CCD, ACI and PCI

methods agree with the test breakout load values at failure. The majority of the strands were debonded by using a plastic PVC pipe.

The loads induced in each specimen are shown in Figure 3.6.

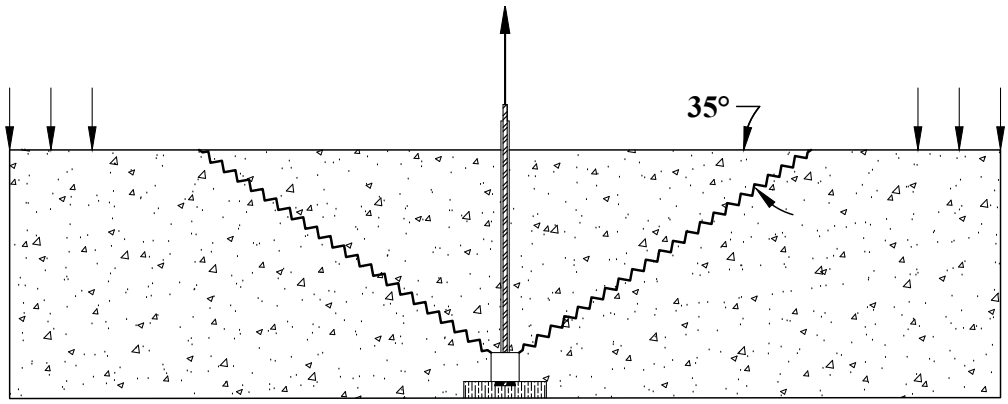

Figure 3.6: Breakout Specimen Loads

Tensile load was applied concentrically to the strands embedded in concrete, while the distributed load, acting in compression, represents the effect of the support posts, used in the tests, pushing down on the ends of the concrete blocks. The support posts were placed such that they would not interfere with the occurrence of the predicted 35° breakout cone. As it can be seen in Figure 3.6, the testing system that was used here, generated bending moments on the concrete blocks; the specimens were not under the effect of pure tension. Thus, flexural and shear effects would also be present in addition to the failure mechanisms mentioned above. To that end, all of the specimens were reinforced with flexural steel on top, considering that they would be tested along the blocks' diagonal top surface, such that they could resist the largest negative bending moments that would arise during the tests. It was aimed to prevent excessive flexural cracking, thus avoiding failure of the specimens in an undesired mode-flexure. Using flexural reinforcement would also partially replicate the heavily reinforced diaphragm, and confine the concrete to some extent, when compared to the concrete in the diaphragm, thus it was deemed to provide more realistic conditions. Shear reinforcement was not placed in order to avoid its potential prevention of the expected breakout cones.

3.4 Test Setup

The test setup is shown in Figure 3.7.

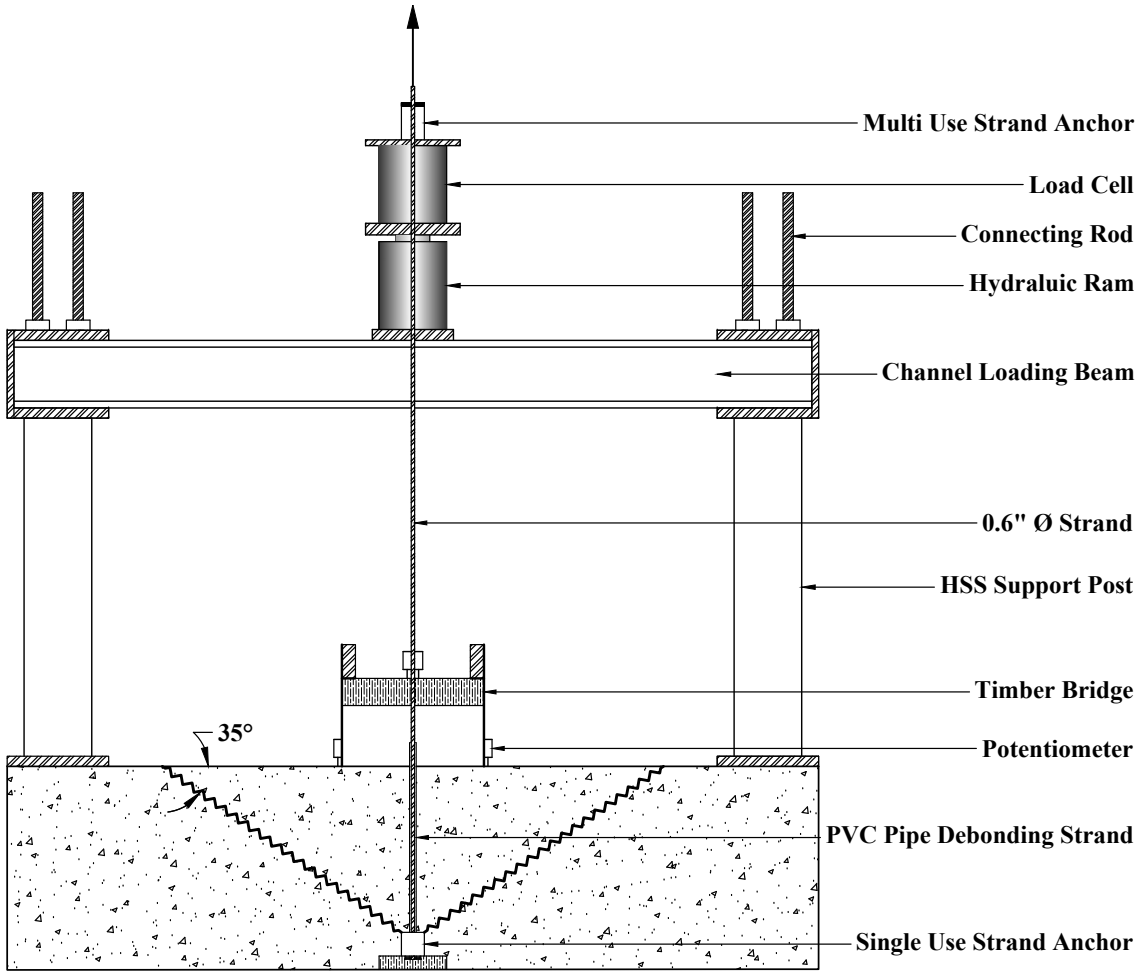

Figure 3.7: Breakout Test Setup

A testing assembly composed of a loading beam, namely, 2 MC channels with two pieces of 3.5" wide flat bar between them welded back to back , sitting on two square HSS 5x5x3/8 support posts, was used.

The tension tests were conducted by using a hydraulic ram; the applied load was recorded both by a pressure sensor connected to the ram, as well as by a load cell. Multi-use strand chucks were used above the hydraulic ram to grip the strands while conducting the tension tests.

Four potentiometers were used to determine the displacements of the concrete surface and the strands in the duration of the tests.

For specimens with a single strand, two potentiometers were placed on the strand, and two were used to measure the heaving of the concrete surface relative to a timber bridge attached to the the outer edge of the block as shown in Figure 3.7.

For specimens with multiple strands, one potentiometer was used for each strand and two were used to measure the concrete surface displacement.

Since the sizes of the blocks varied significantly, different setups were used for smaller and larger specimens.

3.4.1 Small Specimens

The testing assembly for small specimens is shown in Figure 3.8.

Figure 3.8: Small Specimens Test Assembly

For smaller specimens, namely, ones with shallow depths and (mostly) a single strand, the use of 2 MC 6x15.1 channels was determined to be sufficient. The loading beam, composed of the channels, resting on rectangular HSS posts was placed along the diagonal of each

concrete block in order to maximize the post spacing and minimize the possibility of the posts' interfering with the breakout failure.

The channels were designed so that the spacing of the HSS posts could be adjusted to any desired distance, and the MC 6x15.1 were chosen to satisfy bending and shear requirements for a load of 60 kips at the widest spacing. A hydraulic ram with 60 kips load capacity, as well as a load cell with 50 kips capacity were used in the tests.

As can be seen in Figure 3.8, plywood shims were placed under the HSS sections, in order to prevent local crushing failure of a high spot of the concrete. Furthermore, the distance between the HSS sections was arranged such that the latter do not restrict the predicted breakout cone, overlapping with its diameter. The procedures for design of the breakout cone diameter are explained in detail in Section 3.2.

3.4.2 Large Specimens

The testing assembly for large specimens is shown in Figure 3.9.

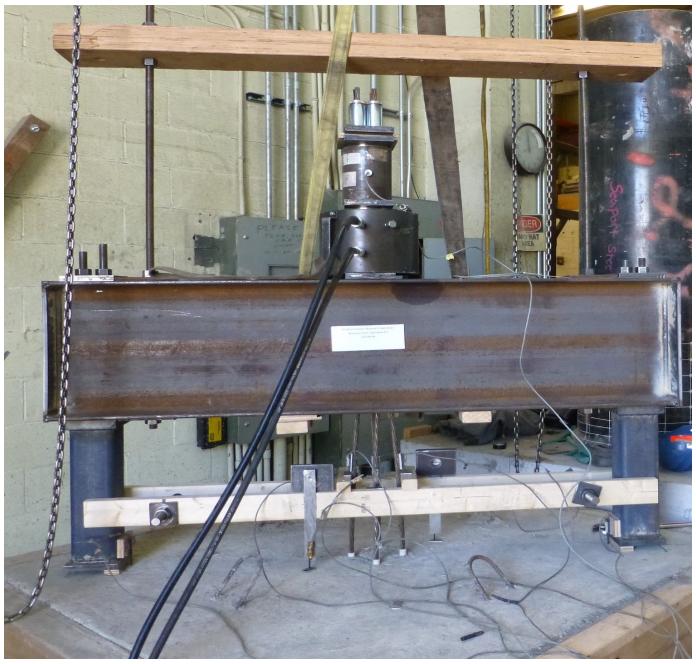

Figure 3.9: Large Specimens Test Assembly

For the larger specimens, 2 MC 18x58 were used, because the larger spans and expected

breakout forces of the four-strand specimens led to much larger moments.

A hydraulic ram and load cell with 300 kips capacity were used in the tests.

Plywood shims were placed under the HSS sections to prevent local crushing failure, analogous to the small specimens assembly. Similarly, the distance between the HSS sections was selected such that the predicted breakout cone would not be obstructed.

A piece of plywood was placed between the steel plates, located above the load cell and below the multi-use strand chucks, in order to ensure that the wedges in the mutli-use chucks were set the same amount, which would lead to all of the strands being stressed simultaneously and the applied load being distributed identically among them.

3.5 Test Results

The loads at failure and the failure modes, as well as the concrete strengths of the blocks at the time of testing are shown in Table 3.1.

Table 3.1: Breakout Tests Results

Specimen	f'_c (psi)	P_{fail} (k)	Failure Mehcanism	System Behaviour
U_1_O_1.75	4250	9.12	Concrete Breakout	Brittle
U_1_O_3.63		18.34		
U_1_O_5.19		31.53		
U_1_O_6.06		38.48		
B_1_O_1.75		6.42		
B_1_O_3.50		18.07		
B_1_O_5.00		33.63		
B_1_O_6.50		47.09		
U_2_L_2.75	4300	18.27		
U_4_L_5.50	4605	48.28	Severe Flexural and Shear Cracking	
U_4_L_9.25		104.36		
U_4_S_9.75	4200	109.06		
U_4_S_14.50		176.23		
U_4_S_18.50	4200	231.07	Strand Fracture	Ductile

For shallow specimens, namely, specimens with a single strand and two strands, a breakout failure mechanism similar to what was expected was achieved.

Figures 3.10 to 3.18 show the crack patterns for specimens with a single strand and two strands.

(a) Top View

(b) North View

(c) South View

(d) West View

Figure 3.10: Specimen U_1_O_1.75 Crack Patterns

(a) Top View

(b) East View

(c) North View

Figure 3.11: Specimen B_1_O_1.75 Crack Patterns

(a) Top View

(b) South View

(c) East View

(d) North View

Figure 3.12: Specimen U_1_O_3.63 Crack Patterns

(a) Top View

(b) East View

(c) South View

Figure 3.13: Specimen B_1_O_3.5 Crack Patterns

(a) Top View

(b) South View

(c) East View

(d) North View

Figure 3.14: Specimen U_1_O_5.19 Crack Patterns

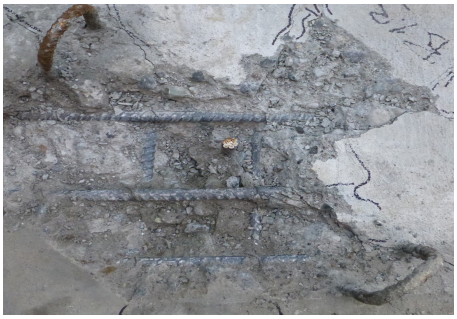

(a) Top View

(b) West View

(c) South View

Figure 3.15: Specimen B_1_O_5.00 Crack Patterns

(a) Top View

(b) North View

(c) West View

(d) South View

Figure 3.16: Specimen U_1_O_6.06 Crack Patterns

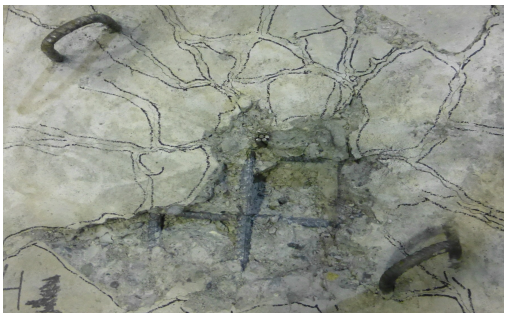

(a) Top View

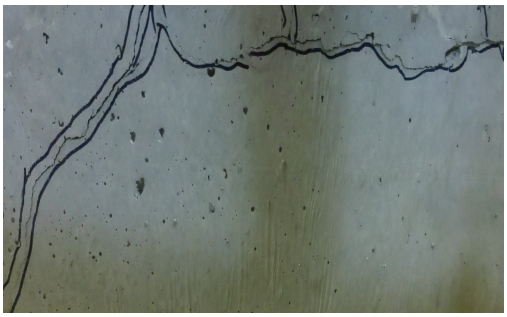

(b) South View

(c) West View

(d) East View

Figure 3.17: Specimen B_1_4_6.50 Crack Patterns

(a) Top View

(b) West View

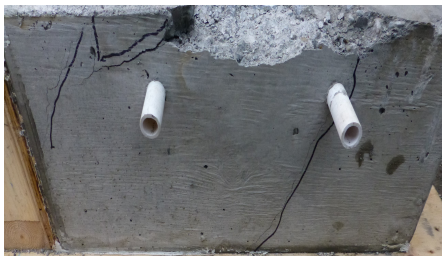

(c) North View

Figure 3.18: Specimen U_2_L_2.75 Crack Patterns

All specimens were designed such that the anchored strands would breakout of the concrete, creating a conical failure surface at a 35° angle from the top of the concrete block. For the specimens with one or two strands, a breakout failure was observed. However, it was never a pure breakout failure, as one can see from the photos, since in all cases the radial cracks, propagating from the strand along the top of the concrete surface, are often accompanied by some flexural cracks, which in some cases propagate to the bottom of the specimens. Furthermore, in most cases, particularly as depicted in Figures 3.12, 3.16 and 3.18, the compression load generated by the support posts caused the sides of the blocks to crack severely, splitting from the blocks. However, since the specimen dimensions were chosen such that they would satisfy the required area of expected breakout cones and the posts were placed on block edges in order to avoid any interference with the breakout cones, this was thought to have had minimal effects. With this in mind, looking at the failure cones, the projected breakout area observed on the top of the blocks matches the predicted area of $3h_{ef}$x$3h_{ef}$ quite closely. Thus, overall, a failure mode similar to the expected one was achieved.

The crack patterns for specimens with four strands are shown in Figures 3.19 to 3.23.

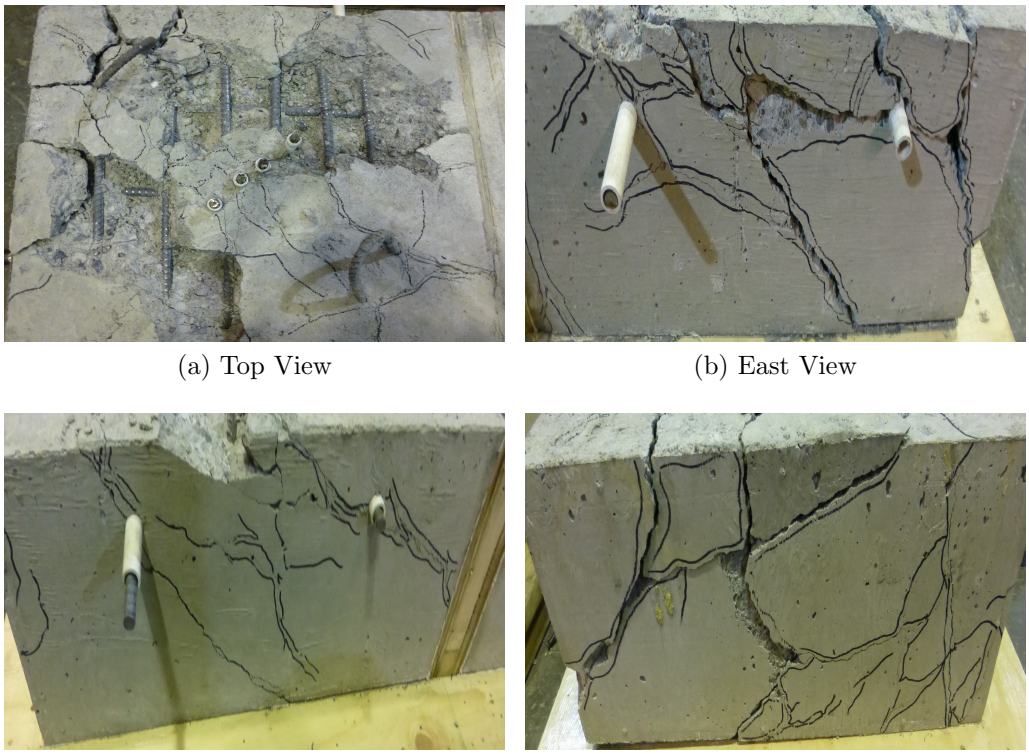

(a) Top View (b) East View

(c) West View (d) North View

Figure 3.19: Specimen U_4_L_5.50 Crack Patterns

Severe flexural and shear cracks were observed in Specimen U_4_L_5.50, and the failure mode could be classified as a combination of flexure and shear, rather than breakout. Furthermore, the radial cracks, accompanying the breakout cones, observed in all previous (single and two strand) specimens were still present. Severe cracks under the support posts were present as well.

Specimens U_4_L_9.25 and U_4_S_9.75 exhibit severe shear and flexural cracks but no radial cracks can be seen, propagating from the location of the strands (anchors)-the failure mode had fully transitioned from breakout to a combination of bending and shear. Severe flexural cracks can be seen on the bottom, diagonally across the specimens, underneath where the support HSS posts were placed. The bottom cracks ran perpendicular to the flexural cracks on the top. This is consistent with the fact that in a plate subjected to positive

(a) Top View

(b) Bottom View

(c) North View

(d) South View

(e) East View_1

(f) West View

Figure 3.20: Specimen U_4_L_9.25 Crack Patterns

bending in one direction, negative moments develop at 90° to the positive ones. Thus, on the bottom, compressive stresses were acting along the diagonal underneath the support posts, while tension stresses were generated perpendicularly to that diagonal, causing the splitting of the concrete.

This fact was overlooked during design, thus no bottom reinforcement was provided. Consequentially, the bottom cracks could not be inhibited and were quite wide- approximately $^1/_4$".

(a) Top View

(b) Bottom View

(c) North View

(d) South View

(e) East View_1

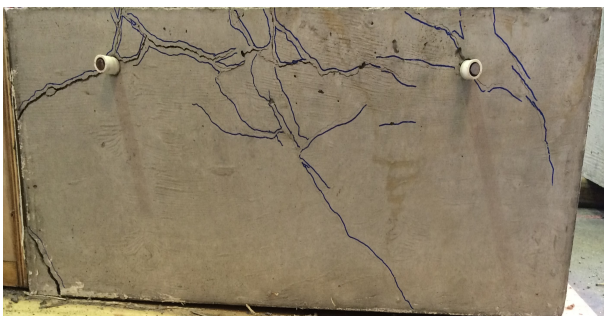

(f) West View

Figure 3.21: Specimen U_4_S_9.75 Crack Patterns

(a) Top View

(b) Bottom View

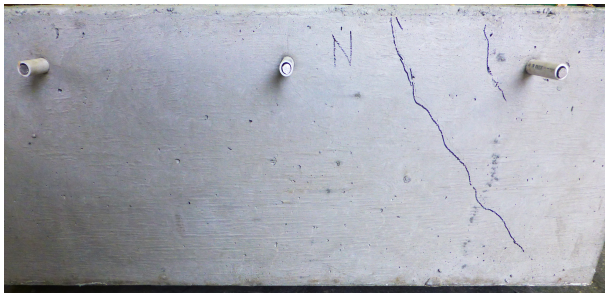

(c) North View

(d) South View

(e) East View_1

(f) [East View_2

(g) West View

Figure 3.22: Specimen U_4_S_14.50 Crack Patterns

For Specimen U_4_S_14.50, some flexural cracking can be observed on top of the specimen, while upon inspection of the sides, some shear cracks propagated down the sides and along the bottom of the specimen. The bottom view of the specimen shows concrete splitting, diagonally across the specimen, similarly to what was observed in Specimens U_4_L_9.25 and U_4_L_9.75.

For all cases of groups of strands with higher depth (up to 14.5") being tested in tension, the failure mechanism switched from breakout to a combination of flexure and shear.

(a) East View

(b) North View

(c) Top View

Figure 3.23: Specimen U_4_S_18.50 Crack Patterns

Finally, in the case of the deepest Specimen U_4_S_18.50, a maximum load of 231 kips was achieved and in order to prevent strand fracture, the test was terminated. Thus, it was concluded that for the given square pattern for four strands, a depth of about 19" would be the limit between flexural failure and a ductile failure due to fracture of the strands.

3.6 Analysis of Test Results

This section presents the comparison between test results and the predicted failure loads from the ACI, PCI and CCD procedures, and discusses the reliability of these models while determining the required embedment depth of the extended girder strands into the diaphragm, ensuring ductile failure.

3.6.1 Comparison Between Test Results and CCD, ACI and PCI Methods' Predictions

The specimens were designed according to the procedures described in ACI and PCI in order to achieve a breakout failure mode for certain target loads. The CCD method was not explicitly used when estimating the failure loads of the specimens, however since both of the aforementioned methods are based on the CCD method, it was, in fact the underlying design methodology.

Figures 3.24 to 3.27 show the failure loads obtained from the tests, as well as the curves obtained from following the procedures described in ACI, PCI and the CCD approach. The plots depict the failure loads, normalized with respect to the nominal strand strength, which was taken as the load, leading to strand fracture, $P_{frac} = 58\ kips$ for a single strand for varying block depths and strand patterns.

The failure loads predicted by the Concrete Capacity Design (CCD) method of analysis were a very close match to the ones obtained from the conducted tests. The procedures specified in ACI and PCI assume cracked concrete and are based on the 5% fractile of the database, used to develop the CCD method, while the CCD approach considers uncracked concrete properties. Thus, the ACI and PCI methods are more conservative and it was deemed appropriate to match the test data according to the CCD model, based on the mean values from Eligehausen's tests for uncracked concrete specimens, rather than using a 5% fractile and considering cracked concrete.

It should be taken under consideration that a very limited database was used - only 14 tests were conducted - and breakout failure was not achieved in all cases. In specimens with larger depths the failure occurred due to a combination of flexural and shear cracking. Yet, the test failure loads match the CCD model almost perfectly in all cases. It is for this reason that it cannot be claimed with absolute conviction that the CCD approach will be able to impeccably predict the capacity of a concrete member, regardless of the edge distance effects, and the anchor groups being investigated.

One thing can be deduced with certainty - the CCD method provides a lower bound to the true (exact) failure load for these tests. It is for that reason that the obtained results were deemed sufficiently close to the CCD method predictions, confirming that the CCD method can be used for a satisfactory estimation of the load capacities for possible strand patterns, extended from the girders into the diaphragm.

The summary of the tests, carried on specimens with single strands is shown in Figure 3.24.

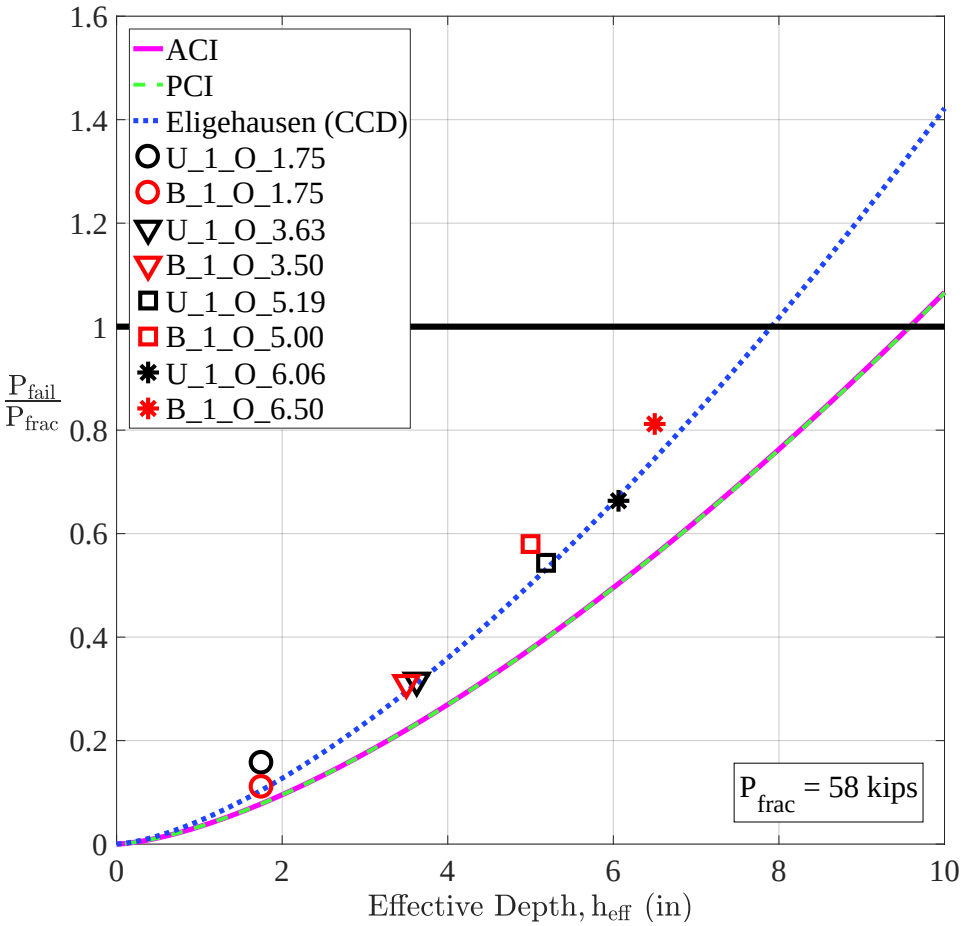

Figure 3.24: Normalized Failure Load vs Effective Depth for a Single Strand

Based on the fact that then test results fit the CCD model very closely, it can be deduced that for a strand anchored with a barrel anchor, an embedment depth of 8" would be sufficient

to ensure a ductile failure due to strand fracture.

The tests carried out on two strand specimens are summarized in Figure 3.25.

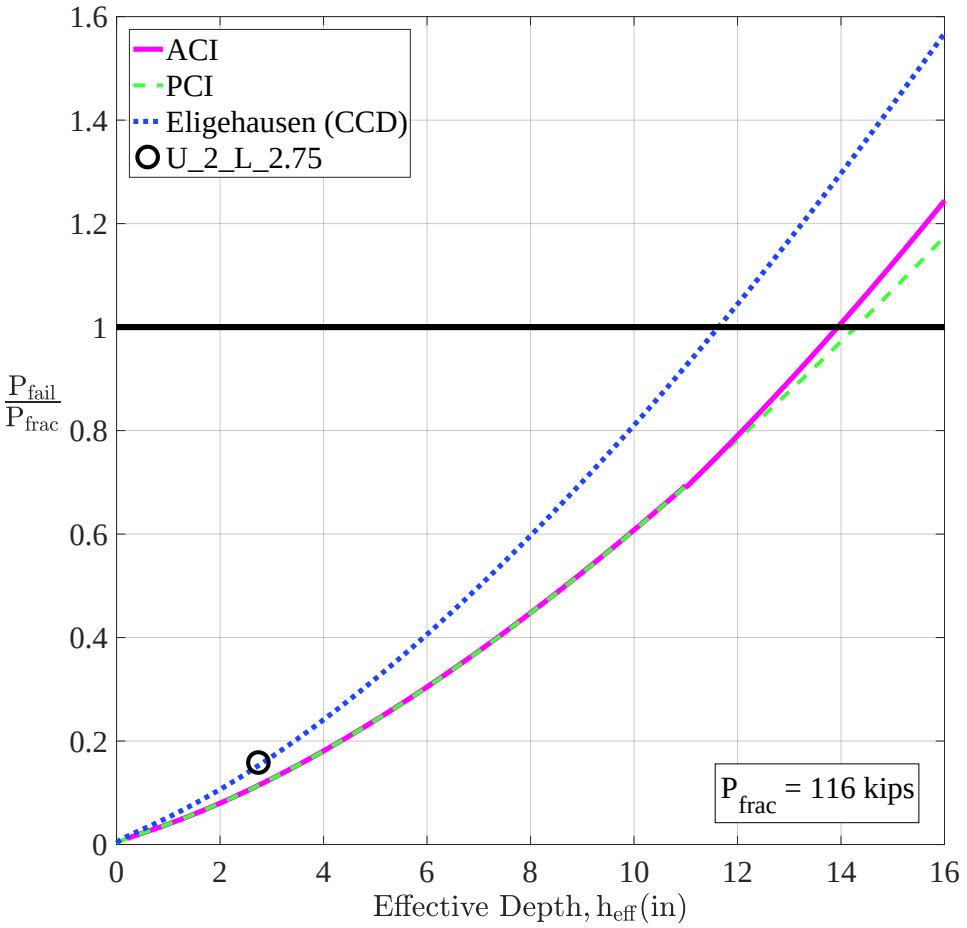

Figure 3.25: Normalized Failure Load vs Effective Depth for Two Strands

Considering the fact that the test data seems to fit the CCD model well, it can be concluded that the required embedment depth for two strands anchored with barrel anchors in order to prevent brittle failure of concrete would be about 11.5".

The results for tests, carried out on specimens with four strands in a line are depicted in Figure 3.26.

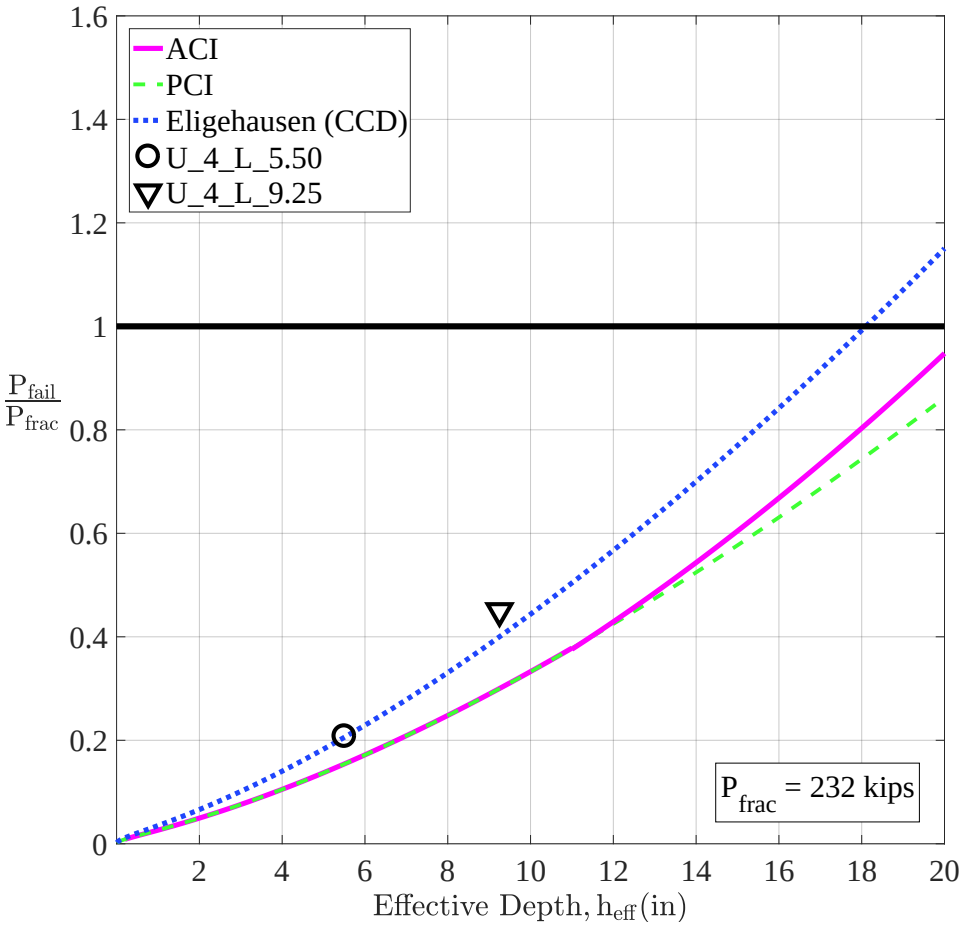

Figure 3.26: Normalized Failure Load vs Effective Depth for Four Strands in a Line

The test data fits the CCD model quite well; thus, it can be deduced that an embedment depth of 18" would be sufficient to prevent concrete breakout and provide a ductile failure mode for four strands equipped with barrel anchors in a line pattern, spaced 2" center-to-center.

The test results for specimens with four strands in a square pattern are summarized in Figure 3.27.

The test results match the CCD model very closely. Specimen U_4_S_18.50, which was the deepest specimen tested, did not fail and exhibited no cracking. To prevent strand fracture, the test was stopped at 231 kips, assuming a nominal strength of 232 kips for four strands (since $P_{frac} = 58\ kips$ for a single strand); thus the actual location of the point

representing that specimen would have been higher up on the plot as shown with the arrow on the plot, indicating that the prediction from the CCD model would likely be slightly smaller than the actual failure load, similar to all other cases.

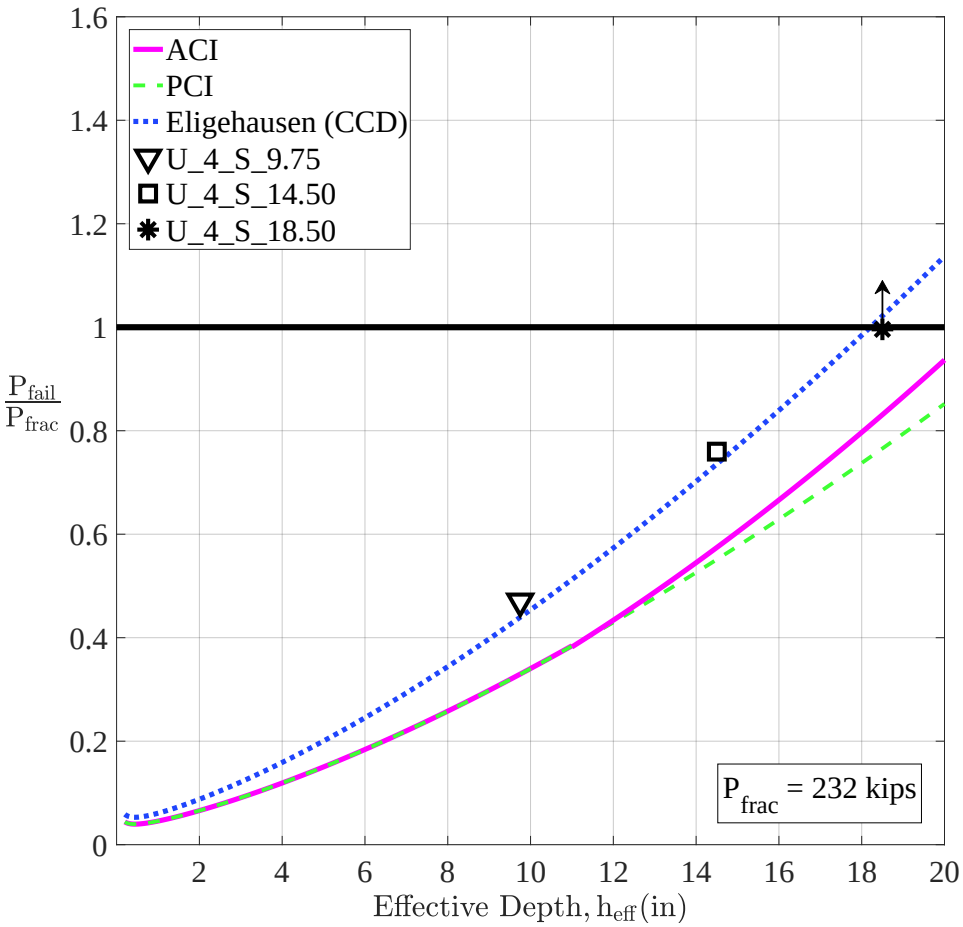

Figure 3.27: Normalized Failure Load vs Effective Depth- Four Strands in a Block

The summary of all ultimate test loads normalized with respect to CCD predictions vs the effective embedment depth is shown in Figure 3.28. As can be seen, the failure loads for the majority of specimens are about 1.1 times the predicted loads by the CCD method, leading to the conclusion that the Concrete Capacity Design model is the most reliable one among the three methods described in Section 3.2.

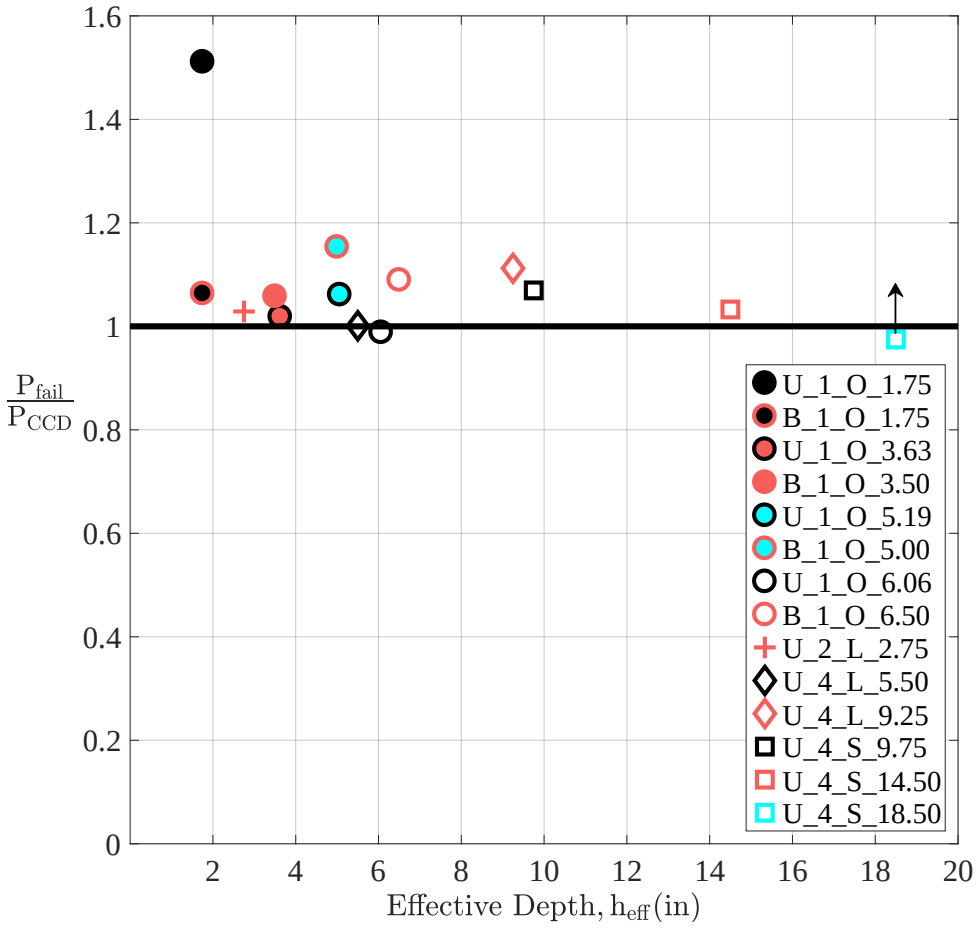

Figure 3.28: Normalized Failure Load vs Effective Depth - CCD

Overall, the failure loads obtained from experimental data fit the predicted values by the CCD method much more closely than ACI and PCI predictions. The CCD method was investigated after the conclusion of the experimental work and was explored upon the discovery of the conservatism of the ACI and PCI predictions in comparison with the observed test results.

3.6.2 Practical Implications of Breakout Tests

The diaphragm region in a typical Washington State bridge bent is very heavily reinforced, thus, a failure mode, resembling the breakout mechanism, may take place progressively, rather than suddenly. Since the extended girder strands will be bonded, a progression of

smaller cone failure surfaces would take place along the strand until full debonding occurred, at which point the strand anchor would bear on the stiff, undamaged concrete surrounding it, in order to resist the majority of the load. This stage represents the initiation of the expected 35° breakout failure surface, however its full development would be arrested by the presence of large amount of flexural and shear reinforcement, which provide a high degree of confinement. Still, considering how closely the test failure loads matched those, predicted by the CCD method, it can be used as a guideline in the determination of the required embedment length of the strands into the diaphragm.

3.7 Conclusions

The tests described in this chapter explored the possible failure mechanisms of strands anchored with barrel anchors, embedded in concrete blocks for different depths and tested in tension. The concrete block depths were designed according to procedures described in ACI and PCI documentation, such that a certain target breakout failure load was achieved. Since the test failure loads were always higher than the design failure loads, the Concrete Capacity Design method, which is the basis for developing the design methodologies adopted by ACI and PCI, was investigated and was found to sufficiently correlate to the test data.

Ultimately, since the test results matched the Concrete Capacity Design predictions so well, it was decided that it can be used to determine the minimum required embedment depths for different strand patterns to be extended from the girders into the diaphragm in order to prevent brittle failure due to concrete breakout, ensuring the occurrence of a ductile failure mode due to fracture of the strands. As a result of these tests, it has been concluded that using a smaller number of strands embedded in concrete drastically reduces the likelihood of the occurrence of a brittle breakout failure mode.

Chapter 4

DEVELOPMENT OF SUPERSTRUCTURE BRIDGE MODELS

4.1 Introduction

This chapter describes the analyses performed on the bridge superstructure in order to investigate the system behaviour under the impact of a longitudinal seismic load.

The goals of the analyses were to evaluate the distribution of girder bending moments across the bridge deck, and to investigate the influence on that distribution of the most important bridge parameters, such as cracking of bridge components, varying cross sectional dimensions, and span lengths. If the girder moment distribution is uniform, the number of strands extended from each girder required to develop the girder-diaphragm connection could be less than current practice.

The distribution of extended girder strands across the bridge deck depends on the distribution of girder end moments, which in turn depends on the ratio of the cap beam torsional stiffness to the girder bending stiffness. If the cap beam is torsionally very stiff compared with the flexural stiffness of the girders, the girder moments will be almost identical, and the same small number of strands could be extended from each girder end into the diaphragm.

Three methods of analysis were pursued to determine the distribution of bending moments among girders. The issue was investigated by considering a 3-D Finite Element model of a typical WSDOT bridge superstructure, followed by the analysis of a less complicated frame model, and was concluded by creating a continuous model.

4.2 UCSD Tests

Present practice in Washington follows the procedure specified in AASHTO Seismic Design Specifications (AASHTO, 2009), which is based on tests carried out on two 40%-scale model

bridge structures at the University of California, San Diego (UCSD) (Holombo et al., 2000).

The UCSD tests were based on a typical California cap beam, which is cast-in-place and flush with the bottom of the girders as shown in Figure 4.1.

(a) Single Column Bent (b) Bent Construction (c) Two Column Bent

Figure 4.1: Typical Integral Column Bents in California Bridges (Ma, 2008)

During the UCSD tests, the cap beam cracked under the effect of torsional moment, with the result that its stiffness was low, and the majority of the moment imposed by column bending was resisted by girders within an "effective width" of the column. The effective width is defined as the sum of the column diameter and the superstructure depth, $B_{eff} = D_c + D_s$, where D_c is the column diameter and D_s is the depth of the superstructure, including the cap beam, as illustrated in Figure 4.2.

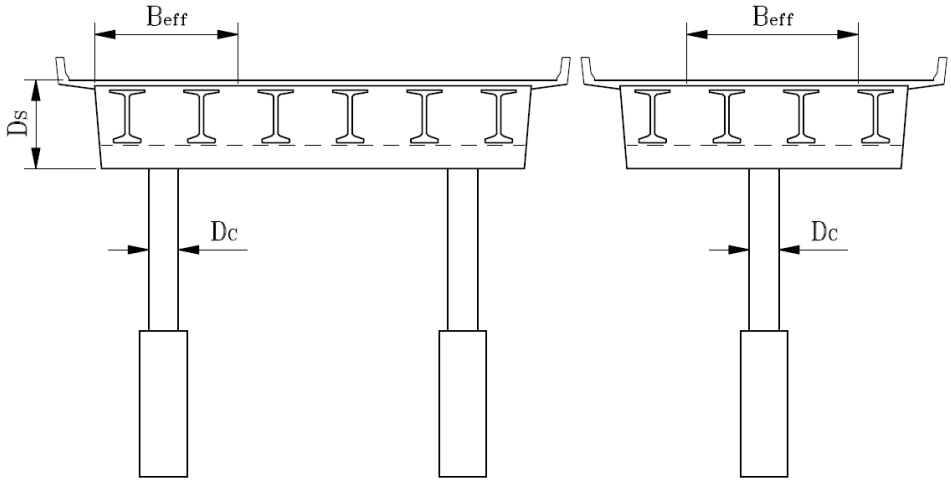

Figure 4.2: Effective Superstructure Width (WSDOT, 2015)

Holombo et al. estimated the contribution of exterior and interior girders to the resistance of the column plastic moment by considering the distribution of the longitudinal strains, measured in the deck reinforcement. They found that the longitudinal deck strains recorded over girders within the column effective width were approximately twice as large as the deck strains recorded over girders outside of the effective width of the column (Holombo et al., 2000).

4.3 Current Design Practice

Based on the results of the UCSD tests, AASHTO requires that unless an analysis is carried out to evaluate the stiffness of the girder-bentcap system, it should be assumed that the girders in close proximity to the column will resist $^2/_3$ of the column plastic moment and the non-adjacent girders will resist the remaining $^1/_3$.

The design guidelines in the WSDOT Bridge Design Manual (BDM), are based on the AASHTO requirements, and thus on the UCSD tests, and include the effective width assumption.

Based on the WSDOT BDM, for prestressed concrete girders with cast-in-place deck slabs, where some of the girders are outside the effective widths and the effective widths of the columns do not overlap, $^2/_3$ of the seismic moment acting at the centroid of the bridge superstructure will be resisted by girders within the effective width. Thus, the moment resisted per girder line for girders within the effective width can be calculated as shown in Equation 4.1.

$$M_{sei}^{Int} = \frac{2M_{po}^{CG}}{3N_g^{int}} \tag{4.1}$$

where

M_{sei}^{Int} is the seismic moment per girder line for girders within the effective width $(k-ft)$,

M_{po}^{CG} is the plastic hinging moment at the center of gravity of the superstructure $(k-ft)$, and

N_g^{int} is the number of girders located within the effective width.

The remainder of the seismic moment, resisted by exterior girders, can be determined as shown in Equation 4.2.

$$M_{sei}^{Ext} = \frac{M_{po}^{CG}}{3N_g^{ext}} \tag{4.2}$$

where

M_{sei}^{Ext} is the seismic moment per girder line for girders outside the effective width $(k - ft)$, and

N_g^{ext} is the number of girders, outside of the effective width.

Considering Equations 4.1 and 4.2, the seismic moment, M_{sei}, can be determined as shown in Equation 4.3.

$$\begin{aligned} &\text{If } M_{sei}^{Int} \geq M_{sei}^{Ext}, \text{ then } M_{sei} = M_{sei}^{Int} \\ &\text{If } M_{sei}^{Int} < M_{sei}^{Ext}, \text{ then } M_{sei} = \frac{M_{po}^{CG}}{N_g^{int} + N_g^{ext}} \end{aligned} \tag{4.3}$$

This seismic moment is the required moment capacity per girder line (WSDOT, 2015). Since two girder lines will nearly always be within the column effective width, M_{sei}^{Int} would always be the moment that is considered in the design of all girder lines. This results in a requirement that all girders be designed for the same end moment, and consequently, the same number of extended strands.

Be that as it may, the cap beams in the state of Washington are built in two stages, so the lower stage can support the precast girders at the time of their erection. The cap beams are larger, and consequently a more uniform distribution of girder moments across the bridge deck would be expected, when compared to a shallow cap beam, flush with the bottom of the girders. If this could be demonstrated, the same total number of extended strands, required to resist the seismic moment, could be spread over a larger number of girders. Consequently, the maximum number of strands extended from a single girder could be reduced, which would improve the block pullout strength for a given embedment distance.

It would also reduce the number of bar and strand conflicts that occur during erection. This is particularly true for curved bridges, for which the opposing girders in a girder line are not collinear. A reduced number of extended strands would thus provide better constructability and simpler fabrication through standardization.

4.4 3-D Finite Element Model

ABAQUS software was used to create a 3-D Finite Element model of a representative WSDOT bridge and analyze its behaviour under self-weight and longitudinal seismic load.

For the ABAQUS model, the bridge prototype parameters, such as column and cap beam dimensions, as well as girder type and span lengths, were selected upon examining the plans of ten typical Washington state bridges. An example of the drawings, showing the crossbeam detail, is given in Figure 4.3.

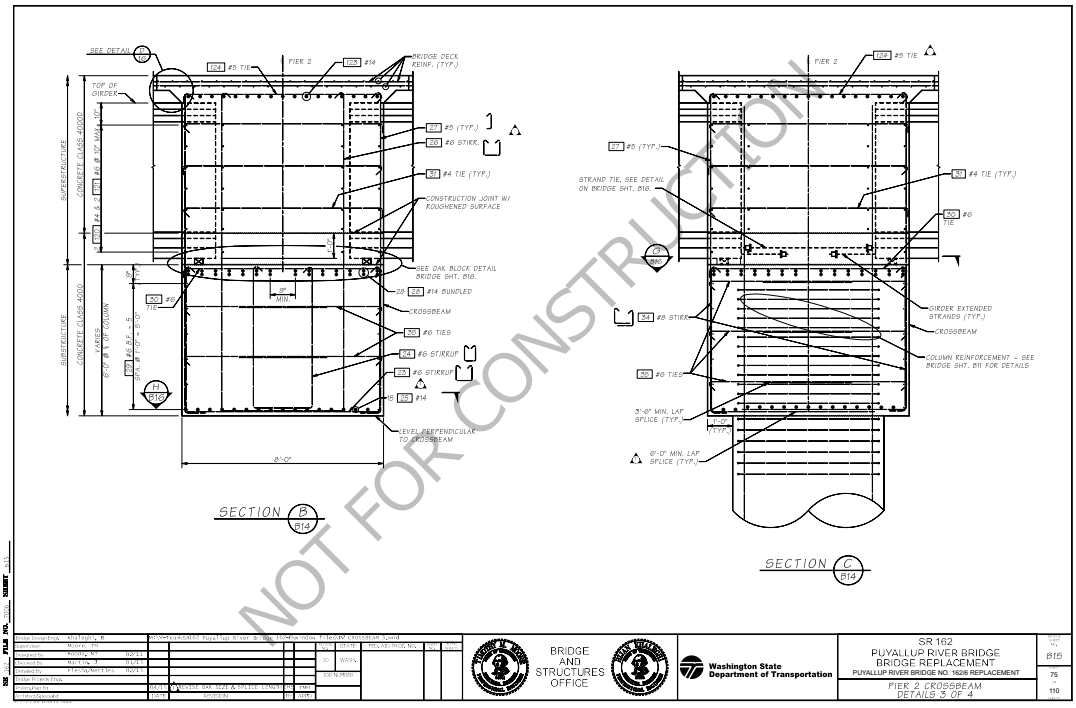

Figure 4.3: Puyallup River Bridge Crossbeam Details

The considerations for the development of the bridge model will be discussed as follows. First, the configuration of the model, followed by the description of the bridge components'

geometric and material properties, will be presented. Then, the elements and constraints used in the finite element model will be examined. Finally, the loading and boundary conditions applied in the model will be investigated.

The corresponding ABAQUS model is shown in Figure 4.4.

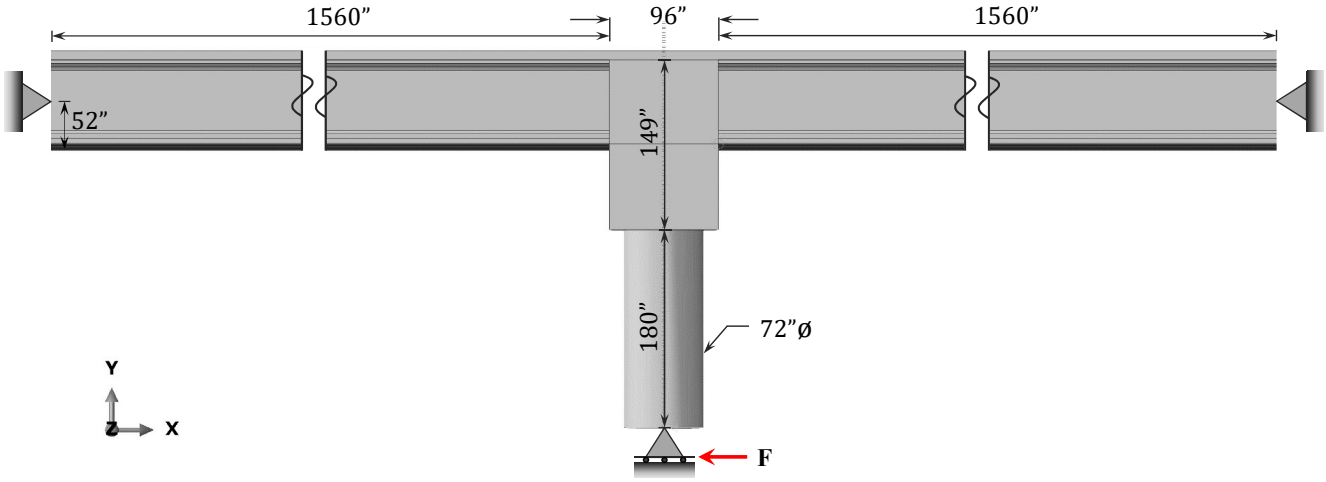

(a) Elevation View (X-Y Plane)

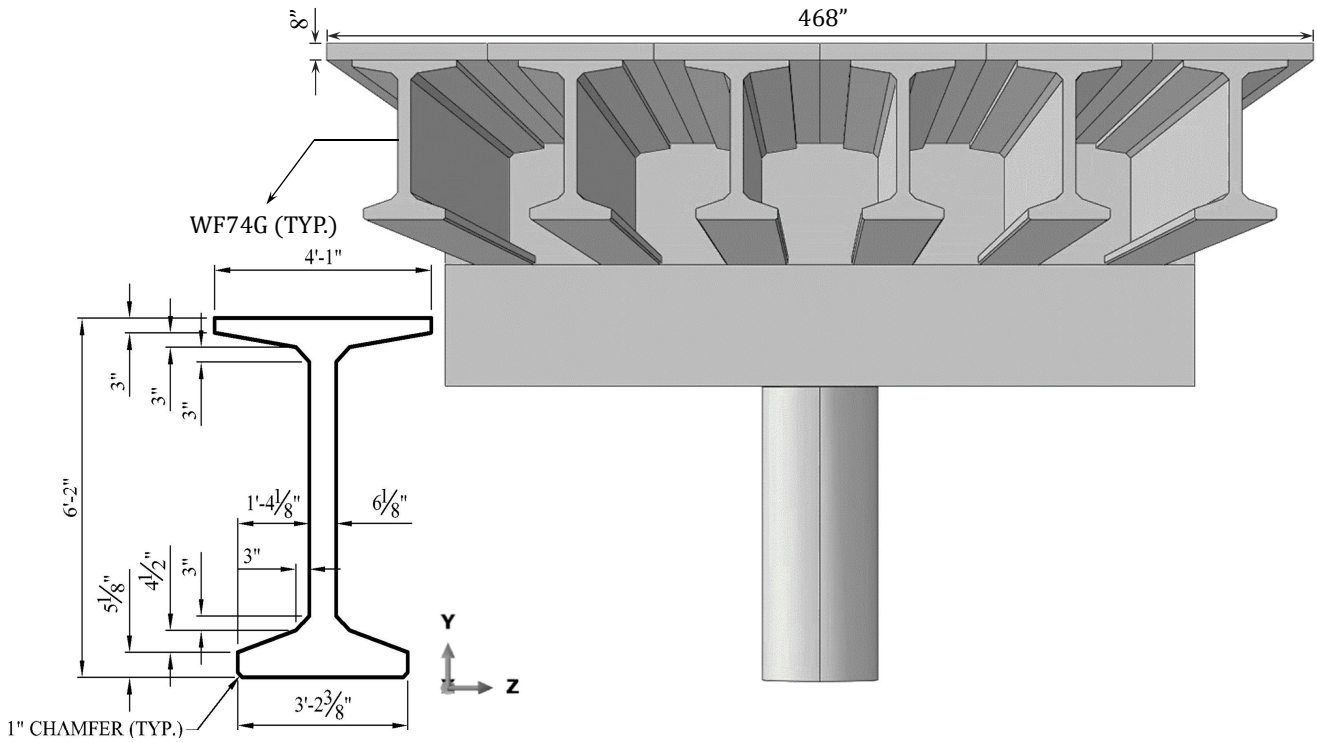

(b) Side View (Z-Y Plane)

Figure 4.4: ABAQUS Model

4.4.1 Bridge Prototype

The bridge model included a single pier and six WF74G girder lines, supported on a single-column bent. As previously mentioned, a typical Washington state cap beam system includes a crossbeam - a lower stage cap - on which girders are erected, and a diaphragm - an upper stage cap - which is cast after the girder erection, along with the deck. Consequently, Washington cap beams are much stiffer torsionally, and as a result, an more uniform girder bending moment distribution is observed, regardless of whether the column plastic moment is applied to the superstructure at a single point, which is the case in this model, or if the same total moment is distributed between multiple points, as it would be for a multi-column bent.

The pier had a circular cross-section with a 6' diameter and the cap beam cross-section was idealized as a rectangle. The end of each girder is, in practice, embedded in the cap beam for a short distance (14.5" for this bridge) as shown in Figure 4.3. However, in the model, that part of the girder was modeled as if it were a part of the cap beam, and the higher stiffness of the higher-strength girder concrete started at the outer face of the cap beam. To model the rest of the bridge superstructure, a composite section, including a typical WF74G girder cross-section and an 8" thick cast-in-place deck, was used. The spacing between composite sections was 6'-6" cc. Key dimensions are given in Figure 4.4.

The material properties for each component of the bridge are summarized in Table 4.1.

Table 4.1: Bridge Model Material Properties

Section	f '$_c$ (psi)	ω_{DL} (kcf)	ω_E (kcf)	E (ksi)
Column	5000	0.150	0.145	4074
Cap Beam	4000	0.150	0.145	3644
Girder	7000	0.165	0.155	5328
Deck	4000	0.155	0.150	3834

w_E and w_{DL} are the concrete unit weight values, taken from the WSDOT BDM, and used for the calculation of the modulus of elasticity, and for the calculation of the dead load,

respectively.

The modulus of elasticity, E, for each section was determined as per AASHTO LRFD Bridge Design Specifications with the expression shown in Equation 4.4 (AASHTO, 2012).

$$E = 33000\ K_1\ w_E^{1.5}\sqrt{f'_c} \tag{4.4}$$

where

$K_1 = 1.0$ is a correction factor for source of aggregate to be taken as 1.0 unless determined by physical test,

w_E is the unit weight of concrete (pcf), taken according to specifications in WSDOT BDM,

f'_c is the specified compressive strength of concrete (ksi).

The resulting values for E for each section are shown in Table 4.1.

4.4.2 Modeling Strategy

A linear elastic material model was used to model all bridge components, as the purpose was to show the general trend of the bridge behaviour under longitudinal seismic load.

The column, cap beam, and composite girders were all modeled as 3-D solid deformable bodies. The elements used for all components in the ABAQUS model were C3D8R, that is, continuum (solid), 3-D, 8-node, linear brick (hexahedral) elements with reduced integration, in order to achieve a less computationally expensive analysis. The cap beam geometry was simplified as a rectangle in order to facilitate the modeling in ABAQUS and avoid the use of tetrahedral elements, as the use of the latter may lead to shear locking, as well as underestimation of displacements and stresses, and is computationally expensive.

The column-crossbeam and diaphragm-girder surfaces were connected by the use of tie constraints, which are surface-based constraints, using a master-slave surface formulation. The ties prevent slave nodes from separating and sliding relative to the master surface and bond the surfaces permanently. The philosophy of the tie constraints involves the connection of every node on the master surface to its closest equivalent, located on the slave surface.

This type of constraint accounts for differences in meshing (different element sizes) in the slave and master surfaces. Models with and without tie constraints, used to connect the deck portions of the composite sections to each other, were compared to study the influence of a continuous deck on the overall system behaviour.

The boundary conditions of the model consisted of pin supports, located at the girder ends, restricting motion in the x, y and z directions, and of pin supports at the bottom of the column surface on two nodes in the X-Z plane, in the z direction, restricting motion in the y and z directions. The girder restraints were applied at the approximate centroid of the composite section, 52" up from the soffit. The effect of nonlinear geometry was not considered.

4.4.3 Loading

The applied load was estimated from the column flexural strength and length. A 6' diameter column with $\rho = 1.55\%$ reinforcement ratio was used in order to determine the plastic moment capacity, M_p, of the column. No reinforcement was explicitly considered in the model.

The column dimensions and reinforcement were obtained from the Puyallup River Bridge drawings.

The column was reinforced with 28#14 bars, thus

$$\rho = \frac{A_s}{A_{g,c}} = \frac{28(2.25)(4)}{\pi(72)^2} = 1.55\% \tag{4.5}$$

The ratio of the center-to-center distance between the longitudinal reinforcing bars to the diameter of the column, γ, was determined as follows.

$$\gamma = \frac{D_c - 2c_c - d_b - 2d_{b_t}}{D_c} \tag{4.6}$$

where

D_c is the column diameter (in),

c_c is the clear cover (in), chosen as 1.5" based on prototype bridge plans,

d_b is the diameter of the longitudinal reinforcement (in)

d_{b_t} is the diameter of the transverse reinforcement (in) (here, #9 hoops).

Then,

$$\gamma = \frac{72 - 2(1.5) - 1.693 - 2(1.128)}{72} = 0.903 \tag{4.7}$$

Column bending moment-axial force interaction diagram C-5-60-0.9, with $\gamma = 0.9$ was used to determine the column moment capacity (Wight and MacGregor, 2012). From the diagram,

$$\begin{aligned} \frac{\phi M_n}{A_g h} &= 0.51 \\ \phi M_n &= 0.51(A_g)(h) \\ 0.9 M_n &= \frac{0.51(\pi)(72^2)(72)}{4} \\ M_n &= 13800 \text{ k} - \text{ft} \end{aligned} \tag{4.8}$$

The plastic moment capacity was then equal to:

$$M_p = 1.2 M_n = 16600 \text{ k} - \text{ft} \tag{4.9}$$

For a column length of 15' to the inflection point of the load, a longitudinal seismic load $F = 1110$ kips was applied to the bottom surface of the column, such that the column plastic moment would be M_p at the top and zero at the bottom.

4.5 Line Element Model

In order to check the ABAQUS model, a wire frame model was developed, idealizing the system as a frame structure, using line elements. The stick model is shown in Figure 4.5.

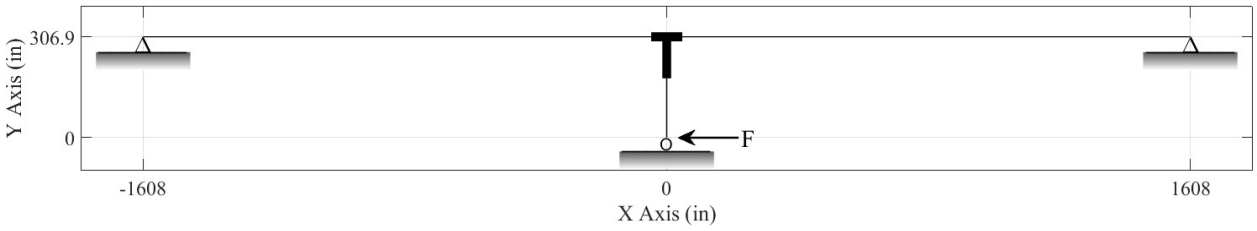

(a) Elevation View (X-Y Plane)

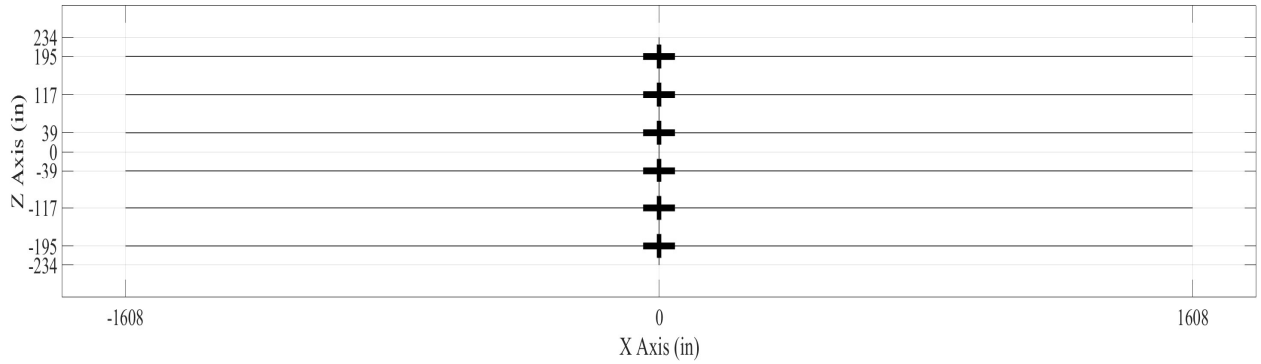

(b) Top View (X-Z Plane)

Figure 4.5: Stick Model

The discrete model consists of frame elements, which are deformable in bending and torsion, with the boundary conditions of the system consisting of a roller constraint at the bottom end of the column and pin constraints at the remote ends of the girders. A series of pairs of girders connect to the cap beam at a regular spacing in the horizontal (x) direction and the column frames into the cap beam at its midpoint from the bottom in the vertical (y) direction. Considering the behavior of the system under longitudinal seismic loading, the torsional rigidity of the cap beam and bending resistance of the girders govern the overall behavior of the system.

In terms of geometry, the cap beam cross section was idealized as a rectangle, the column had a circular cross section with a 6' diameter, and the girders were modeled as composite WF74G sections with 8" deck on top, similarly to the ABAQUS model. The system dimensions are shown in Figure 4.5, and the cross sectional properties correspond to the components shown in Figure 4.4.

The cap beam, column and girders of the real structure were represented as frame el-

ements located at the centroid of the real elements. To create the frame model, x, y and z coordinates for the nodes of each element were defined, and element node connectivities in terms of fixities of the x, y and z axis rotations and displacements were prescribed. A single-column bent with six girder lines is illustrated in Figure 4.5.

The moment acting at the centroid of the superstructure is significantly higher than the column plastic moment, M_p. To account for this effect in the frame model, rigid offset elements, originating from the intersection of the column centerline and centroid of the composite section and terminating at the sides and bottom of the cap beam, were added since the frame model represents components as wire elements through their centerlines. Thus, the girder elements were treated as rigid over a length 4' from the centerline of the cap beam, namely, over the half width of the cap beam. Rigid offset elements, which were 49" wide (girder top flange width) were used along the cap beam in locations where the girders were connected to it, in order to account for the fact that the cap beam would be stiffer in locations where the girders were framing into it. Similarly, a rigid offset element of 10'-7" was applied at the top of the column, such that the total torsional moment, acting on the center of gravity of the superstructure would be the same as in the ABAQUS model. The rigid offsets are shown as bold lines in Figure 4.5.

The boundary conditions of the system were the same as the ABAQUS model: the column was pinned at the bottom, restricting motion in the y and z directions, and the ends of the girders were pinned, restricting motion in the x, y and z directions, as shown in Figure 4.5a. No nonlinearities were considered.

A longitudinal load, $F = 1110$ *kips* was applied to the bottom of the column, similar to the ABAQUS model, as shown in Figure 4.5a. This resulted in the same moment acting at the superstructure center of gravity.

4.6 Continuous Model

As a third analysis strategy, a continuous model of the bridge superstructure was considered.

The cap beam was represented as a line element with torsional stiffness and it had rota-

tional springs, representing the bending stiffness of the girders, attached to it. The girder stiffnesses were smeared along the cap beam to create a distributed spring system. A closed form solution was developed for this system by considering a finite portion of the cap beam and idealizing it as a rectangular shaft under pure torsion as shown in Figure 4.6. The effect of gravity was ignored.

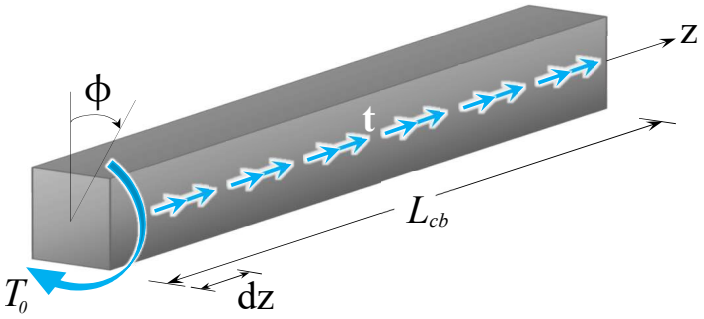

Figure 4.6: Continuous Model

The continuous model was instrumental in determining the dimensionless ratios of stiffness and geometry that govern the distribution of girder moments across the deck width. The torsional stiffness of the cap beam, GJ_{cb}, was obtained from its rectangular cross-section. The girder rotational resistance was represented by a continuous rotational spring of stiffness per length, β, which can be determined as follows.

$$\beta = \frac{2N_L}{L_{cb}}\left(\frac{3EI_g}{L_g}\right)\left(\frac{1}{(1-\alpha)^3}\right) \tag{4.10}$$

where

N_L is the number of girder lines across half the bridge width,

L_{cb} is the length of half of the cap beam (in),

I_g is the moment of inertia of the composite section (WF74G + 8" deck on top) (in^4),

L_g is the length of the girder span (in)

The factor 2 accounts for the fact that there are two girders per line, and the α accounts for the rigid end offset in each girder where the girders are attached to the cap beam. It is given by

$$\alpha = \frac{b_{g,eff}}{L_g} \tag{4.11}$$

where $b_{g,eff}$ is the rigid offset of the girders (in), which was taken as 48" (half of the cap beam width) for the reference bridge.

The derivation procedures of the expressions for the distributed spring constant β, as well as the angle of twist, ϕ, at any location, z, along the cap beam, are explained below. If β is the distributed spring constant per unit length, then, the torque applied by the spring to the cap beam, per unit length, is

$$t = -\beta\phi \tag{4.12}$$

The resisting torque is

$$T = GJ_{cb}\frac{d\phi}{dz} \tag{4.13}$$

As shown in Figure 4.6, from equilibrium,

$$\frac{dT}{dz} + t = 0 \tag{4.14}$$

By combining Equations 4.12 to 4.14, the governing equation for torque is obtained as follows.

$$GJ_{cb}\frac{d^2\phi}{dz^2} - \beta\phi = 0 \tag{4.15}$$

Let

$$\lambda^2 = \frac{\beta}{GJ_{cb}} \tag{4.16}$$

Then,

$$\frac{d^2\phi}{dz^2} - \lambda^2\phi = 0 \tag{4.17}$$

The solution has the following form

$$\phi(z) = Ae^{\lambda z} + Be^{-\lambda z} \tag{4.18}$$

which can equivalently be represented as

$$\phi(z) = A\cosh(\lambda z) + B\sinh(\lambda z) \tag{4.19}$$

Substituting Equation 4.19 into Equation 4.13, gives the torque

$$T(z) = GJ_{cb}\lambda\big[A\sinh(\lambda z) + B\cosh(\lambda z)\big] \tag{4.20}$$

If we consider half of the cap beam, with length L_{cb}, the torsional moment T_o, acting on the cap beam loaded end, originates as a bending moment in the column when the bridge is subjected to horizontal load. Then, this bending moment is transferred from the column to the cap beam as a torsional moment. The magnitude of T_o is half of the plastic hinging moment acting on the center of gravity of the superstructure.

At $z = L_{cb}$, namely, at the outer end of the cap beam, there is no torque acting on the cap beam; hence,

$$T(L_{cb}) = 0 = GJ_{cb}\lambda\big[A\sinh(\lambda L_{cb}) + B\cosh(\lambda L_{cb})\big] \tag{4.21}$$

Adjacent to the column, at z = 0, the torque T_o is acting on the cap beam; hence,

$$T(0) = T_o = GJ_{cb}\lambda\big[A\sinh(0) + B\cosh(0)\big] = GJ_{cb}\lambda B \tag{4.22}$$

As a result,

$$B = \frac{T_o}{GJ_{cb}\lambda} \tag{4.23}$$

From Equation 4.21,

$$A = -\frac{T_o}{GJ_{cb}\lambda}\coth(\lambda L_{cb}) \tag{4.24}$$

Thus,

$$T(z) = \big[-T_o\coth(\lambda L_{cb})\sinh(\lambda z) + T_o\cosh(\lambda z)\big] \tag{4.25}$$

and from Equation 4.19,

$$\phi(z) = -\frac{T_o}{GJ_{cb}\lambda}\frac{\cosh(\lambda L_{cb})}{\sinh(\lambda L_{cb})}\cosh(\lambda z) + \frac{T_o}{GJ_{cb}\lambda}\sinh(\lambda z)$$

$$\phi(z) = \frac{T_o}{GJ_{cb}\lambda}\left[\frac{-\cosh(\lambda L_{cb})\cosh(\lambda z) + \sinh(\lambda L_{cb})\sinh(\lambda z)}{\sinh(\lambda L_{cb})}\right] \tag{4.26}$$

$$\phi(z) = -\frac{T_o}{GJ_{cb}\lambda}\left[\frac{\cosh(\lambda(L_{cb} - z))}{\sinh(\lambda L_{cb})}\right]$$

Similarly, from Equation 4.20:

$$T(z) = T_o\left[\frac{\sinh(\lambda(L_{cb} - z))}{\sinh(\lambda L_{cb})}\right] \tag{4.27}$$

For the prototype bridge model, $\lambda L_{cb} = 0.435$.

The distribution of torque along the cap beam is illustrated in Figure 4.7.

The torque distribution along the cap beam is shown for two different values of λL_{cb}; $\lambda L_{cb} = 0.435$ for the reference structure, and $\lambda L_{cb} = 1.947$ for a structure, which has a smaller cap beam, which would have a much smaller torsional stiffness. This value is based on the UCSD bulb tee bent cap prototypes sectional and material properties. As it can be seen, the torsional moment distribution is much less uniform for a structure with low cap beam torsional stiffness.

The real structure consists of discrete girders and not a continuous rotational spring. Thus, the structure can be discretized to include a number of rotational springs, representing the girders, and as that number of girders approaches infinity, the model would behave as the continuous system, since the infinite number of springs would be equivalent to the girders being smeared along the cap beam.

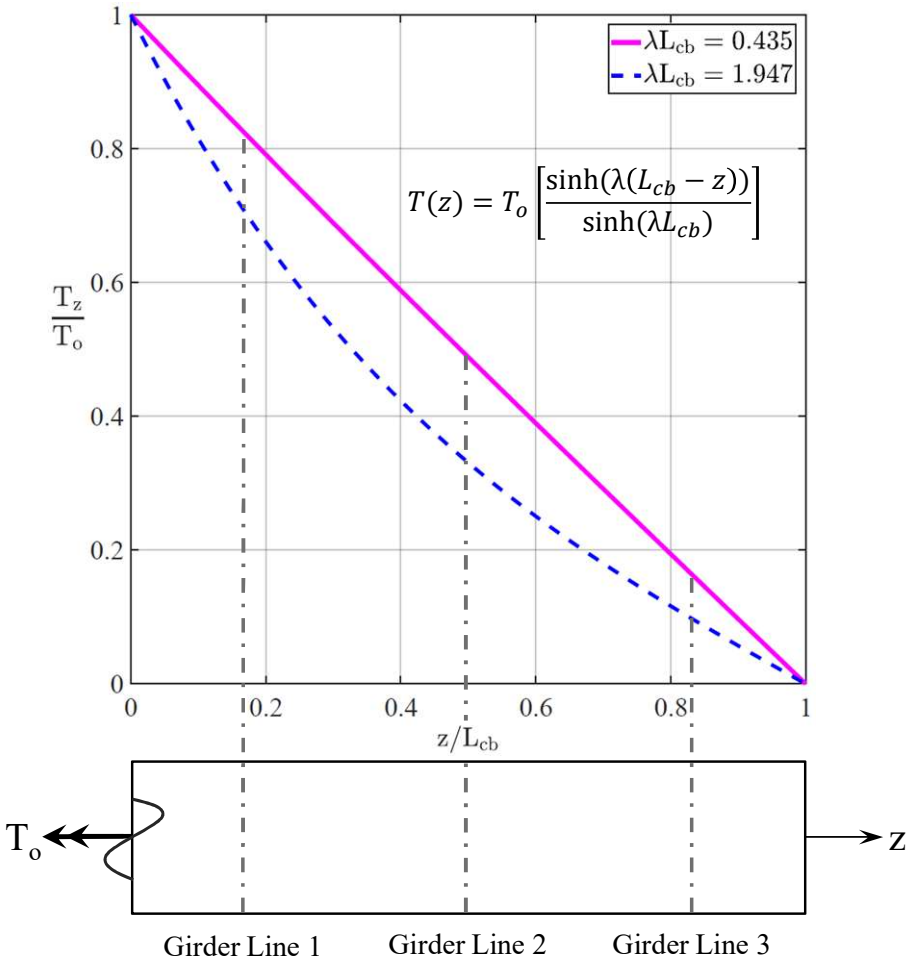

Figure 4.7: Torsional Moment Distribution Along Cap Beam

The moment attributable to each girder can be obtained as the change in torque in the cap beam from one side of the girder to the other. For girder line i, the relevant z values are

$$z_i = L_{cb} - i(s_g) \tag{4.28}$$

and

$$z_{i-1} = L_{cb} - (i-1)s_g \tag{4.29}$$

where

$s_g = \dfrac{L_{cb}}{N_L}$ is the girder spacing

and

N_L is the number of girder lines along (half of the) cap beam length L_{cb}.

This is shown in Figure 4.8. The structure depicted here is the prototype bridge and includes three girder lines within half of the cap beam length.

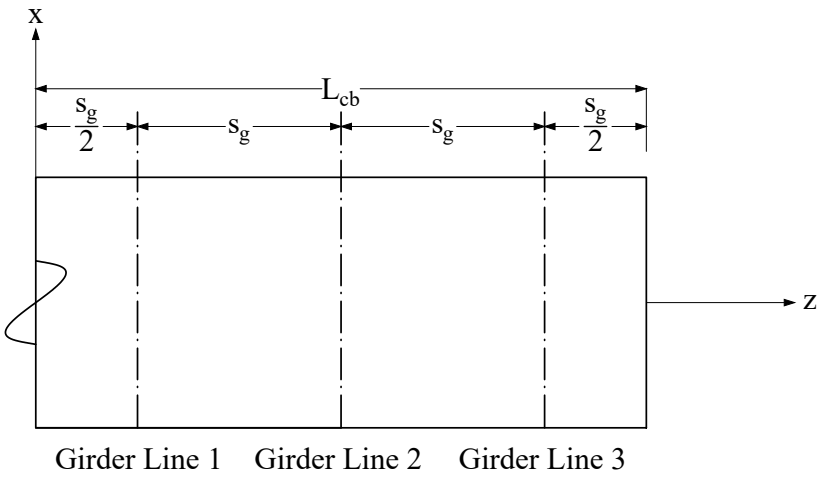

Figure 4.8: Discretization of Continuous Model

The moment in a single girder on line i is given by

$$M_{g,i} = \frac{1}{2}\frac{T_o}{\sinh(\lambda L_{cb})}\left[\sinh\left\{\lambda L_{cb}\left(1-\frac{i-1}{N_L}\right)\right\} - \sinh\left\{\lambda L_{cb}\left(1-\frac{i}{N_L}\right)\right\}\right] \tag{4.30}$$

where the factor $1/2$ accounts for the fact that two girders per line framing into the cap beam. Upon the application of several sum and difference of angle formulas for hyperbolic functions, Equation 4.30 can be further simplified to

$$M_{g,i} = T_o\frac{\sinh\left(\dfrac{\lambda L_{cb}}{2N_L}\right)}{\sinh(\lambda L_{cb})}\cosh\left\{\lambda L_{cb}\left(1-\frac{i-1/2}{N_L}\right)\right\} \tag{4.31}$$

The largest cap beam torque takes place in the regions closest to the column; hence, the girder lines located in the closest proximity to the column will exhibit the largest bending moments as shown in Figure 4.9.

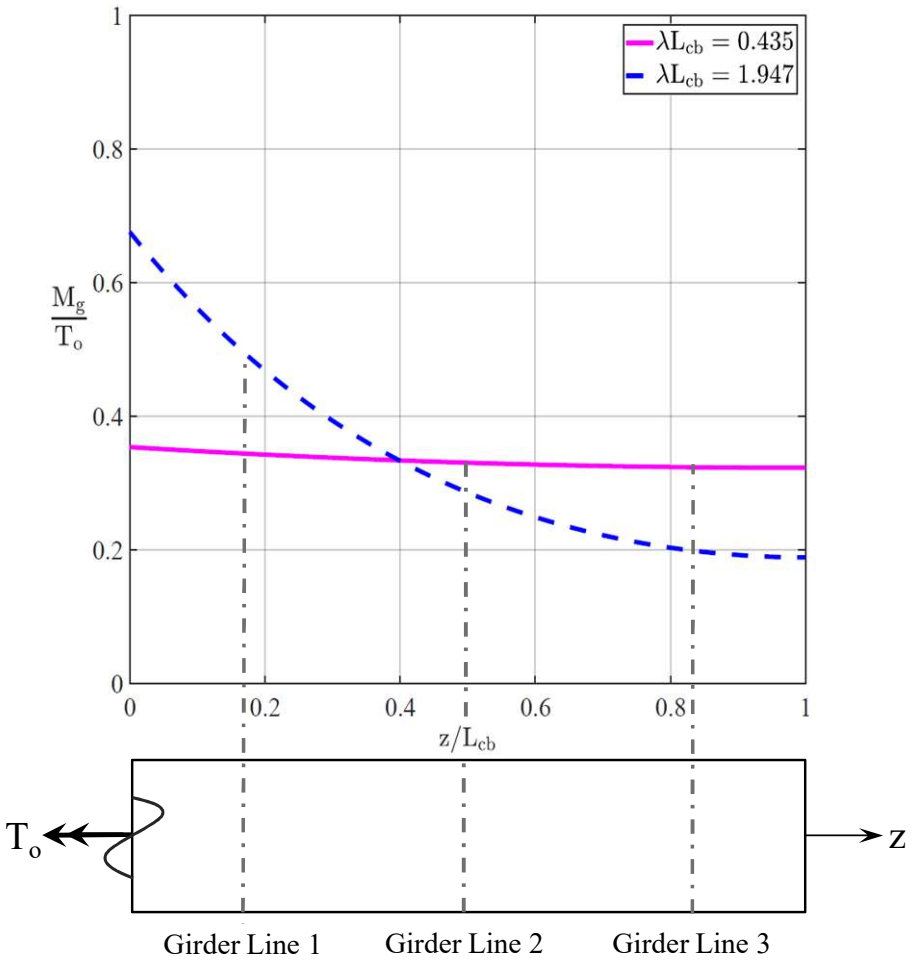

Figure 4.9: Girder Moment Distribution Along Cap Beam

The ratio of the maximum girder moment, $M_{g,max}$ to the average girder moments, $M_{g,avg}$, was selected as an appropriate normalization in order to depict the change in the bending moments in the girders along the cap beam with varying girder stiffnesses and number of girders.

The average moment across the N_L girder lines is

$$M_{g,avg} = \frac{T_o}{2N_L} \tag{4.32}$$

For the girder lines closest to the column, i = 1, so the ratio $\frac{M_{g,max}}{M_{g,avg}}$ is

$$\frac{M_{g,max}}{M_{g,avg}} = 2N_L \frac{\sinh\left(\frac{\lambda L_{cb}}{2N_L}\right)}{\sinh(\lambda L_{cb})} \cosh\left\{\lambda L_{cb}\left(1 - \frac{1}{2N_L}\right)\right\} \tag{4.33}$$

This development shows that the distribution of girder moments is controlled by the dimensionless parameters λL_{cb}, and N_L. λL_{cb} is the square root of the ratio of the flexural stiffness of the girders to the torsional stiffness of the cap beam.

$$\lambda L_{cb} = \sqrt{\frac{\beta L_{cb}^2}{G_{cb} J_{cb}}}$$

$$\lambda L_{cb} = \sqrt{\frac{(K_g/L_{cb}) L_{cb}^2}{G_{cb} J_{cb}}} \tag{4.34}$$

$$\lambda L_{cb} = \sqrt{\frac{K_g}{K_{cb}}}$$

where

$$K_g = \frac{2(N_L)3E_g I_g}{L_g(1-\alpha)^3} \tag{4.35}$$

which is the total flexural stiffness of all of the girders within half of the bridge width and

$$K_{cb} = \frac{G_{cb} J_{cb}}{L_{cb}} \tag{4.36}$$

which is the torsional stiffness of half of the cap beam.

Since the cap beam would be torsionally stiffened where the girders are connecting to it, a modification to increase the the cap beam stiffness was deemed necessary. This modification is similar to the use of a rigid end offset in the girders. The torsional stiffness of the cap beam was increased by increasing G_{cb}, rather than decreasing the free length between girders. The factor used was c_G, where

$$c_G = \frac{s_g}{s_g - b_{cb,eff}} \tag{4.37}$$

where $b_{cb,eff}$ is the rigid element offset along the cap beam, taken as 49" for the prototype bridge model.

Thus, the finalized expression for λL_{cb} would be

$$\lambda L_{cb} = \sqrt{\frac{(2N_L)3E_g I_g L_{cb}}{G_{cb} c_G J_{cb} L_g (1-\alpha)^3}} \tag{4.38}$$

Chapter 5

SUPERSTRUCTURE ANALYSIS RESULTS AND DISCUSSION

5.1 Introduction

A parametric study was conducted in order to investigate the effects of varying some of the important parameters in the ABAQUS Model, Stick Model and Continuous Model. First, the structure was investigated under uncracked elastic conditions, and the effects of changing the member stiffness, global geometry, and number of girders were studied. Then, the effects of concrete cracking and strand yielding were investigated. Finally, the results of the parameter study were correlated, and were compared with Priestley's recommendations (discussed in Chapter 4).

5.2 Elastic Uncracked Sections - Effect of Rigid-End Offsets (REO)

The part of the structure for which girder moment distributions will be evaluated, as well as the girder line numbering, are depicted in Figure 5.1.

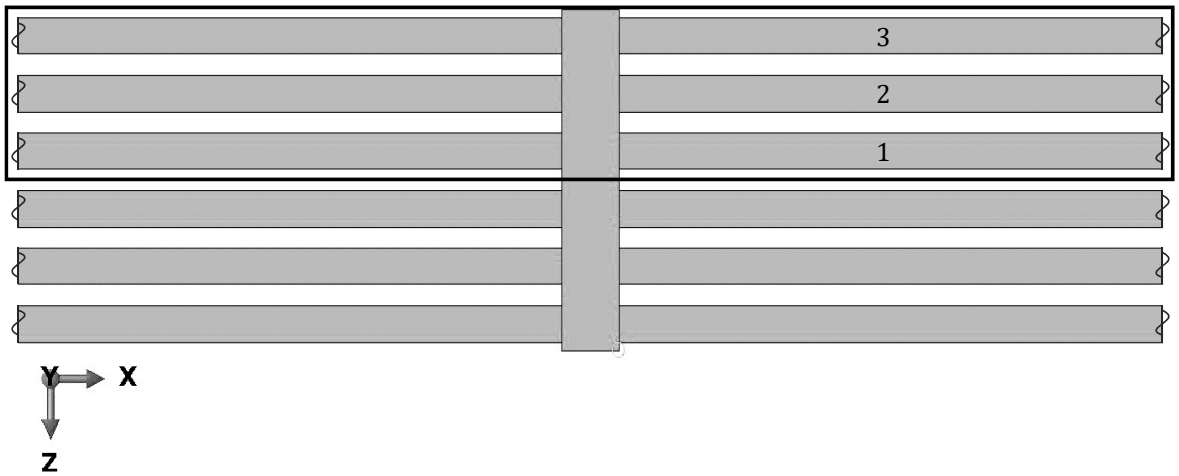

Figure 5.1: ABAQUS Model Top View (X-Z Plane) and Girder Numbers

As it can be seen, a bridge bent with six girder lines across the full bridge width was used as a reference structure in order to compare the behaviour, predicted by the different models.

5.2.1 Calibration Between Models

A single ABAQUS model was used to determine the girder moments for the reference structure. All bridge components were solid elements, and thus there was no need for rigid end offsets used in the other two models. As the joint region is not completely stiff, the lengths of the rigid end offsets are expected to not be exactly equal to the widths of the cap beam and girder sections.

The stick and ABAQUS models were run with uncracked elastic material properties, and the rigid end offsets in the stick model were adjusted as follows. The girders were treated as 49" wide, and the cap beam was treated as torsionally rigid within that width. Realistically, since only the girder top flanges are 49" wide, the true width, over which the cap beam should be considered torsionally rigid is actually less than 49". Thus, to check the effect of the girder width, portions of the cap beam between girders, which are torsionally flexible, were considered as both the full 78", which was the center to center spacing between girders, and 29", which would be the clear spacing between girders. It was deemed sufficient to check these two most extreme cases, with the prior being the worst case scenario, where essentially the girders provide no torsional rigidity to the cap beam, and the latter being the best case scenario, where the girders provide maximum torsional rigidity to the cap beam.

The continuous model matched the other two models when rigid end offsets for full width of the cap beam and girder sections were used.

Considering elastic uncracked section properties for all bridge components, the distribution of girder moments is shown for all three models for the reference Puyallup River structure in Figure 5.2. This plot depicts the moment distribution in terms of the girder bending moment, normalized with respect to the average moment in all girders (a total of 3 girder lines), considering half of the bridge superstructure.

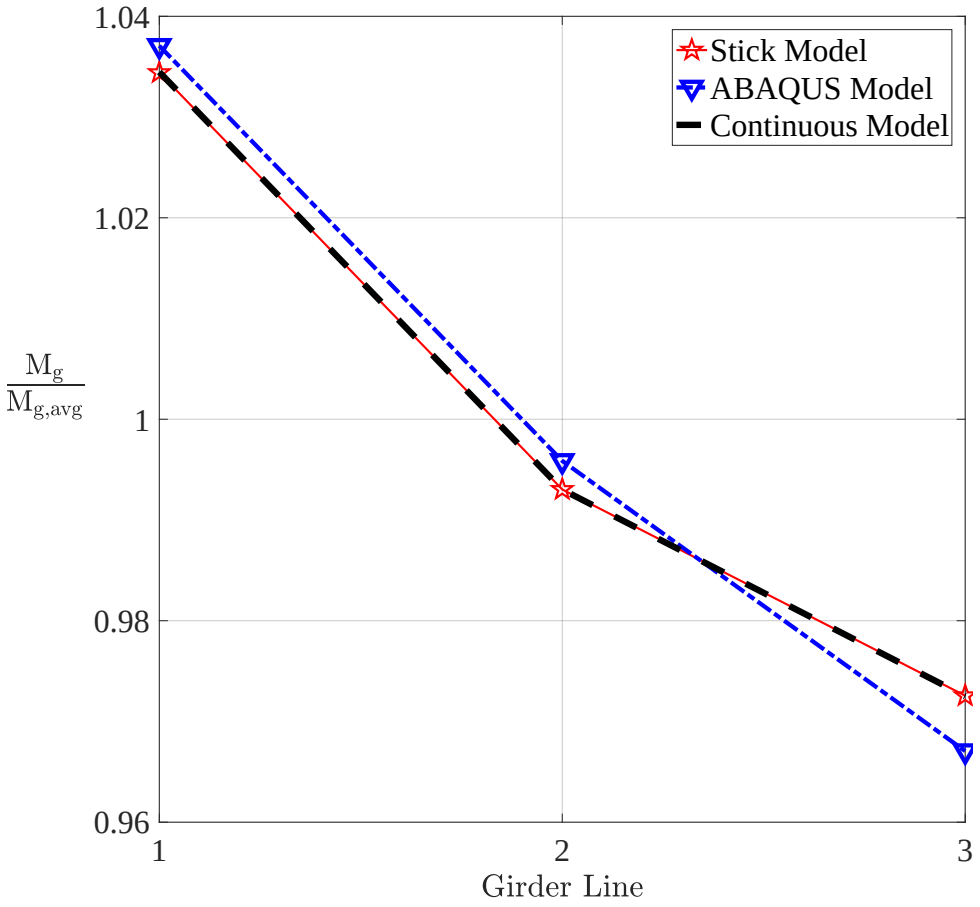

Figure 5.2: Girder Moment Distribution Along Half Cap Beam, Full Width REO

All three models agree in terms of the general trend regarding the girder bending moment distribution, namely, that the girder moments are almost uniformly distributed, with highest magnitudes closest to the pier. This distribution is expected, since the largest torsional moment in the cap beam is located in the middle of the cap beam and that moment magnitude gets smaller with distance farther and farther from mid-cap beam. The cap beam would transfer that torsional moment as a bending moment to the girders, and the largest bending moments would occur in girders closest to the column, which is the case here. The maximum girder moment is less than 4% larger than the average moment. The Stick Model and the Continuous Model give almost identical results, whereas the ABAQUS model deviates slightly. The ABAQUS model values vary within less than 0.6% from the other models thus, the results are deemed acceptable. Furthermore, the results depicted here include the full

width rigid end offsets (REO), namely, 48" along each girder, and 49" along the cap beam, wherever girders are connected to it, for both the Continuous and Stick Models.

To check the effect of the rigid offsets, results for the Stick and Continuous Models without including any offsets were compared with the previously shown results for all models, which included the rigid offsets. This is shown in Figure 5.3.

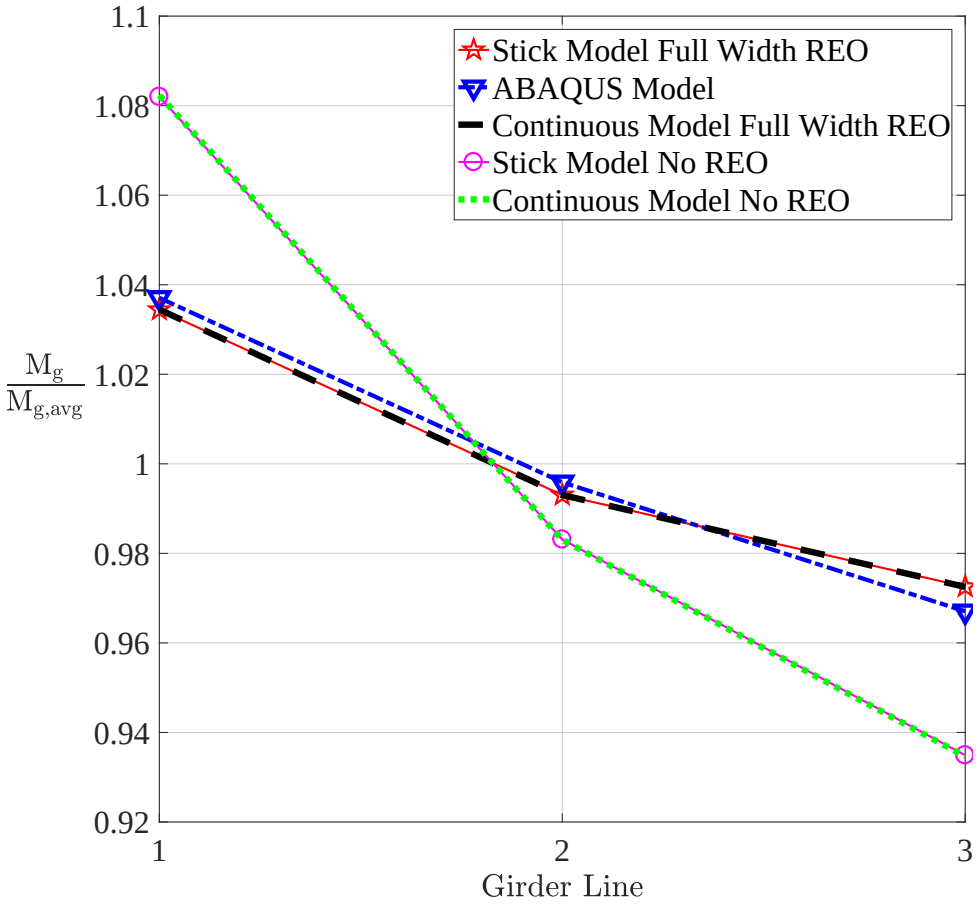

Figure 5.3: Girder Moment Distribution Along Half Cap Beam REO Impact

As it can be seen, the girder moment distribution is less uniform when rigid end offsets are ignored. This is to be expected as ignoring the rigid end offsets assumes the cap beam is less torsionally stiff than it would be in reality. It was discovered that the difference in girder moments was less than 5% between stick models (or continuous models since they behave the same) when rigid end offsets were accounted for and when their effect was excluded.

5.3 Elastic Uncracked Sections - Effect of Stiffness Ratio

The distribution of moments among the girders depends on the relative stiffnesses of the girder and cap beam. The two parameters that determine girder bending moment distribution are λL_{cb} and N_L, which are defined in Section 4.6. It is convenient to separate these two parameters, such that the total girder stiffness, $K_g = \frac{(2N_L)3E_gI_g}{L_g(1-\alpha)^3}$ would always be kept the same by reducing E_gI_g for increasing N_L. That way, considering Equation 4.33, one would be able to observe the variation in moment distribution for a constant number of girder lines, N_L, and varying λL_{cb} values. In a similar manner, when the distribution of moments with varying N_L is investigated, it would be ensured that λL_{cb} stays constant.

The effects of changing the relative stiffnesses between the girders and cap beam, namely by varying λL_{cb}, were studied using the geometry of the reference structure (three girder lines in the half width of the deck), and rigid-end offsets equal to the full beam width. The stiffness of the girders was varied from 0.069 to 20 times their reference value. The lower limit was selected based on the bending stiffness of a cracked WF74G girder, which would be approximately 6.9% of its uncracked stiffness. The upper limit, 20, represents the ratio of girder bending to cap beam torsional stiffnesses which would take place if the cap beam were to crack completely, resulting in it having a torsional stiffness equal to 5% of its uncracked value. The λL_{cb} value will change either due to a variation in the cross-sectional dimensions of the girders and/or the cap beam, or due to cracking. The effect of the latter will be discussed later in more detail. For reference, $\lambda L_{cb} = 0.435$ is the value for the reference structure model for uncracked elastic section properties and the corresponding moment ratio $\frac{M_{g,max}}{M_{g,avg}} = 1.040$ for the ABAQUS model and $\frac{M_{g,max}}{M_{g,avg}} = 1.035$ for the Stick and Continuous models.

The ratio $\frac{M_{g,max}}{M_{g,avg}}$ is plotted against λL_{cb} in Figure 5.4. The plot shows that the ratio $\frac{M_{g,max}}{M_{g,avg}}$ increases with increasing λL_{cb}, that is, as the girder bending stiffness increases relative to the torsional stiffness of the cap beam.

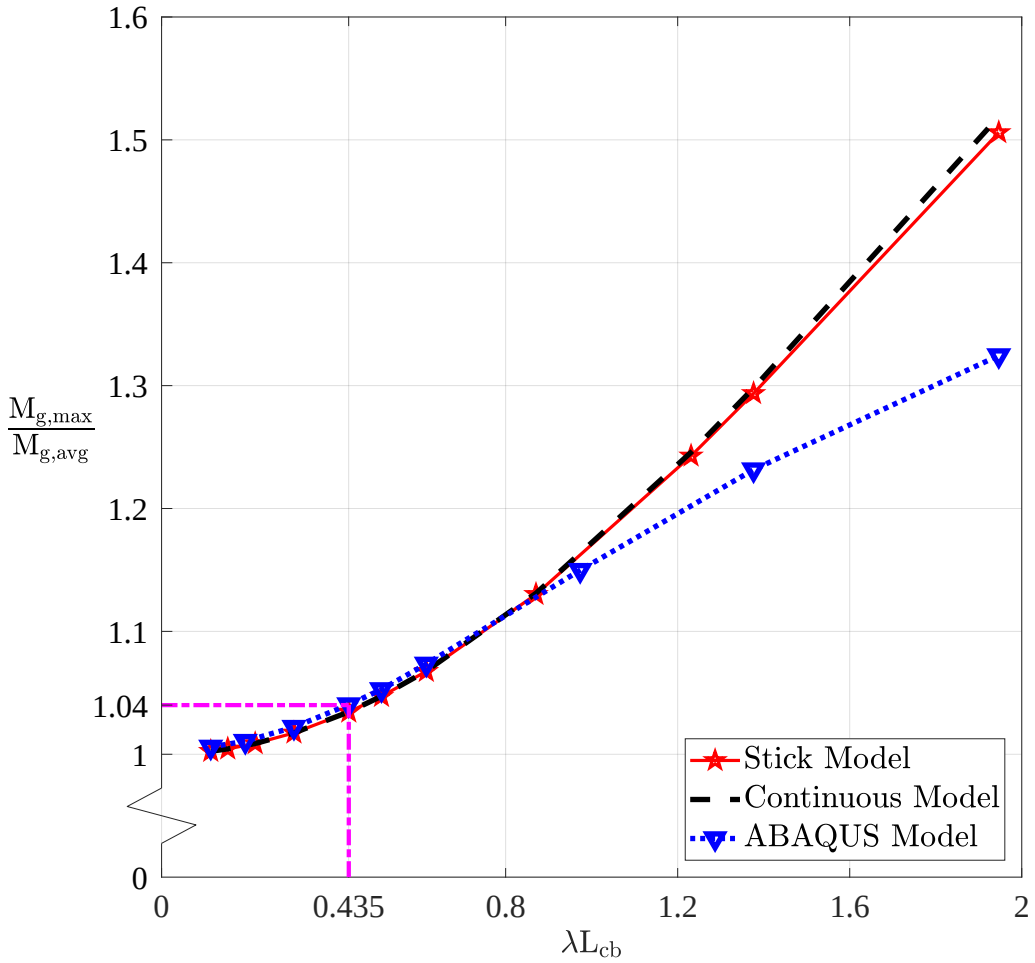

Figure 5.4: Girder Moment Distribution with Varying Stiffness Ratio, Full REO, $N_L = 3$

The ABAQUS model is a more complicated finite element model, compared to the stick model, and some of the 3-D solid element interaction might be causing the observed trend, since the girder moments, obtained from ABAQUS are more uniformly distributed compared to the other models. However, at low values of λL_{cb}, which are expected to occur in practice, the ABAQUS model approaches the exact solution and follows the trend of the other models.

All in all, the expected system behaviour is similar for all three models.

The combined effect of the simultaneous change in both number of girder lines, N_L and the stiffness ratio λL_{cb} on the girder end moment distribution was studied by using only the stick and continuous models. It would have been very time consuming to make enough ABAQUS models, varying both the girder and cap beam sizes, and the number of girder

lines each time, in order to investigate all cases presented in Section 5.4. Since the ABAQUS model results agree so closely with the other two models for the effect of changing λL_{cb} alone, particularly for the low λL_{cb} range, which is expected to occur in practice, the use of the simplified models was deemed appropriate.

5.4 Elastic Uncracked Sections - Effect of Number of Girders

The effect of the second parameter, namely number of girder lines, N_L, on the girder moment distribution, is complicated by consideration of the rigid-end offsets. If the cap beam length had been kept constant, while the number of girders increased, the space between girders would diminish and the cap beam would become stiffer in torsion, thereby changing λL_{cb}. If rigid end offsets were accounted for, the cap beam would become torsionally stiffer, making the distribution of girder moments more uniform. The extent to which this happens depends on the size of the rigid end offset. Thus, that feature of modeling affects the influence of the number of girders. Ergo, to investigate the effect of changing the number of girder lines, the rigid end offsets in the stick and continuous models were ignored and the stiffness ratio $\lambda L_{cb} = 0.681$ was used in all cases. Until now $\lambda L_{cb} = 0.435$ for the reference structure for uncracked section properties, because full width rigid end offsets were used. $\lambda L_{cb} = 0.681$ is the stiffness ratio, corresponding to uncracked section properties, considering the reference model with no rigid offsets.

The stick model was developed for a superstructure with a minimum of 3 and a maximum of 8 girder lines along half of the bridge width, in order to see the difference in the girder moment distribution for a smaller number of larger girders (corresponding to the reference structure) and a large number of small girders. The maximum number of girders in the half width of the bridge was limited to 8, because this is likely to be an upper bound to the number of girders used in practice. The cap beam length and the total girder stiffness were kept the same as in the reference structure, while the number of girders and their individual stiffnesses were varied. The variation in the normalized girder moments corresponding to their respective girder lines is shown for 3 and 8 girder lines across half of the cap beam width in Figure 5.5.

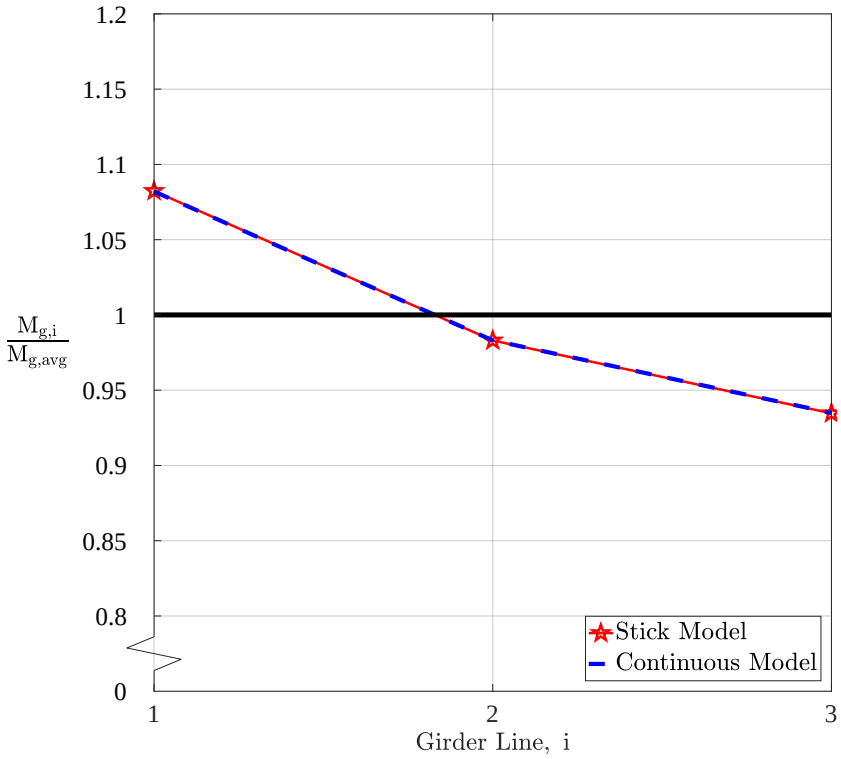

(a) 3 Girder Lines

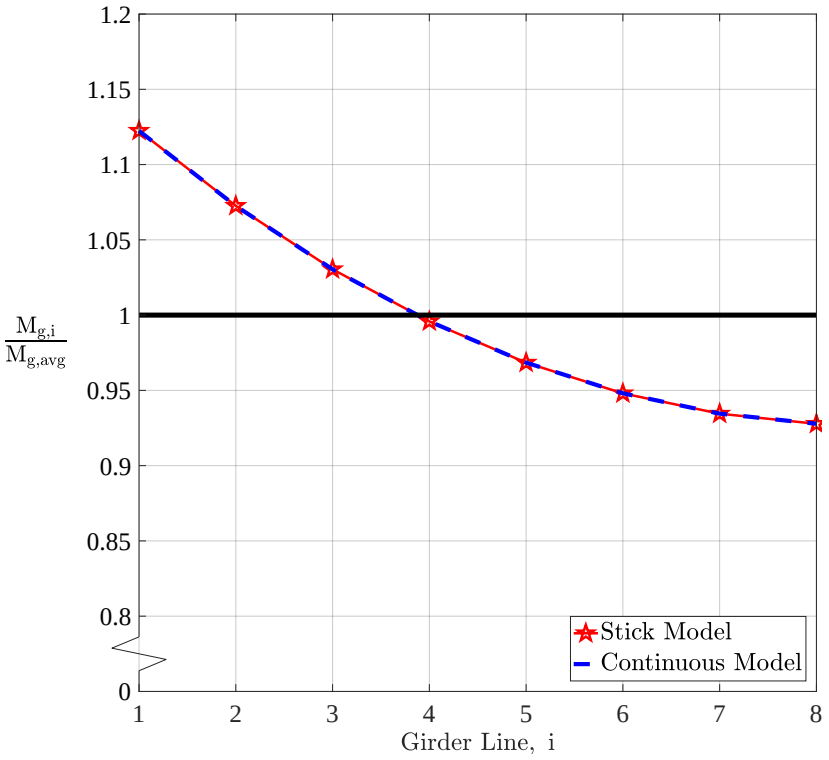

(b) 8 Girder Lines

Figure 5.5: Girder Moment Distribution vs Number of Girder Lines, No REO, $\lambda L_{cb} = 0.681$

In conclusion, the use of more and smaller girders leads to maximum girder moments that are higher proportions of the average.

Equation 5.1, which predicts the maximum girder moment using the continuous model as a function of the number of girders, can be used to find $\frac{M_{g,max}}{M_{g,avg}}$ as N_L approaches infinity. The limit is

$$\frac{M_{g,max}}{M_{g,avg}} = 2N_L \frac{\left(\frac{\lambda L_{cb}}{2N_L}\right)}{\tanh(\lambda L_{cb})} = \frac{\lambda L_{cb}}{\tanh(\lambda L_{cb})} \tag{5.1}$$

As λL_{cb} increases, $\frac{M_{g,max}}{M_{g,avg}}$ approaches λL_{cb}.

Figure 5.5 shows results for a single λL_{cb} value and variable number girder lines, N_L. The change in $\frac{M_{g,max}}{M_{g,avg}}$ for several N_L and variable λL_{cb} values is illustrated in Figure 5.6. It shows that, for large enough total girder bending stiffness to cap beam torsional stiffness ratio, λL_{cb}, the moment ratio is asymptotic to N_L. This implies that all the moment is resisted by the first line of girders, which is what is to be expected when the girders are very stiff relative to the cap beam. This can also be shown mathematically, because for very large λL_{cb}, looking back at Equation 4.33, an indeterminate form $\frac{\infty}{\infty}$ is observed and by using L'Hospital's Rule, Equation 4.33 approaches

$$\frac{M_{g,max}}{M_{g,avg}} = N_L \tag{5.2}$$

However, the λL_{cb} values required to achieve this result are much higher than the ones likely to occur in practice. The girder moment distribution for various numbers of girder lines and for a restricted and more practical range of λL_{cb} values is shown in Figure 5.7.

As can be seen in Figure 5.6 and Figure 5.7, the girder moments distribution is less and less uniform for a larger number of girders for the same λL_{cb} value.

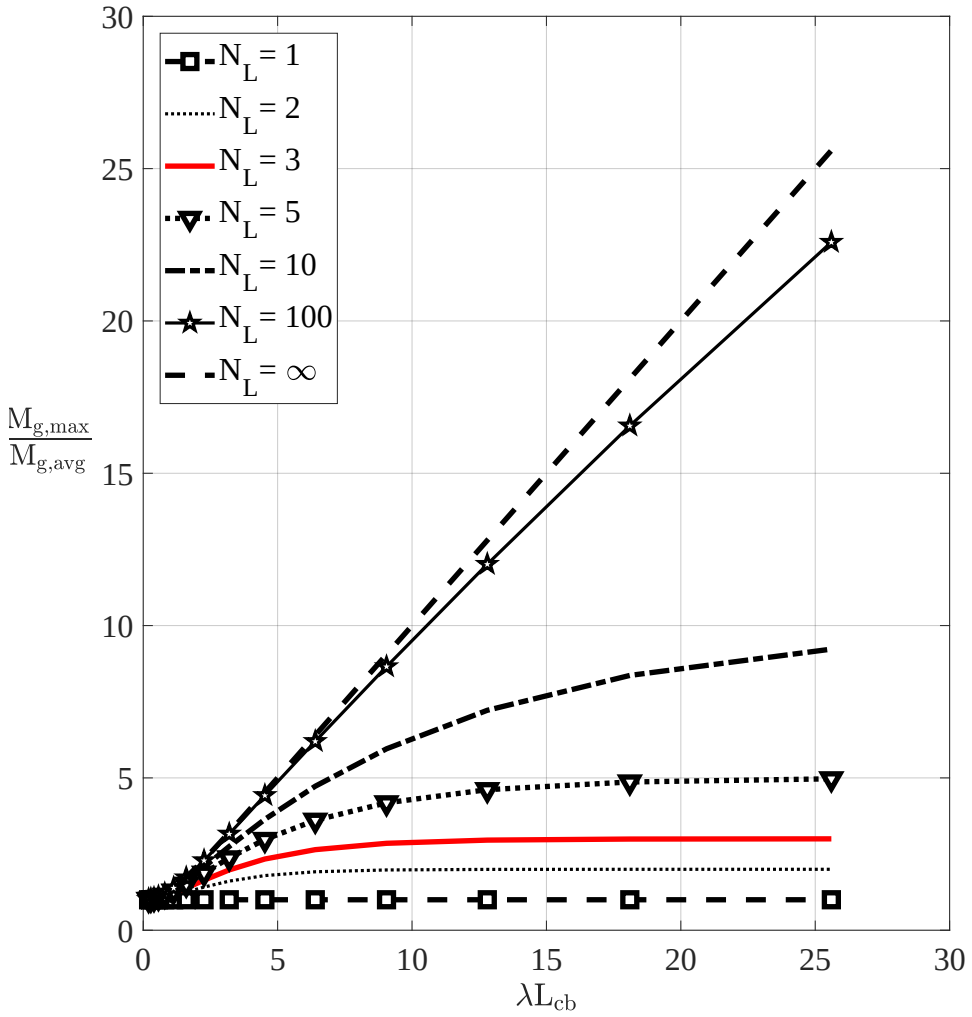

Figure 5.6: Girder Moment Distribution with Varying Stiffness Ratio for Different Number of Girder Lines, No REO

As N_L becomes large, the maximum girder moment approaches the limiting value λL_{cb}, and this suggests that normalization by $M_{g,avg}$ may be useful when the number of girders is small, but less so when many small girders are used. In case of the latter, normalization by half of the torsional moment acting on the centroid of the superstructure, T_o, may be more useful. However, for the current normalization, as λL_{cb} becomes very large, i.e. when the girders are much stiffer than the cap beam, the ratio $\frac{M_{g,max}}{M_{g,avg}}$ converges to the number of girder lines (along half the width of the bridge), N_L. Then, the interior girders will resist all of the moment.

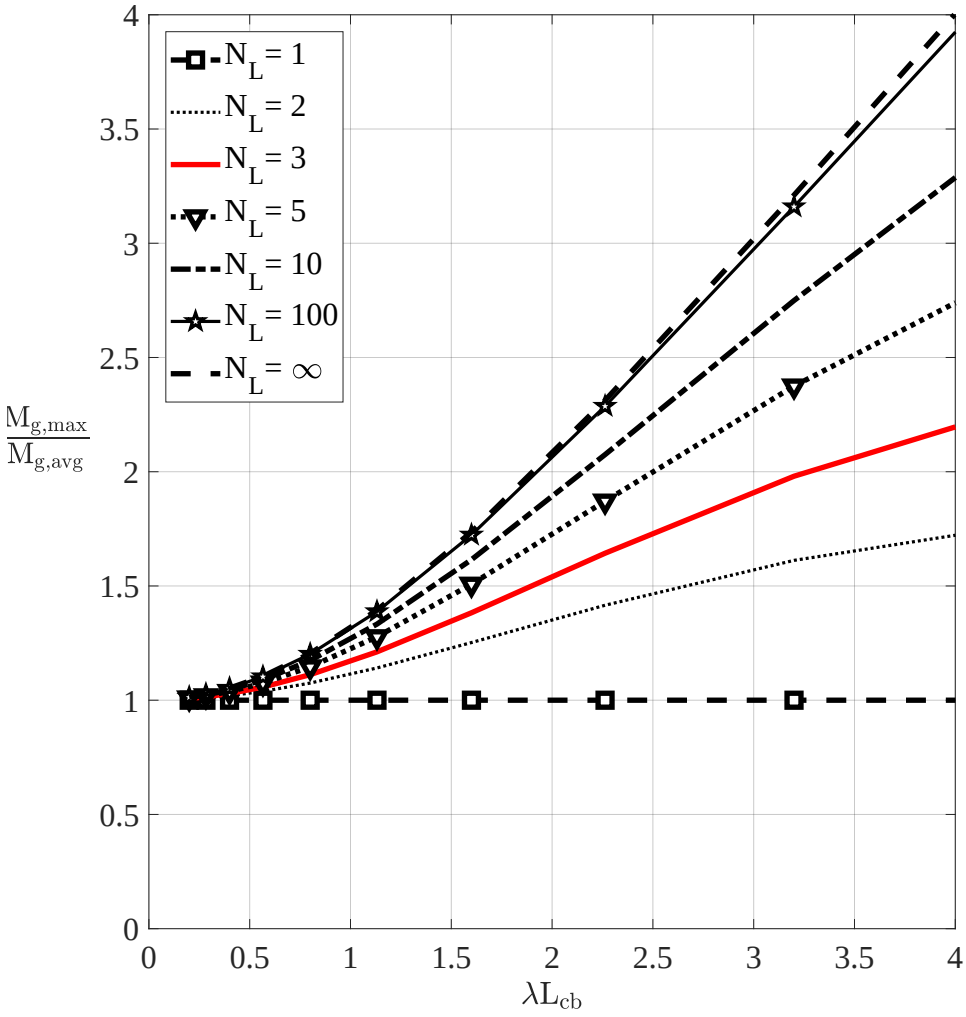

Figure 5.7: Girder Moment Distribution with Varying Stiffness Ratio for Different Number of Girder Lines, No REO

5.5 Effect of Cracking

When a vertical crack forms at the end of the girder (at the girder-diaphragm interface) and the extended strands start to work, the girder stiffness will be reduced significantly -it would be approximately 6.9% of its uncracked value for a girder with 10 extended strands. The (fully) cracked cap beam torsional stiffness was assumed to be 5% of its uncracked stiffness as Priestley et al. (1996) recommend that value unless detailed torsional stiffness calculations are done (Priestley et al., 1996).

The effect of the cracking of the cap beam and girders, separately and together, on the

uniformity of girder moments is illustrated in Figure 5.8 using the ABAQUS Model results, considering the reference structure. As the other models agree closely with the ABAQUS one, their results are not shown.

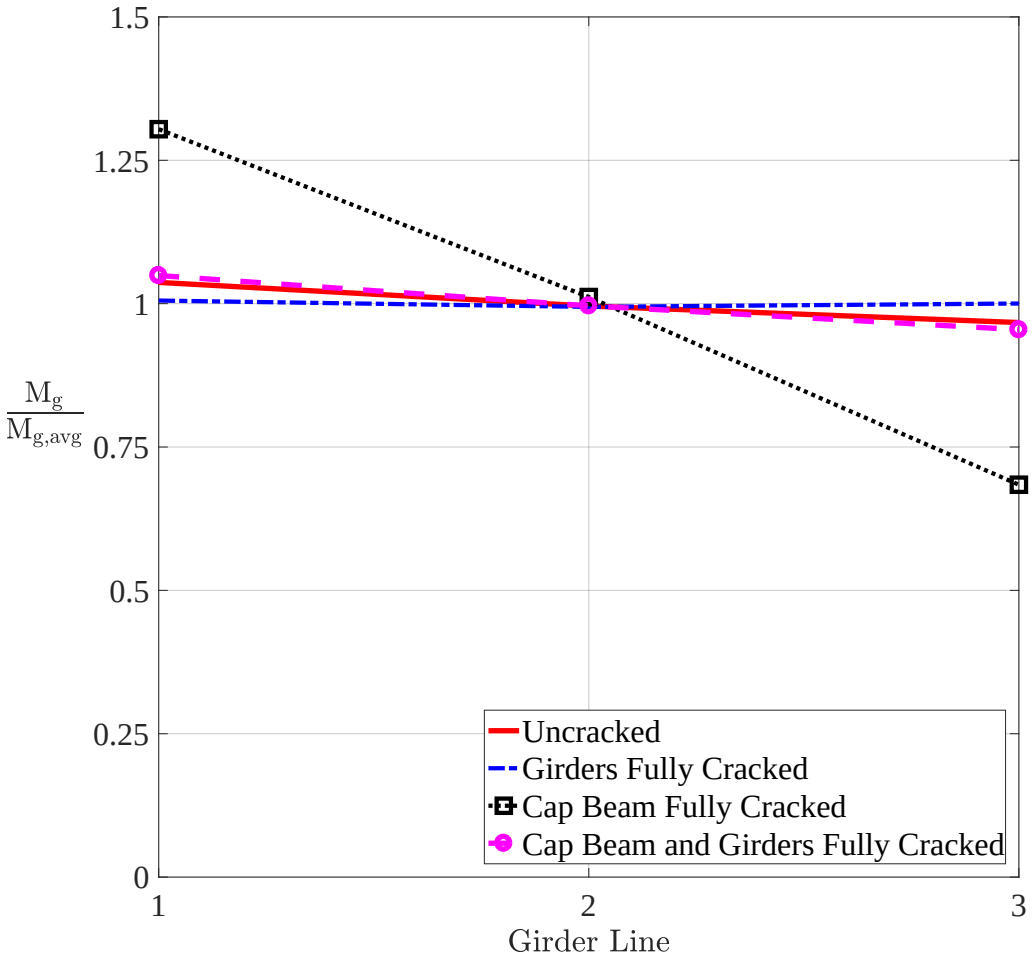

Figure 5.8: Variation in Girder Moment Ratio Along Cap Beam for the Effect of Component Cracking

To observe the effect of varying girder to cap beam stiffness ratios on the girder moment distribution, several cases were investigated. Progressively decreasing girder stiffnesses, ranging between 100% (uncracked) and 6.9% (fully cracked) were considered separately from progressively decreasing cap beam stiffnesses, ranging between 100% and 5%. The changes to the stiffnesses were applied by changing the modulus of elasticity, E, for each bridge component. Finally, a case, in which both the cap beam and the girders to be fully cracked, was

considered.

If all the girders are treated as cracked, or the cap beam is cracked along its entire length, these changes can be represented by a change in the stiffness ratio, λL_{cb}. However, if only some of the girders crack, or if the cap beam cracks along only part of its length, λL_{cb} can no longer be used as the controlling parameter.

As it can be seen in Figure 5.8, if only the girders are fully cracked, i.e. a low λL_{cb}, then all girder moments will be almost identical and the most uniform girder moment distribution is observed. Furthermore, the effect of severe cracking of the cap beam with little to no cracking in the girders, i.e. a high λL_{cb}, leads to the most non-uniform distribution of girder moments. In such a case, much larger moments are acting on girders in close proximity to the pier (within its effective width) and much smaller moments act on the edge girders. Finally, the girder moment distribution is almost equivalent (and fairly uniform) in the cases where nothing is cracked and when both the cap beam and girders are fully cracked. The same trend can be observed from Figure 5.4; namely, that for small values of λL_{cb}, which would represent a small ratio of the girder bending stiffness to the cap beam torsional stiffness, the moment distribution between girders is almost uniform.

Similarly, for large values of λL_{cb}, which represent a low ratio of the girder to cap beam stiffness and would occur when the only the cap beam is cracked, the girder moment distribution is less and less uniform. Presumably, in reality, the highest $\frac{M_{g,max}}{M_{g,avg}}$ ratio would be observed for a completely cracked cap beam and uncracked girders. Theoretically, the largest value of $\frac{M_{g,max}}{M_{g,avg}}$ would have would be the number of girder lines, N_L. This is unlikely to be observed in reality, as the value of λL_{cb} needs to be very large, namely at least 60 for 3 girder lines (the reference structure) in order for $\frac{M_{g,max}}{M_{g,avg}}$ to converge to $N_L = 3$. That means the total girder bending stiffness to cap beam torsional stiffness ratio needs to be 3600, which is deemed unlikely.

For reference, if the cap beam is completely cracked (down to 5% of its uncracked torsional stiffness), and the girders are uncracked, λL_{cb} is less than 2, including rigid offsets. Excluding the rigid offsets, λL_{cb} was determined to be approximately 3.

Finally, if the strands extended from the girders are yielding, that would be equivalent to considering the variation in moments for a low value of λL_{cb}, thus leading to a more uniform girder moment distribution.

Looking at the girder moment variations in all models, it could be concluded that the results of the UCSD tests involved a system with a torsionally very weak cap beam (even though it was PT), which cracked extensively, while the girders remained almost at full capacity (that is what their moment distribution, as well as photos of the post-test suggest), thus leading to the conclusion of ⅔ - ⅓ moment distribution. That distribution is not representative of the behaviour of bridges in Washington State, which predominantly use the "drop cap" (two-stage cap beam) bent system.

5.6 Likelihood of Cracking

For all the models discussed, the effect of cracking was considered by progressively increasing the degree of cracking in the cap beam and the girders, both individually and concurrently. This section discusses the likelihood and extent of cracking of these components.

5.6.1 Cap Beam Cracking

The shear stresses in the cap beam caused by the torsional moment, acting at the center of gravity of the superstructure, were investigated in the ABAQUS model with linear elastic material properties and uncracked section properties.

The portion of the structure where the shear stresses were checked is shown in Figure 5.9.

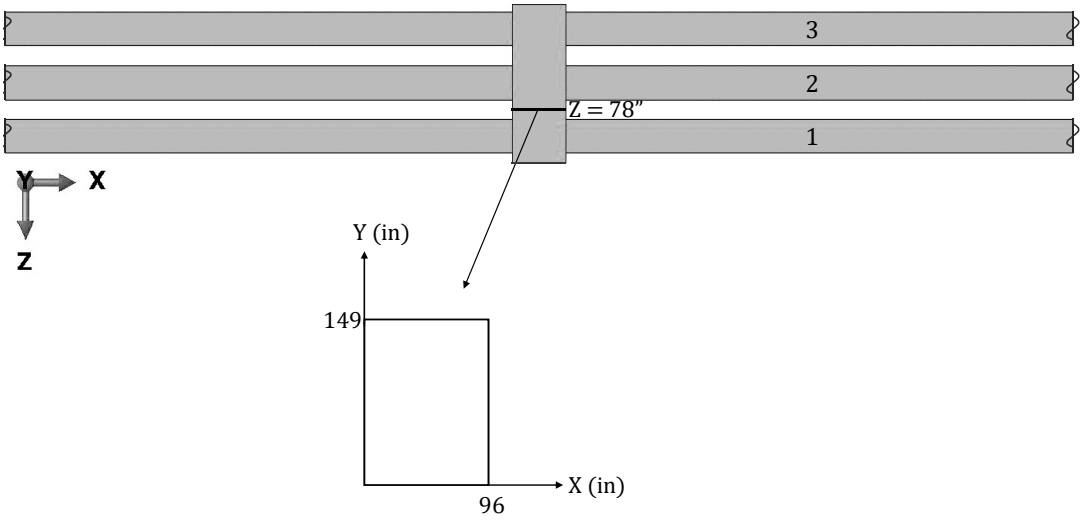

Figure 5.9: Cap Beam Location for Shear Stresses

The shear stresses in the cap beam between girder lines 1 and 2, namely at z=78”, are shown in Figure 5.10.

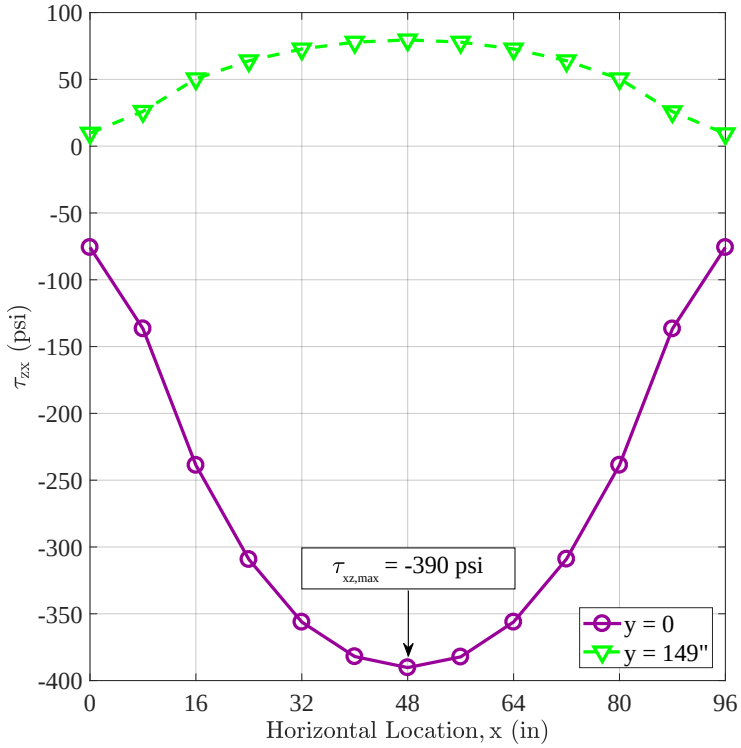

(a) Shear Stress, τ_{xz} vs Horizontal Location

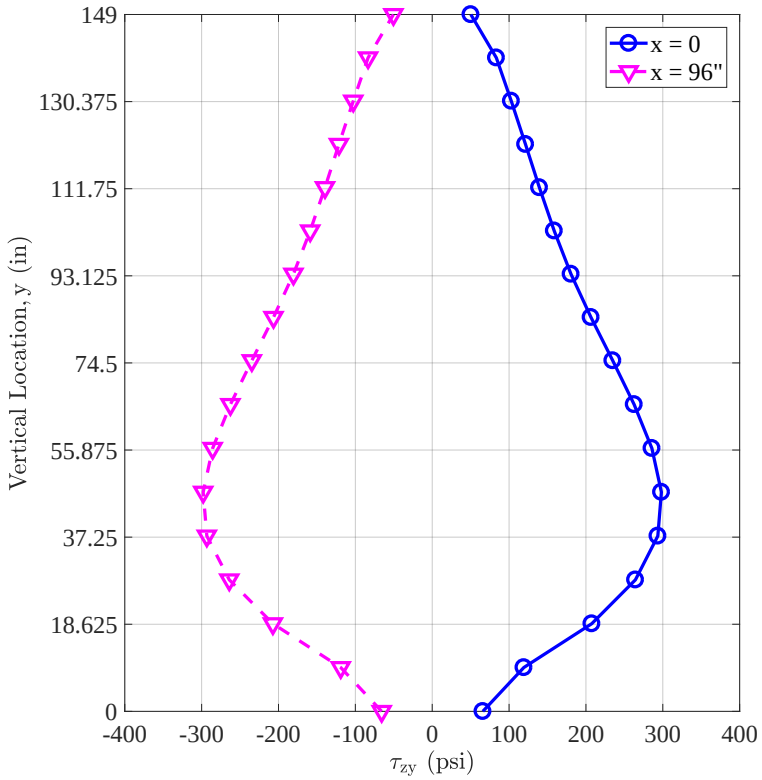

(b) Shear Stress, τ_{yz} vs Vertical Location

Figure 5.10: Cap Beam Shear Stress vs Location, z=78”

The maximum shear stress in the cap beam at z = 78”, namely the location between girder lines 1 and 2, shown in Figure 5.9, was τ_{max} = 390 psi and it was observed at the mid-bottom of the cap beam. The cap beam concrete, which uses the WSDOT 4000D mix, almost always has a 28-day compressive strength greater than 5000 psi. At the time of the earthquake, it is likely to be stronger still. If the cracking limit in shear is considered to be $4\sqrt{f'_c}$, for the cap beam this limit would be equal to 282 psi, considering an $f'_c = 5000$ psi.

Thus, the cap beam should be expected to crack adjacent to the column as it experiences shear stresses exceeding the cracking limit. The shear stresses in the cap beam between girder lines 2 and 3 were lower than or barely approaching the cracking limit of 282 psi. Therefore, the cap beam will not crack there.

These results were checked against the stick model maximum shear stress as follows.

(Stanton, 2002) offers an expression, which can be used to determine the shear stress in

the middle of the short side in a rectangular section, caused by a torsional moment, with good accuracy (within 0.1%).

$$\tau_{M_t} = \frac{M_t}{\beta_s h_{cb} b_{cb}^2} \tag{5.3}$$

where

M_t is the torsional moment acting on the section, taken as the torsional moment acting on the superstructure between girder lines 1 and 2, namely $M_t = 109500\ k - in$,

$h_{cb} = 149$" and $b_{cb} = 96$" are the larger and the smaller dimensions of the cap beam, respectively,

β_s is a dimensionless coefficient, function of $\frac{b_{cb}}{h_{cb}}$ and it is determined by Equation 5.4 (Stanton, 2002).

$$\beta_s = \frac{1}{3\left[0.742454 + \frac{b_{cb}}{h_{cb}}\left(0.5 + 0.375\frac{b_{cb}}{h_{cb}}\right)\right]} \tag{5.4}$$

$$\beta_s = 0.273$$

The maximum shear stress in a rectangular section would typically be observed in the middle of the long side of the section. However, this is expected to occur under the impact of pure torsion. Here, there are also shear forces acting on the cap beam, both from the girders and the column. Upon investigation, it was determined that the total shear force applied by the girders is much smaller, when compared to the column shear force. Thus, the maximum shear stress, observed in the cap beam would occur in its mid-bottom (at x=48" and y=0), where the effects of torsional moment and column shear force coincide. This can be seen from the ABAQUS results in Figure 5.10 as τ_{max} is τ_{xz}.

$$\tau_{M_t} = \frac{109500}{(0.273)(149)(96)^2} \tag{5.5}$$

$$\tau_{M_t} = 0.292\ ksi$$

The maximum transverse shear stress caused by the impact of a shear force can be

determined as shown in Equation 5.6 (Hibbeler, 2011).

$$\tau_{V,max} = \frac{3}{2}\frac{V_{cb}}{A_{cb}} \tag{5.6}$$

where

V_{cb} is the shear force acting on half of the cap beam from the column, $V_{cb} = 555\ kips$,

A_{cb} is the cross-sectional area of the cap beam, calculated as follows

$$\begin{aligned} A_{cb} &= h_{cb}b_{cb} \\ A_{cb} &= 149(96) \\ A_{cb} &= 14300\ in^2 \end{aligned} \tag{5.7}$$

Thus,

$$\begin{aligned} \tau_{V,max} &= \frac{3}{2}\frac{555}{14300} \\ \tau_{V,max} &= 0.058\ ksi \end{aligned} \tag{5.8}$$

So, the total shear stress due to the impact of the torsional moment and the shear force is

$$\tau_{max} = 0.058 + 0.292 = 0.350\ ksi = 350\ psi \tag{5.9}$$

This result is within 10% of the ABAQUS results.

5.6.2 Girder Cracking

The girders' cracked stiffness as well as their likelihood of cracking is checked next.

Considering the torsional moment at the centroid of the superstructure to be $M_{p,cg} = 27420\ k-ft$, based on the column plastic moment capacity, and the geometry of the reference bridge superstructure, the total moment transferred to the girders in flexure along half of the bridge width would be

$$M_{g,tot} = \frac{M_{p,cg}}{2} = 13710\ k - ft \tag{5.10}$$

Assuming the distance between the resultant compressive force and the centroid of the extended strands as $d = h_{girder} - 2" = 6'$, the total tensile force in the strands would be

$$\begin{aligned} T_{s,total} &= \frac{M_{g,tot}}{d} \\ T_{s,total} &= 2285\ kips \end{aligned} \tag{5.11}$$

Considering the yield stress for a Grade 270 0.6" diameter strand to be $f_{ps} = 243\ ksi$, the force at a single strand at yield would be

$$\begin{aligned} T_{ps} &= A_p f_{ps} \\ T_{ps} &= 52.73\ kips \end{aligned} \tag{5.12}$$

where A_p is the cross-sectional area of a 0.6" diameter strand (in^2).

Thus, the required total number of extended strands for half width of the bridge (6 girders) is

$$\begin{aligned} N_{ps} &= \frac{T_{s,total}}{T_{ps}} \\ N_{ps} &= 43 \end{aligned} \tag{5.13}$$

Based on the results presented in the previous sections, it is reasonable to assume a uniform girder moment distribution, thus extending the same number of strands from each girder. Thus, 7.2 strands need to be extended from each girder. Since the number of extended strands needs to be an even integer, 8 extended strands will be assumed per girder.

In order to determine the cracked stiffness of the girders, only the extended strand contribution was considered. The extended strands were assumed to debond after a length of L'_d, decaying from the strand stress at the nominal girder strength, $f_{ps} = 243\ ksi$, at its end embedded in the cap beam, to the effective presstress in the strands, $f_{pe} = 150\ ksi$, past the debonding length. This is in accordance with Section 12.9 of ACI 318-11, which discusses the development length requirements for prestressing strands.

$$L'_d = \frac{f_{ps} - f_{pe}}{1\ ksi} d_b \tag{5.14}$$

where d_b is the nominal strand diameter, which is 0.6".

Thus $L'_d = 55.8$". The axial stiffness of the extended strand over the debonding length is as follows.

$$k_{ps} = \frac{E_p A_p}{L'_d} = 110.8\ k/in \tag{5.15}$$

where $E_p = 28500\ ksi$ is the elastic modulus of a prestressing strand.

Using a moment arm of d and the axial strand stiffness, the rotational stiffness of a fully cracked girder provided by the (8) extended strands alone can be calculated according to Equation 5.16.

$$\begin{aligned} k_\theta &= \frac{\text{moment}}{\text{unit rotation}} = \frac{N_{ps} E_p A_p d}{L'_d/d} \\ k_\theta &= 4597000\ kip - in/rad \end{aligned} \tag{5.16}$$

Comparing this approximate cracked girder stiffness to the uncracked girder stiffness, as shown in Equation 5.17.

$$\begin{aligned} k_g &= \frac{3 E_g I_g}{L_g} \\ k_g &= 13100000\ k - in/rad \end{aligned} \tag{5.17}$$

The stiffness reduction ratio is

$$\frac{k_\theta}{k_g} = 0.35 \tag{5.18}$$

leading to the conclusion that if a girder cracks, its stiffness will reduce to approximately 35% of its uncracked stiffness.

If the prestressing strands were to yield, their stiffnesses would decrease, and the distribution of girder end moments would become more uniform. This "self-correcting" feature of the behaviour provides a useful backup to cover any uncertainties in the elastic properties.

Assuming a service prestress of $f_{cs} = -1500\ psi$ at the extreme tension face, namely, the bottom of the girder, and considering the tensile stress in the concrete is limited to $6\sqrt{f'_c}$, and $f'_c = 7000\ psi$ for a girder, the cracking moment is

$$M_{g,cr} = f_r S_{g,1} \tag{5.19}$$

where f_r is the modulus of rupture, determined as follows.

$$\begin{aligned} f_r &= 6\sqrt{f'_c} - f_{cs} \\ f_r &= 2002\ psi \end{aligned} \tag{5.20}$$

and $S_{g,1}$ is the girder bottom section modulus, determined as shown in Equation 5.21.

$$\begin{aligned} S_{g,1} &= \frac{I_g}{y_{cg}} \\ S_{g,1} &= 24240\ in^3 \end{aligned} \tag{5.21}$$

where y_{cg} is the girder center of gravity, measured from the bottom

Thus,

$$M_{g,cr} = 4045\ k - ft \tag{5.22}$$

As such, it can be concluded that the girders are unlikely to crack, since the girder cracking moment is greater than the predicted bending moment in each girder.

Upon investigating the ABAQUS model with uncracked section properties, the maximum axial stress in the girders was determined as 1.8 ksi in tension. However, since the effect of prestressing was not considered, the stress at the extreme tension face expected to occur in reality is expected to be much lower. The prestressing will cause significant pre-compression in the bottom girder flange, counteracting all or some of the tension caused by seismic bending. The exact value will depend on the prestressing details in the end of the girder.

The use of linear elastic material properties for the bridge superstructure was deemed appropriate, as it was thought that the cap beam is very stiff torsionally and would likely experience little cracking, namely it is expected to crack only in certain regions, i.e. close to the pier. The girders are also unlikely to crack and thus the use of a linear elastic material model does not compromise the results. Furthermore, the effect of the extent of cracking of the cap beam and the girders on the girder moment distribution was already investigated for the sake of completion.

The effects of partial cracking of bridge components (girders and cap beam), nonlinear geometry and material properties (i.e. by explicitly modeling the prestressing strands and reinforcement in the concrete and by not using a linear elastic properties to define materials), as well as considering the impact of other factors, such as a skew of a bridge should be investigated in more depth. However, it is thought none of these factors would drastically impact the conclusions drawn from the work presented in this thesis.

5.7 Comparison with UCSD Configuration

Since the majority of design manuals are based on the findings of Holombo et.al from the UCSD tests, a comparison between a typical bent cap system used in the state of Washington and the UCSD test prototype is presented by utilizing the continuous model as shown in Figure 5.11.

The continuous model curves for three and two girder lines along half of the bridge width were plotted for the WSDOT and UCSD superstructures, respectively. Linear elastic material properties and uncracked sectional properties were considered. The material properties and component dimensions for the UCSD bridge model were obtained from Holombo's Ph.D. dissertation (Holombo, 1999).

As can be seen in Figure 5.11, the distribution of girder end moments across the bridge deck is much more uniform for the WSDOT bent cap system.

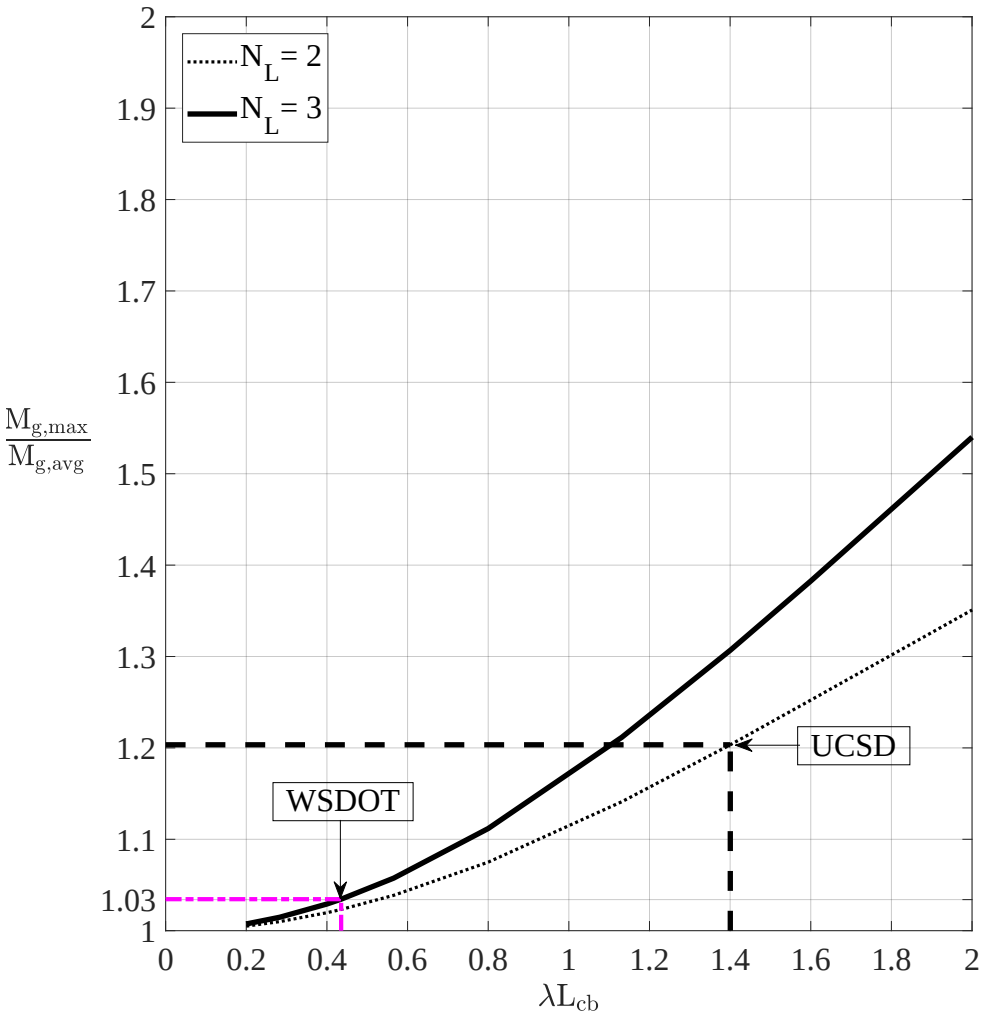

Figure 5.11: UCSD vs WSDOT Girder Moment Distribution

Similarly, Figure 5.12 shows a comparison of the deformed shapes for both typical Washington and California State bent cap systems. Washington bridges have much deeper cap beams, typically about 12' deep, which makes them considerably more stiff in torsion than California bridges.

The girder end rotations and consequentially, bending moments, are much more uniform for a Washington State bridge bent.

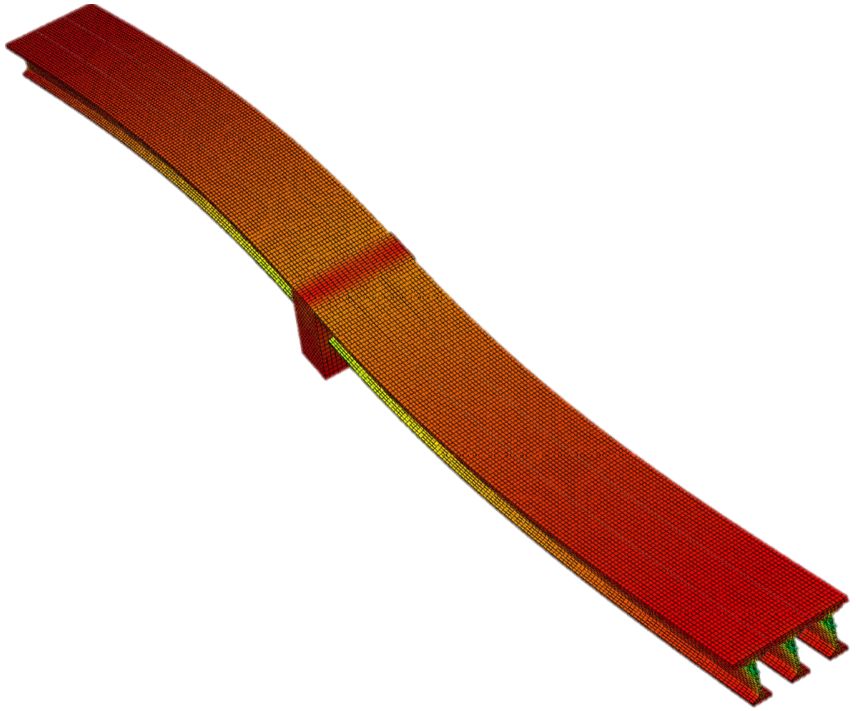

(a) Washington

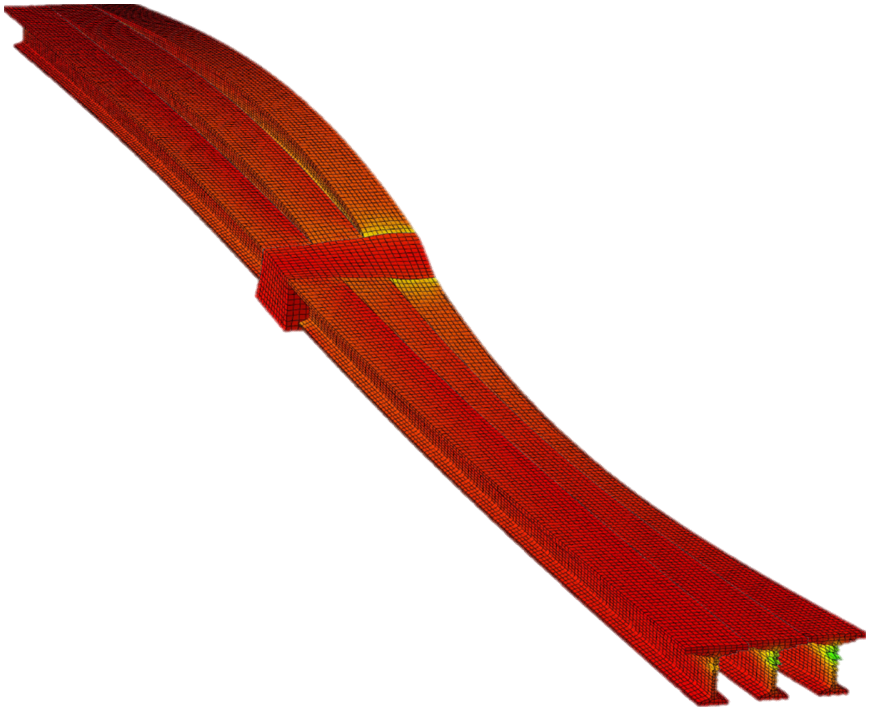

(b) California

Figure 5.12: Bridge Bent Deformed Shapes

The effect of partial cracking of the cap beam was investigated with ABAQUS software by cracking a portion of the cap beam between the first pair of girder lines, adjacent to the column (girder lines 1 and 2 in Figure 5.9). The cracked cap beam stiffness was considered as 5% of the uncracked stiffness. The shear stress (τ_{yz}) contours for Washington and California bridge bents are shown in Figure 5.13.

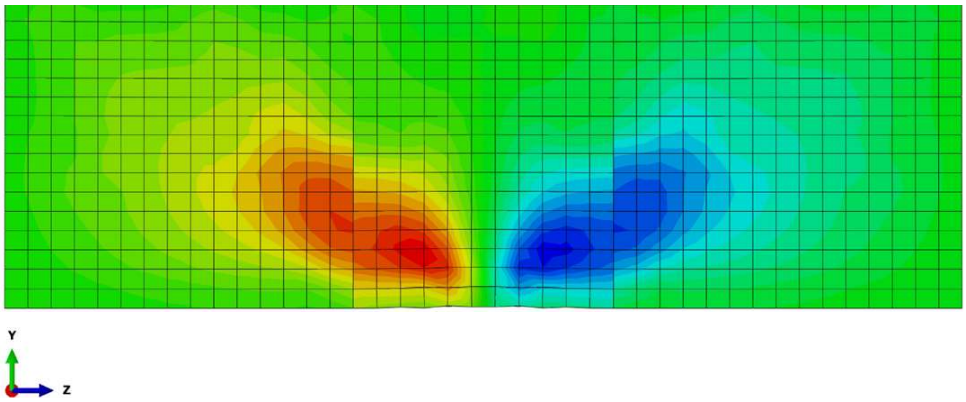

(a) Washington

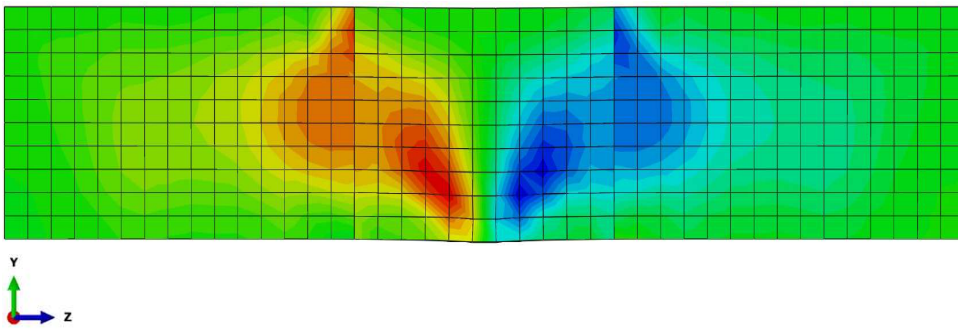

(b) California

Figure 5.13: Shear Stress Contours for Partially Cracked Cap Beams

For a Washington State bent cap system, regions of high, concentrated stresses developed where the column frames into the cross beam and propagated outward, significantly decreasing in magnitude by the time the diaphragm region was reached. Thus, the girders located in the cracked region, where the cap beam stiffness is low and shear stresses were small, experienced smaller bending moments, compared to exterior girders.

For a California bent cap system, since the crossbeam is considerably less deep, the stresses remain more concentrated and cannot dissipate in the manner, resulting in much

higher shear stresses in the cracked cap beam region, causing significantly larger bending moments in the girders in closest proximity to the column.

The girder bending moment distribution for partially cracked bridge bents is shown in Figure 5.14.

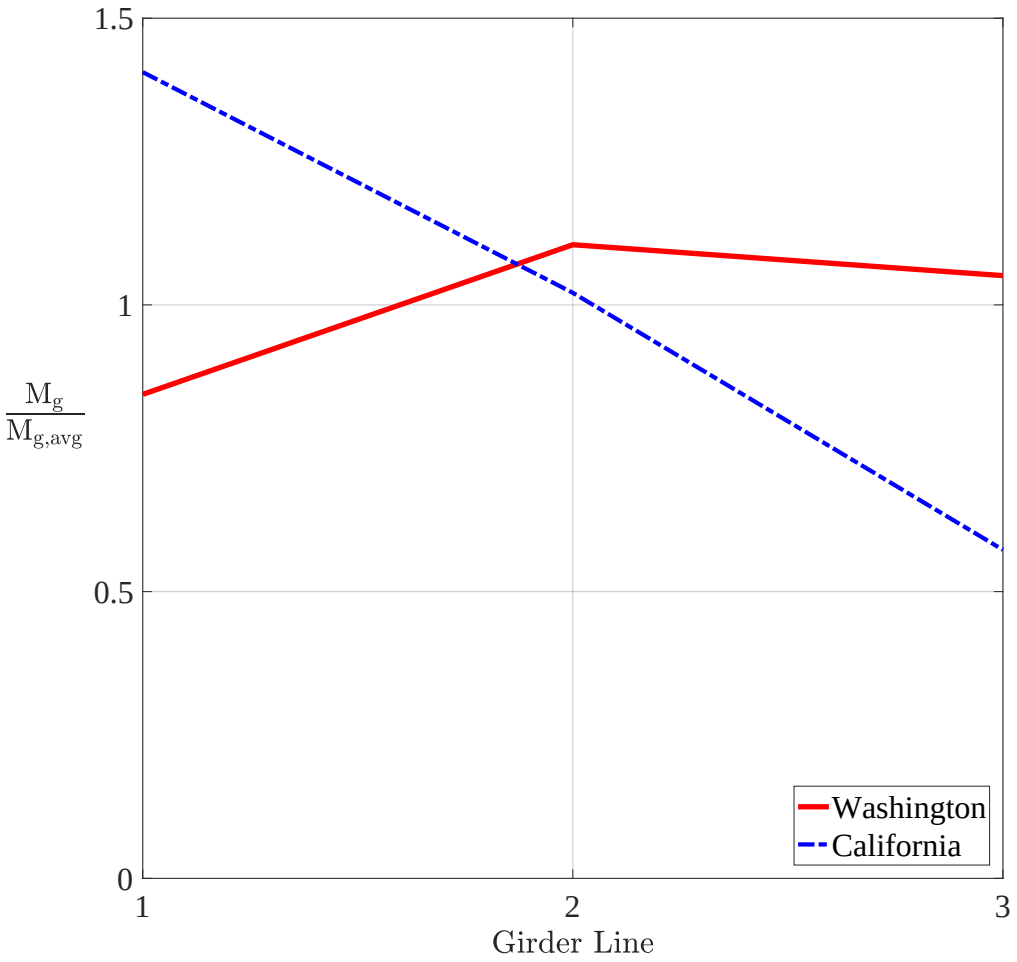

Figure 5.14: Girder Moment Distribution for Partially Cracked Bent Caps

Looking at the results for a typical bent cap system in the state of Washington, as summarized in Figures 5.12 to 5.14, it can be concluded that girder moment uniformity is not significantly compromised by partial cap beam cracking. In contrast, a much less uniform distribution of girder moments is observed for a typical California cap beam system.

5.8 Conclusions

Current practice is based on the assumption that the major (2/3) portion of the seismic moment (due to longitudinal seismic load), acting at the center of gravity of the bridge superstructure, will be resisted by the girders closest to the column. This practice is overly conservative for bents with two-stage "drop" cap beams and consequentially, a lot more strands are required to develop the girder-diaphragm connections, while complicating the practical implementation of the connection detail.

The study described in this chapter has concluded that since a two-stage bent cap system is used in the state of Washington, the cap beam is torsionally stiff and strong enough to justify girder bending moment distribution that is much more uniform than that included in the AASHTO LRFD Specifications (AASHTO, 2012). The moment distribution between girders is controlled by two dimensionless parameters: λL_{cb} and N_L, where N_L is the number of girder lines along half of the bridge width, and λL_{cb} is the ratio of the flexural stiffness of all the girders to the torsional stiffness of the half cap beam, $\sqrt{\frac{K_g}{K_{cb}}}$. As it can be concluded from the analyses described in this chapter, for uncracked and fully cracked bridge components, the girder bending moment distribution is almost identical. Thus, the same number of strands, which is going to be smaller than current practice, can be extended from each girder. In no case, with the exception of a severely cracked cap beam and barely cracked girders, was a girder moment distribution justifying the $2/3M_p$ (interior) - $1/3M_p$ (exterior) rule, observed. It is concluded that the UCSD test results were derived for a system with a very different stiffness ratio to that used in Washington bridges, leading to a distribution of girder moments that is unrealistically non-uniform. Furthermore, the basis for deciding the measured distribution of girder moments, namely the strains in the longitudinal reinforcement of the deck, is questionable.

As a result of all of the analyses, it is claimed that all girder-diapghragm connections for a particular bridge can be developed with the same, smaller number of strands, compared to current practice. This is a significant benefit in terms of constructablilty, especially in

curved bridges. It would also improve the block pullout strength of the connection, as less strands with a large embedment distance would be used. Finally, cost would be reduced.

The proposed girder-diaphragm connection design procedure differs from the present design guidelines (AASHTO, 2012), primarily since Washington state cap beams are much stiffer and stronger in torsion, when compared to the ones in California and the ones used in the UCSD tests, which the current design practice is based on.

Chapter 6

IMPLEMENTATION

A successfully designed bridge bent system must have sufficient strength and ductility in order to provide satisfactory longitudinal seismic resistance. In order to achieve these requirements, the principles of Capacity Design must be invoked. The column is usually designated as the yielding element, and the strength of adjoining elements is determined by the need to capacity protect them.

The strength of the column, and therefore the load on the adjoining elements, are subject to some uncertainties. The primary ones are the strength of the reinforcing bars, the longitudinal reinforcement ratio, and the magnitude of the axial load. Considering all reinforcement conforms to the ASTM A 706 standard specifications (ASTM, 2016), the expected value of the yield stress of the longitudinal column reinforcement was taken as the average of the maximum permitted yield stress ($f_{y,max} = 78$ ksi) and the minimum yield stress ($f_{y,min} = 60$ ksi), namely, as $f_{y,expected} = 69$ ksi. For the column of the reference structure, a 15% increase in the yield stress from the minimum to the expected value was found to cause an approximately 7% increase in the nominal column moment capacity, M_n. Moreover, increasing the axial load, P_n by 10% increases the column nominal moment capacity M_n by about 2%. The increase in moment capacity due to these two factors is accounted for within the factor of 1.2 required by AASHTO and applied on the nominal moment capacity, M_n, in order to obtain the plastic moment capacity, M_p.

The possible failure mechanism of the girders was investigated by considering the effects of the factors contributing to the girders' resistance against pulling out of the diaphragm, as described below.

The properties of the prototype bridge model were used when performing detailed calculations.

The elements resisting girder failure were considered as interface shear stresses between the faces of the girder and the surrounding diaphragm concrete, pullout of the reinforcing bars, projecting from the end of the girder, failure of extended strands, and girder cracking. Each of these is considered in detail in this chapter.

6.1 Girder-Diaphragm Interface Shear Resistance

The shear resistance of the girder-diaphragm interface for each girder was considered as described in AASHTO LRFD Bridge Design Specifications (AASHTO, 2012).

The nominal interface resistance, V_{ni}, was determined as follows.

$$V_{ni} = cA_{cv} + \mu(A_{vf}f_y + P_c) \tag{6.1}$$

in which:

$A_{cv} = b_{vi}L_{vi}$ is the interface area,

where

b_{vi} is the interface width considered to be engaged in shear transfer (in),

L_{vi} is the interface length considered to be engaged in shear transfer (in),

c is the cohesion factor of the interface (ksi),

μ is the friction coefficient,

A_{vf} is the interface shear reinforcement within the interface area A_{cv} (in^2),

f_y is the design yield stress of the interface reinforcement (ksi),

and

P_c is the permanent net compressive force normal to the shear plane ($kips$); if force is tensile, $P_c = 0$.

The component of the interface shear resistance, consisting of the net normal clamping force, $A_{vf}f_y + P_c$, is zero for the reference bridge.

Since WF74G girders, embedded into the diaphragm 14.5" were considered for the prototype structure,

$L_{vi} = 198.92$"

$b_{vi} = 14.5$"

Consequently,

$A_{cv} = 28884.40\ in^2$

The cohesion factor, c, is determined as specified in Chapter 5 Article 5.7.4.4 in AASHTO LRFD Bridge Design Specifications, considering concrete placed against a clean concrete surface, free of laitance, but not intentionally roughened,

$$c = 0.075\ ksi$$

Thus, from Equation 6.1,

$$V_{ni} = 216.33\ kips \tag{6.2}$$

The net interface shear resistance, V_{ni} was determined to act at a distance of 49.1" from the top of the girder as an average value weighted by girder side length, excluding the girder top flange. Thus, the positive moment resistance provided by the impact of interface shear was determined as

$$M_{n,i} = 10,620\ k - in \tag{6.3}$$

The selected value of 75 psi for the cohesion factor may be a conservative estimate for the shear stress. The diaphragm concrete is cast some months after the girder, so differential shrinkage will, if anything, add compression force across the interface, leading to additional frictional forces.

6.2 Bar Pullout

According to typical WSDOT drawings for WF74G girders, 7 No. 7 bars are embedded into each girder web for 10'-6" ($25d_b$) and extended into the diaphragm for 1'-10"; and 4 No. 6 bars are embedded 6'-0" into the girder bottom flange and extended into the diaphragm for 1'-6" ($24d_b$).

The provisions in Chapter 12 in ACI 318-11 were used to determine the required development length for a No. 6 and No. 7 bars, in order to check whether the reinforcing bars extending from the girder into the diaphragm will pull out of the girder before they yield.

The development length for a reinforcing bar was determined by using Equation 6.4 (ACI318, 2011).

$$l_d = \left(\frac{3}{40} \frac{f_y}{\sqrt{f'_c}} \frac{\Psi_t \Psi_e \Psi_s}{\left(\frac{c_b + K_{tr}}{d_b} \right)} \right) d_b \tag{6.4}$$

where

f_y is the yield stress of the reinforcing bars (psi),

f'_c is the specified compressive stress of the concrete (psi),

Ψ_t is a factor used to modify development length based on reinforcement location,

Ψ_e is a factor used to modify development length based on reinforcement coating,

Ψ_s is a factor used to modify development length based on reinforcement size,

d_b is the reinforcement diameter (in),

$\frac{c_b + K_{tr}}{d_b}$ is a term accounting for confinement.

For uncoated reinforcement, $\Psi_e = 1.0$. For No. 6 deformed bars and smaller, the required development length can be reduced by 20%, using a $\Psi_s = 0.8$.

Since the diaphragm region, which the bars are embedded in, is very highly reinforced, it is assumed that maximum confinement will be provided, thus the term $\frac{c_b + K_{tr}}{d_b}$ is taken as 2.5 - the maximum permitted value in the code.

The required development length for a No. 7 bar was determined as follows.

$$\begin{aligned} l_d &= \left(\frac{3}{40}\frac{60,000}{\sqrt{5000}}\frac{(1.0)(1.0)(1.0)}{2.5}\right)0.875 \\ l_d &= 22.27\text{”} \end{aligned} \tag{6.5}$$

Whereas for a No. 6 bar,

$$\begin{aligned} l_d &= \left(\frac{3}{40}\frac{60,000}{\sqrt{5000}}\frac{(1.0)(1.0)(0.8)}{2.5}\right)0.75 \\ l_d &= 15.27\text{”} \end{aligned} \tag{6.6}$$

Thus, it is assumed that the controlling failure mode of the reinforcing bars will be yielding, rather than pullout. Using an Excel spreadsheet, considering the extended non-prestressed reinforcement at the girder ends, it was determined that when the girders are trying to breakout from the diaphragm, all of the extended reinforcing bars would be in tension and their tensile strain values would be quite high (ranging from 2% - 6%). As such, the total tension force provided by the reinforcement was determined to be 357.6 kips.

The bending moment resistance of the reinforcement was determined to be

$$M_{n,s} = 18,368\ kip - in \tag{6.7}$$

Upon investigation of Chapter 21 of ACI318-11, which addresses seismic design requirements, it was discovered that the required embedment length for straight bars with sizes from No. 3 through No. 11 under tension can be determined as follows.

If the depth of concrete cast in one lift beneath the bar does not exceed 12", the development length is $2.5\ell_{\mathrm{dh}}$; if the concrete cast in one lift beneath the bar exceeds 12", the development length is $3.25\ell_{\mathrm{dh}}$, where ℓ_{dh} is defined as follows.

$$\ell_{dh} = \frac{f_y d_b}{65\sqrt{f'_c}} \tag{6.8}$$

where

f_y is the yield stress of the reinforcing bars (psi),

d_b is the reinforcing bar diameter (in),

f'_c is the specified compressive strength of the concrete (psi).

Assuming the concrete cast in one lift was greater than 12", it was determined that the required embedment lengths for a No. 7 bar and a No. 6 bar are 37.12" and 31.82", respectively. Considering that No. 7 bars are embedded 22", an additional embedment of 15" would be required to develop the bars in tension. Similarly, No. 6 bars are embedded for 18", and 14" of additional embedment are required to develop the bars in tension.

According to the provisions in Chapter 12 in ACI318-11, sufficient embedment length is provided in each case; however, the seismic provisions in Chapter 21 require more than the provided embedment depth for the development of the extended reinforcing bars in tension. Thus, for the current detail, the extended reinforcing bars cannot be counted on to provide additional resistance to girder pullout in the same way as extended girder strands equipped with anchors.

6.3 Failure of Extended Strands

Each girder in the reference bridge includes 8 Grade 270 0.6" diameter extended strands, located 2" from the bottom face of the girder and embedded into the diaphragm for 1'-9" with a strand vice and a plate on the end. The extended strands will contribute to preventing pullout of the girder from the diaphragm. The Concrete Capacity Design (CCD) model, which was previously determined to accurately predict the required embedment depth to achieve a ductile failure of strands anchored with barrel anchors, was used to check the failure mode of the extended strand detail, as well as to estimate the resistance the extended strands would provide to the girders pulling out of the diaphragm. The CCD model was described in detail in Chapter 3.

The concrete cone failure load of the 8 strands with barrel anchors was determined according to equation Equation 6.9 (Fuchs et al., 1995).

$$N_n = \frac{A_N}{A_{No}} \Psi_2 \, k_{nc} \sqrt{f'_c} \, h_{ef}^{1.5} \tag{6.9}$$

where

h_{ef} is the effective embedment depth of the anchor (in),

A_{No} is the projected area of a single anchor at the concrete surface (in^2),

A_N is the actual projected area at the concrete surface (in^2),

k_{nc} is a calibration factor,

Ψ_2 is a factor accounting for edge effects,

f'_c is the specified concrete compressive strength (psi).

Edge effects will not have an impact, thus $\Psi_2 = 1.0$.

$k_{nc} = 40$ for cast-in-place anchors.

The projected area of a single anchor is determined idealizing the failure cone as a pyramid with base length of $3h_{ef}$. Thus,

$$A_{No} = 9h_{ef}^2 = 9(21^2) = 3969\ in^2 \tag{6.10}$$

The actual projected area at the concrete surface is determined by considering the effect of the spacing between the anchored extended strands.

$$A_N = (3h_{ef})(3h_{ef} + 28.5) = 3(21)(3(21) + 28.5) = 5764.5\ in^2 \tag{6.11}$$

From Equation 6.9,

$$\begin{aligned} N_n &= \frac{5764.5}{3969}(1.0)(40)\frac{\sqrt{5000}}{1000}\left(21^{1.5}\right) \\ N_n &= 395.33\ kips \end{aligned} \tag{6.12}$$

This corresponds to a strand stress of 228 ksi. Assuming an ultimate strand stress of 267 ksi, corresponding to a fracture load of 58 kips, the tensile load capacity of the 8 extended strands would be about 464 kips. As it can be seen, this exceeds the CCD prediction for a concrete breakout. Thus, it is assumed that the failure mechanism of the extended strands would be the breakout of the concrete surrounding them. Regardless, the strands still provide a resistance to the girders trying to pull out of the diaphragm prior to the breakout of the concrete. The moment resistance provided by the extended strands is

$$M_{n,p} = 28,465\ k - in \tag{6.13}$$

6.4 Girder Cracking

The likelihood of the girder cracking at the girder-diaphragm interface was investigated by determining the positive bending moment that would generate tensile stresses in the bottom girder flange equal to the cracking stresses. The girders in the reference structure are reinforced with 42 straight and 22 harped 0.6" diameter strands. At the end of the girder, the centroid of the straight strands is located 3¾" from the bottom face of the girder, while the centroid of the harped strands is located 1'-2" from the top face of the girder. The 22 strands are harped at $0.4L_{span}$ and $0.6L_{span}$.

The effective stress of the strands is assumed as $f_{pe} = 160\ ksi$. Then, the transfer length, l_t can be determined as follows.

$$l_t = \frac{f_{pe}}{3} d_b = \frac{160}{3} 0.6 = 32" \tag{6.14}$$

Considering the girders are embedded 14.5" into the diaphragm, the strands, which are located 14.5" from the girder end, namely less than the transfer length, will have a stress less than the effective stress. Assuming a linear variation from zero stress to f_{pe}, the stress in the strands would be 72.5 ksi.

The stress at the extreme bottom fiber of the girder due to prestressing and self weight can be determined as follows.

$$f_1 = -\frac{F_p}{A} - \frac{F_p e_p}{S_{g,1}} + \frac{M_{sw}}{S_{g,1}} \tag{6.15}$$

where

$F_p = A_p f_p$ is the force in the prestressing strands ($kips$),

A is the cross-sectional area of a WF74G girder (in^2),

and

A_p is the area of prestressing steel (in^2),

f_p is the stress in the prestressing steel (ksi),

e_p is the distance from the centroid of the WF74G section to the centroid of the prestressing

strands (in),

$S_{g,1}$ is the bottom section modulus of the girder (in^3),

M_{sw} is the self weight moment at 14.5" from the girder end.

Thus,

$$f_1 = -\frac{64(0.217)(72.5)}{923.53} - \frac{42(0.217)(72.5)(31.907)}{20594.8} - \frac{22(0.217)(72.5)(-24.343)}{20594.8} + \frac{1151.58}{20594.8}$$
$$f_1 = -1.65\ ksi \tag{6.16}$$

Considering a cracking stress f_{cr},

$$f_{cr} = 7.5\frac{\sqrt{9200}}{1000}$$
$$f_{cr} = 0.72\ ksi \tag{6.17}$$

Thus, the cracking moment can be determined based on the maximum tension stress that can be applied before the girder cracks.

$$M_{cr} = (f_{cr} - f_1)\, S_{g,1}$$
$$M_{cr} = (0.72 - (-1.65))\, 20594.8 \tag{6.18}$$
$$M_{cr} = 48775\ k - in$$

As can be seen, the cracking girder moment is much greater than the maximum girder bending moment demand, which is expected to occur when the column has reached its plastic moment capacity. Thus, it can be concluded that the girders will not crack prior to the failure of the column.

6.5 Sequence of Failure Events

All of the factors contributing to the resistance of a girder pulling out from the diaphragm as well as the maximum girder moment demand, when the column has reached its plastic moment capacity, and the cracking girder moment are summarized as shown in Figure 6.1.

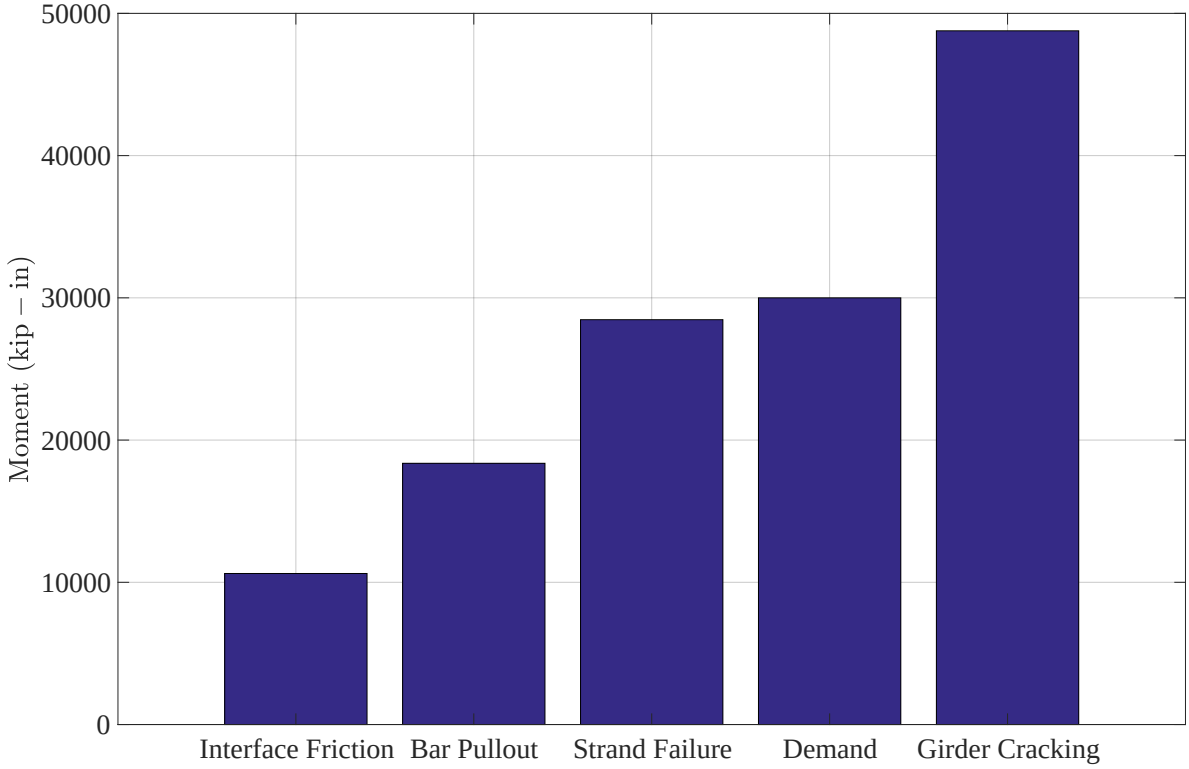

Figure 6.1: Girder Pullout Failure Sequence

The maximum girder moment demand was obtained from ABAQUS analysis results, discussed in Chapter 5. A similar girder moment demand is obtained considering the total plastic moment at the center of gravity of the superstructure is distributed evenly among girder lines. The interface friction, bar pullout and strand resistance are additive.

The interface shear girder-diaphragm resistance will be overcome first. After that, the girder will be relying on the extended bars and strands to resist it trying to pull out of the diaphragm. The collective moment resistance of the extended strands and bars was determined as 46,093 k-in, considering the impact of the portion of the top girder flange, which is in compression and reduces the moment capacity. This resistance is larger than the maximum girder bending moment of approximately 30,000 in-k, which is expected to occur when the column reaches its plastic moment capacity. The largest girder moment was determined to occur when a partially cracked cap beam and uncracked girders were considered. The cap beam region, contained within the first two girder lines was taken down

to 5% of its uncracked stiffness, while the rest of the cap beam was left uncracked.

If the girders remain uncracked and the cap beam is completely cracked (that is, the stiffness of the whole cap beam is down to 5% of its uncracked stiffness), then the maximum girder moment demand was found to be approximately 36,500 k-in. This value is still significantly smaller than the resistance provided by the extended bars and strands. This leads to the conclusion that fewer strands can be extended, such that the total resistance to girder pull out would be equal to the maximum girder moment demand. In that case, 4 extended strands, along with the extended reinforcing bars would be sufficient to provide a 34,000 in-k moment resistance, ensuring the girders will not pull out before the column has failed.

The bars extending from the girders into the diaphragm are currently considered to serve as reinforcement for shear friction for transverse seismic loading, and to resist pullout effects, arising in the girders due to creep. Thus, if the reinforcing bars, extended from the girder into the diaphragm, are not considered to contribute to girder pullout resistance during a seismic event, then 8 strands, with stresses $f_p = 260$ ksi were determined to provide resistance (of about 32,000 k-in), greater than the maximum girder moment demand, obtained from either analysis or the assumption that all girders will resist an equal portion of the seismic moment.

The girder cracking moment is much greater than the largest girder bending moment demand and thus the girders are not expected to crack by the time the column has reached its plastic moment capacity.

The sequence of events influences the distribution of girder moment demand. It is clear that the interface shear transfer fails first. If that is assumed to drop to zero because the resistance is brittle, the subsequent behaviour will depend on bar and strand yielding. That implies essentially zero stiffness for incremental loading, in which case the moment demand is uniform across all the girders and the same number of strands can be extended from each girder.

6.6 Design Guidelines

6.6.1 Design Procedure

Based on all of the findings in this thesis, the following design procedure is recommended:

1. Determine the plastic moment of the column, $M_p = 1.2M_n$, and the corresponding moment at the center of gravity of the superstructure. This is the total moment to be distributed among the girders (See WSDOT BDM Section 5.1.3 Equation 5.1.3-2 (WSDOT, 2015)).

2. Determine the value of λL_{cb} for the bent, and from it the ideal distribution of moment among the girders, using Table 6.1. For values of parameters not addressed in the table, the girder moments may be obtained using Equation 6.19.

$$M_{g,i} = T_o \frac{\sinh\left(\frac{\lambda L_{cb}}{2N_L}\right)}{\sinh(\lambda L_{cb})} \cosh\left\{\lambda L_{cb}\left(1 - \frac{i - 1/2}{N_L}\right)\right\} \tag{6.19}$$

where

i is girder line number,

$M_{g,i}$ is the bending moment in girder i caused by longitudinal seismic loading,

T_o is the maximum torque in the cap beam equal to half of the total seismic moment generated by a single column and acting at the center of gravity of the superstructure

L_{cb} is half of the cap beam length, for a single column bent; half of the column spacing for a multi-column bent,

N_L is the number of girder lines along half of the cap beam,

λL_{cb} is the ratio of total stiffness of all girders to the torsional stiffness of half the total length of the cap beam. For girders free to rotate, $\lambda L_{cb} = \sqrt{\left(\frac{3EI}{L}\right)_g \frac{2N_L}{(GJ/L)_{cb}}}$.

The term $3EI_g$ should be replaced by $4EI_g$ when the far end of the girder is fixed against rotation.

EI_g is the flexural stiffness of one girder, including composite deck,

L_g is the girder span length, if girders frame into the cap beam from only one side.
$L_g = \dfrac{2}{(1/L1 + 1/L2)}$ if girders frame into the cap beam from both sides,
where L_1 and L_2 are individual girder span lengths.

GJ_{cb} is the torsional stiffness of the cap beam cross-section.

2.1. For two-stage prismatic cap beams, the moment distribution is likely to be nearly uniform.

2.2. For flush cap beams, it is likely that λL_{cb} will be > 1.0 and the moment distribution will not be uniform.

2.3. For tapered cap beams, Table 6.1 (or Equation 6.19) may be used if the torsional stiffness is initially defined by the deepest section of the cap beam, and λL_{cb} is then increased by 20%. This will lead to a less uniform distribution of girder moments than that found with a prismatic cap beam.

3. Adjust the girder moments from their ideal values to a practical distribution that can be accommodated by an integral number of extended strands in each girder. The sum of the adjusted moments shall be at least as large as the sum of the ideal moments, and the adjustments should generally increase the moments in girders closer to the column. A slight downwards adjustment in an individual girder moment is acceptable, especially in a girder remote from the column.

4. Select strands and bars to develop the required moment resistance in each girder as follows.

4.1. Use strands extended from the bottom flange, rather than reinforcing bars, to the extent possible. *(Reasoning: The strands are located with the greatest lever arm and so are the most efficient way to resist moment. Strands are stronger than comparably sized rebar, so fewer are needed. Strands may be fully anchored within the cap beam with strand vices, at the horizontal location that is most advantageous for satisfactory joint performance. Strands are already well anchored in the girder, so no special anchorage requirements are needed there. Strands are more flexible in bending than rebar, so may more easily be moved in cases of conflict during construction.)*

4.2. Extend each strand as far as possible through the cap beam (e.g. to a point 6" inside the vertical diaphragm steel on the opposite face.) Anchor each strand with a strand vice that is fully seated prior to girder shipment.

4.3. The pattern of strands extended from opposing girders at a common cap beam should be chosen in such a way as to minimize the likelihood of conflicts.

4.4. To calculate the positive moment flexural resistance of the girder, assume that each strand is stressed to its yield stress (e.g. 243 ksi). *(Reasoning: by this means the elongation of the strand will be $< 1\%$, and the girder pullout from the cap beam will be < 1.0", when the column plastic capacity is reached. The strand will also pull the girder back to its original position, with no residual displacement, after an event.)*

4.5. If some of the rebar used in the present detail is retained, its contribution to the flexural strength should be counted in order to minimize the number of extended strands. *(This is not recommended: the web rebar is located so that it is anchored near the face of the cap beam, and may cause unnecessary joint shear stress or block pullout damage during an extreme event.)*

Table 6.1: Girder Moment Ratios as a Function of Stiffness Ratio λL_{cb}

λL_{cb}	$N_L = 2$		$N_L = 3$			$N_L = 4$			
	$\frac{M_{g,1}}{T_o}$	$\frac{M_{g,2}}{T_o}$	$\frac{M_{g,1}}{T_o}$	$\frac{M_{g,2}}{T_o}$	$\frac{M_{g,3}}{T_o}$	$\frac{M_{g,1}}{T_o}$	$\frac{M_{g,2}}{T_o}$	$\frac{M_{g,3}}{T_o}$	$\frac{M_{g,4}}{T_o}$
0	0.250	0.250	0.167	0.167	0.167	0.125	0.125	0.125	0.125
0.2	0.251	0.249	0.168	0.166	0.166	0.126	0.125	0.125	0.124
0.4	0.255	0.245	0.172	0.166	0.163	0.129	0.126	0.123	0.122
0.6	0.261	0.239	0.177	0.164	0.158	0.135	0.126	0.121	0.118
0.8	0.269	0.231	0.185	0.163	0.152	0.142	0.127	0.118	0.113
1	0.278	0.222	0.195	0.161	0.144	0.150	0.128	0.114	0.107
1.2	0.289	0.211	0.206	0.158	0.136	0.160	0.129	0.110	0.101
1.4	0.301	0.199	0.218	0.155	0.127	0.171	0.130	0.105	0.094
1.6	0.313	0.187	0.230	0.152	0.118	0.182	0.131	0.100	0.086
1.8	0.326	0.174	0.243	0.148	0.108	0.194	0.131	0.095	0.079
2	0.338	0.162	0.257	0.144	0.099	0.206	0.132	0.090	0.072
2.2	0.350	0.150	0.270	0.140	0.090	0.219	0.131	0.085	0.065
2.4	0.362	0.138	0.283	0.136	0.081	0.231	0.131	0.080	0.058
2.6	0.373	0.127	0.295	0.132	0.073	0.243	0.130	0.075	0.052
2.8	0.384	0.116	0.307	0.127	0.066	0.255	0.129	0.070	0.046
3	0.394	0.106	0.319	0.122	0.059	0.266	0.128	0.065	0.041
3.2	0.403	0.097	0.330	0.118	0.052	0.277	0.126	0.061	0.036
3.4	0.412	0.088	0.341	0.113	0.047	0.287	0.124	0.056	0.032
3.6	0.420	0.080	0.351	0.108	0.041	0.297	0.122	0.052	0.028
3.8	0.427	0.073	0.360	0.104	0.037	0.307	0.120	0.049	0.025
4	0.434	0.066	0.369	0.099	0.032	0.316	0.117	0.045	0.022

Note: The numbers 1, 2, 3 and 4 refer to the girder lines. Line 1 is closest to the column.

6.6.2 Design Example

A reference structure with a single column bent and 6 girder lines across the full bridge width was used in this design example, as that has been the prototype bridge considered in this thesis.

Given:

D_c = 6.00' column diameter,
f'_c = 4.00 ksi specified concrete strength of deck concrete, Class 4000D,
d_b = 0.6" nominal strand diameter, area of strand, $A_p = 0.217\ in^2$,
f_{pu} = 270 ksi specified tensile strength of prestressing strands,
f_{py} = 243 ksi for low relaxation strand,
ϕ = 1.00 resistance factor for extreme event limit state,
GTYP = WF74G; H = 74" girder depth,
A = 11¾", "A" dimension,
t_s = 8" slab thickness,
$Y_{t\ slab}$ = 23.897" c.g. of superstructure to top of slab,
h = 125.103" distance from top of column to c.g. of superstructure,
L_1 = 110' Span length of span 1. Factor = 1.00 (two-span bridge),
L_2 = 160' Span length of span 2. Factor = 1.00,
L_{col} = 25' column clear height used to determine overstrength moments,
M_{po}^{top} = 16854 k-ft plastic overstrength moment at the top of the column,
M_{po}^{Base} = 16963 k-ft plastic overstrength moment at the base of the column,
M_{SIDL} = 520 k-ft moment due to SIDL per girder (based on BDM design example in Appendix 5-B10 (WSDOT, 2015)),
γ_p = 0.9

Design Steps:

1. Determine total seismic moment at the center of gravity of the superstructure

$$M_{po}^{CG} = 16584 + \left(\frac{16584 + 16963}{25}\right)\frac{125.103}{12}$$
$$M_{po}^{CG} = 30956.03k - ft \qquad (6.20)$$

2. Determine the design moment per girder

From Step 1, the maximum torque in the cap beam is equal to half of the total seismic moment, namely, $T_o = 15478.015k - ft$.

Considering the following properties,

E_g = 5328 ksi,
E_{cb} = 3644 ksi.

Since $\nu = 0.2$ for concrete and $G = \frac{E}{2(1+\nu)}$,

G_{cb} = 1518 ksi,
I_g = 1313000 in^2 for a composite section including a WF74G girder with a 8" deck on top,
L_g = $12 * 2/(1/110' + 1/160') = 1560$",
L_{cb} = 234",
h_{cb} = 149",
b_{cb} = 96",
$J_{cb} = \frac{h_{cb} b_{cb}^3}{3}\left(1 - 0.63\frac{b_{cb}}{h_{cb}}\right) = 26110000\text{in}^4$, and
N_L = 3.

Finally, considering pinned girder ends, $\lambda L_{cb} = \sqrt{\left(\frac{3EI}{L}\right)_g \frac{2N_L}{(GJ/L)_{cb}}}$.

The ratio λL_{cb} was determined as 0.69 for the reference structure used here (ignoring the lower crossbeam taper, and considering the cap beam section directly above the column, which has the full height of 6' for the cross-beam and 6'-5" for the diaphragm).

Using Table 6.1, the corresponding girder moment ratios, $\frac{M_{g,i}}{T_o}$ are as follows.

Table 6.2: Girder Moment Ratios

Girder No, i	1	2	3
$\frac{M_{g,i}}{T_o}$	0.181	0.164	0.156

The corresponding seismic moment per girder is

Table 6.3: Girder Moments

Girder No, i	1	2	3
$M_{g,i}$ $(k-ft)$	2797	2535	2407

The span moment distribution factors K_1 and K_2 are

$K_1 = \frac{L_2}{L_1 + L_2} = \frac{160}{110 + 160} = 0.593$ and

$K_2 = \frac{L_1}{L_1 + L_2} = \frac{110}{110 + 160} = 0.407$. Equation 6.19 and Table 6.1 are based on the assumption that the two girders in each line each resist 50% of the girder line moment. If the two girder spans differ, the moments should be modified in accordance with the span lengths, using the factors K_1 and K_2 in place of 0.50. The final girder moment demands can be determined as

$M_{g,L_1} = \frac{K_1}{0.5} M_{g,i} - 0.9 M_{SIDL}$ for girders with span length L_1 and

$M_{g,L_2} = \frac{K_2}{0.5} M_{g,i} - 0.9 M_{SIDL}$ for girders with span length L_2

Thus, the design moment for each girder can be determined as given in Table 6.4.

Table 6.4: Design Girder Moments

Girder	1	2	3
M_{g,L_1} (k-ft)	2847	2536	2385
M_{g,L_2} (k-ft)	1811	1597	1493

3. Determine the number of extended strands for each girder

   3.1. Excluding the contribution of extended girder web and bottom flange reinforcing bars into the diaphragm

   The center of gravity of extended strands to the bottom of the girder was taken as 3", so the lever arm, d, is 82.25".

Using $f_{py} = 243$ ksi, the number of extended strands can be determined according to Equation 6.21 as specified in the WSDOT BDM Page 5-B10-2 (WSDOT, 2015).

$$N_{ps} = \frac{M_{g,L}}{0.9\phi A_{ps} f_{py} d}$$
$$N_{ps} = \frac{M_{g,L}}{(0.9)(1.0)(0.217)(243)(82.25)} \quad 6.21$$

The required number of extended strands for each girder are given in Table 6.5.

Table 6.5: Number of Extended Strands Excluding Contribution of Extended Rebars

Girder	1	2	3	Total
N_{ps,L_1}	$8.75 \approx 10$	$7.80 \approx 8$	$7.33 \approx 8$	23.88 (26)
N_{ps,L_2}	$5.57 \approx 6$	$4.91 \approx 6$	$4.59 \approx 4$	15.07 (16)

These strands are sufficient to resist the predicted moment demands in the absence of projecting rebar. The joint shear behavior will be better if the strut-and-tie mechanism within it has the more rational geometry made possible by using only strands that are anchored at the far face of the diaphragm.

3.2. Including the contribution of extended girder web and bottom flange reinforcing bars into the diaphragm

If the web and flange bars are to be extended into the diaphragm, their contributions should be included in the flexural strength of the connection. (7 No. 7 from the girder web extending 22" into the diaphragm, and 4 No. 6 from the bottom girder flange extending 18" into the diaphragm for WF74G girders. The bar stress should be taken as $f_y(l/l_d)$.)

The extended bars provide a moment capacity of 1130 k-ft. As a result, the number of extended strands for each girder is given in Table 6.6.

Table 6.6: Number of Extended Strands Including Contribution of Extended Rebars

Girder	1	2	3	Total
N_{ps,L_1}	$5.28 \approx 6$	$4.32 \approx 4$	$3.86 \approx 4$	$13.46 \approx 14$
N_{ps,L_2}	$2.10 \approx 2$	$1.44 \approx 2$	$1.12 \approx 2$	$4.66 \approx 6$

As can be seen, the number of extended strands can be reduced significantly, but at the cost of adding mild reinforcement. Furthermore, the flow of stresses in the joint would be less advantageous if the bars are used.

Chapter 7

CONCLUSIONS AND FUTURE WORK

7.1 Summary

Precast prestressed bridges in Washington State are designed to resist longitudinal seismic forces by frame action. Moments must therefore be transferred from the ends of the girders, where they are manifested as bending, into the cap beam, where they are manifested as torsion. Consequently, positive moment connections are needed at the girder ends, and they are presently achieved by extending some of the strands located in the bottom flange of the girder into the cast-in-place diaphragm, where they are anchored with strand vices and bearing plates. That hardware configuration can cause conflicts and difficulties during construction. The objectives of this research were to investigate the existing method of making the positive moment connection and, if possible, to develop a new one that would be easier to construct. These goals were addressed using a combination of laboratory testing and structural analysis. The first two tasks, associated with the anchorage capacity of strands equipped with barrel anchors, were completed using laboratory tests. The last task, in which the moment demand at each girder end was evaluated, was conducted using structural analysis.

The performance of a single anchorage device, and in particular the possibility of local concrete crushing behind the strand anchor, was first investigated by physical testing. It was found that a barrel anchor, with no backing plate, was easily sufficient to resist the force imposed by a strand at incipient fracture.

Second, the possibility of a group of strands breaking out from the diaphragm was evaluated. Tests were carried out on strands, anchored by strand vices, grouped in various patterns and embedded to various depths in concrete blocks representing a diaphragm. It

was found that the results were closely predicted by the Concrete Capacity Design method, which can therefore be used to predict the minimum embedment length required to ensure that strand fracture takes place prior to a group breakout failure mode.

Third, the distribution of girder end moments across the bridge was evaluated using Finite Element Analysis. The important parameters were the flexural properties of the girders and the torsional properties of the cap beam. The outcome focused on the girder end moments when the column reached its full flexural capacity.

7.2 Conclusions

- **Resistance of a single anchor**. A barrel anchor, with no backing plate, is easily sufficient to resist, without damage to the anchor or bearing failure of the concrete, the force exerted by a strand at incipient fracture. The high resistance to bearing stresses (measured at approximately 100 ksi on concrete with $f'_c \approx 4$ ksi) is attributed to very efficient confinement behind the anchor.

- **Resistance of a group of strands to failure by breakout**. The Concrete Capacity Design method predicted very accurately the failure loads measured in the tests conducted for this project. Those tests, along with the tests originally used to develop the method, provide verification of the method, which can therefore be used to evaluate the minimum embedment length needed to ensure that ductile strand yield and fracture precede brittle group breakout failure.

- **Distribution of girder moment demand across the bridge**. For bridges constructed with a two-stage cap-beam, used extensively in Washington State, the cap beam system is sufficiently stiff in torsion compared to the flexural stiffness of the girders, such that the moment demand in the end of each girder is almost uniform across the width of the bridge. The end moment used for design, and consequently the number of strands that need to be extended from each girder, may thus be reduced below the values required by the existing design method. That method was developed

from tests conducted on a system in which the ratio of cap beam torsional stiffness to girder bending stiffness was much lower than that typical of Washington State bridges.

7.3 Recommendations

7.3.1 Recommendations for Implementation

- Extended strands, up to and including 0.6" diameter, should be equipped with a barrel anchor alone. No backing plate is necessary.

- Strands should be extended as far as possible across the cap beam to achieve the best transfer of moment into the cap beam. Terminating the strand just inside the vertical reinforcement at the far side of the cap beam maximizes the structural benefits and minimizes the construction difficulties.

- Girder end moments may be determined using the approach outlined in Section 6.6 of this thesis. In most cases, that will lead to equal moments in each girder and the smallest possible number of strands extending from each girder.

- Consideration should be given to eliminating the non-prestressed bar reinforcement in the girder ends, and generating the force required for vertical shear friction in the web from the extended strands alone. This would simplify fabrication of the girders and reduce the possibility of bar conflicts on site.

7.3.2 Recommendations for Further Research

- The research conducted here addressed only right bridges. The anchorage capacities are expected to remain unchanged in skew bridges, so the primary need is to determine the moment demands in skew bridges. Preliminary hand calculations suggest that, in a skew bridge, the cap beam behaves as if it were stiffer than in a comparable right bridge, in which case the girder end moments would be distributed even more uniformly than

was found here. However, that tentative funding should be investigated using Finite Element Analysis.

REFERENCES

AASHTO (2009). *AASHTO Guide Specifications for LRFD Seismic Bridge Design*. American Association of State Highway and Transportation Officials, American Association of State Highway and Transportation Officials, 444 North Capitol Street, NW Suite 249, Washington, DC 20001, United States, 1^{st} Edition.

AASHTO (2012). *AASHTO LRFD Bridge Design Specifications*. American Association of State Highway and Transportation Officials, American Association of State Highway and Transportation Officials, 444 North Capitol Street, NW Suite 249, Washington, DC 20001, United States, 6^{th} Edition.

ACI318 (2011). *Building Code Requirements for Structural Concrete(ACI 318-11) and Commentary*. American Concrete Institute, American Concrete Institute, 38800 Country Club Drive, Farmington Hills, MI 48331, United States.

ASTM (2016). *ASTM A706/A706M Standard Specification for Deformed and Plain Low-Alloy Steel Bars for Concrete Reinforcement*, 16 Edition (March).

Balmer, G. G. (1949). "Shearing Strength of Concrete Under High Triaxial Stress - Computation of Mohr's Envelope as a Curve." *Structural Research Laboratory Report No. SP-23*, U.S. Dept. of the Interior, Bureau of Reclamation, Denver, Colorado, 1–26.

Chuan-Zhi, W., Zhen-Hai, G., Zhen-Hai, G., and Xiu-Qin, Z. (1987). "Experimental Investigation of Biaxial and Triaxial Compressive Concrete Strength." *ACI Material Journal*, 84(2), 92–100.

Fuchs, W., Eligehausen, R., and Breen, J. E. (1995). "Concrete Capacity Design (CCD) Approach for Fastening to Concrete." *ACI Strucutral Journal*, 92(1), 73–94.

Hawkins, N. M. (1968). "The Bearing Strength of Concrete Loaded Through Rigid Plates." *Magazine of Concrete Research*, 20(62), 31–40.

Hibbeler, R. C. (2011). *Mechanics of Materials,* Custom Edition for the Univeristy of Washington. Pearson Prentice Hall.

Holombo, G. J. (1999). "Seismic Design of Precast Girder Bridges." PhD Dissertation, University Of California, San Diego, San Diego, California, United States.

Holombo, J., Priestley, M. J. N., and Seible, F. (2000). "Continuity of Precast Prestressed Spliced-Girder Bridges Under Seismic Loads." *PCI Journal*, 45(2), 40–63.

Ma, J. (2008). "Caltrans Bridge Design Overview." 15^{th} Annual CALTRANS/PCMAC Bridge Seminar. Available at https://www.yumpu.com/en/document/view/12065309/california-precast-bridge-design-in-the-past-precast-prestressed-. Accessed on: 3/1/2017.

Marsh, M. L., Stringer, S. J., Stanton, J. F., Eberhard, M. O., Haraldsson, O. S., Tran, H. V., Khaleghi, B., Schultz, E., and Seigurant, S. (2013). "Precast Bent System for High Seismic Regions." *Report No. FHWA-HIF-13-037*, Federal Highway Administration, United States.

Miller, R. A., Castarodale, R., Mirmiran, A., and Hastak, M. (2004). "Connection of Simple-Span Precast Concrete Girders for Continuity." *Report No. 519*, National Cooperative Highway Research Program, Transportation Research Board, Business Office 500 Fifth Street, NW Washington DC 20001, United States.

Newhouse, C. D., Roberts-Wollmann, C. L., Cousins, T. E., and Davis, R. T. (2007). "Comparison of Strands and Bars for Positive Moment Connection of Continuous Precast Concrete Bulb-Tee Girders." *PCI Journal*, 52(3), 18–28.

Newman, K. and Newman, J. (1971). "Failure Theories and Design Criteria for Plain Concrete." *Proceedings for International Civil Engineering Material Conference on Structural,*

Solid Mechanics and Engineering Design, London, Wiley-Interscience, New York, NY, 963–995.

Noppakunwijai, P., Jongpitakseel, N., Ma, Z. J., Yehi, S. A., and Tadros, M. K. (2002). "Pullout Capacity of Non-Prestressed Bent Strands for Prestressed Concrete Girders." *PCI Journal*, 47(4), 90–103.

Owen, L. M. (1998). "Stress-Strain Behaviour of Concrete Confined by Carbon Fiber Jacketing." M.S. thesis, University of Washington, United States.

PCI (2004). *PCI Design Handbook Precast and Prestressed Concrete*. Precast/Prestressed Concrete Institute, Precast/Prestressed Concrete Institute, 209 W Jackson Blvd, Suite 500, Chicago, Illinois 60606, United States, 6^{th} Edition.

Pilkey, W. D. (2005). *Formulas for Stress, Strain, and Structural Matrices,* Second Edition. John Wiley & Sons, Inc.

Priestley, M. J. N., Seible, F., and Calvi, G. M. (1996). *Seismic Design and Retrofit of Bridges*. John Wiley & Sons, Inc. p. 200.

Richart, F. E., Brandtzaeg, A., and Brown, R. L. (1929). "The Failure of Plain and Spirally Reinforced Concrete in Compression." *University of Illionois Bulletin*, Vol. 26, Engineering Experiment Station, University of Illionois at Urbana-Champaign, 1–74.

Stanton, J. F. (2002). "Torsion. CEE 220 Introduction to Mechanics of Materials. University of Washington.

Wight, J. K. and MacGregor, J. G. (2012). *Reinforced Concrete: Mechanics and Design*. Pearson Education Inc.

WSDOT (2015). *WSDOT Bridge Design Manual (LRFD)*. Washington State Department of Transportation, Washington State Department of Transportation, Bridge and Structures Office, PO Box 47340, Olympia, WA 98504, United States, M 23-50.14 Edition.